THE INFLUENCE OF PARTICLE SIZE, MICROFRACTURES, AND MOISTURE CONTENT ON THE PERMEABILITY OF CRUSHED SHALE SAMPLES

By

MERCY ACHANG
Bachelor of Science in Physics
The University of Dschang
Dschang - Cameroon
2002

Master of Science in Geophysics
The University of Yaoundé I
Yaoundé - Cameroon
2008

Submitted to the Faculty of the
Graduate College of the Arts and Science
Oklahoma State University
in partial fulfillment of
the requirements for
the Degree of
DOCTOR OF PHILOSOPHY
July 2018

THE INFLUENCE OF PARTICLE SIZE, MICROFRACTURES, MOISTURE CONTENT ON THE PERMEABILITY OF CRUSHED SHALE SAMPLES

Dissertation Approved:

Jack C. Pashin. Ph.D., Chair

Dissertation Adviser

Michael G. Grammer, Ph.D.

James O. Puckette, Ph.D.

Peter Clark, Ph.D.

ACKNOWLEDGEMENTS

This dissertation has been completed thanks to God Almighty for giving me strength and wisdom every step of the way; unless the Lord builds a house, the laborer labors in vain. God positioned great mentors and facilitators of destiny on my path to refine me into a desirable and useable end product.

I would like to express my profound gratitude to my Committee Chair and Advisor Dr. Pashin for his enthusiastic encouragement and useful critiques of this research. When I felt my research world was crumbling, Dr. Pashin, you believed in me and never gave up. I learned a lot from your experience as a geologist wearing multiple hats and will always look back with a smile. My deepest thanks also goes to my committee members, Dr. James Puckette for his open door policy to students and having to answer my questions all the time, Dr. Michael Grammer, for giving me an understanding of carbonates and advanced observational skills and my external committee member Dr. Peter Clark for suggestions about my experimental design. Thanks for being supportive and motivating.

I am thankful to Dr. Eliot Atekwana for sharpening my critical thinking and research writing skills and constant review of my manuscripts. Thank You, Dr. Estella, for being a mentor, mother, and pacesetter in my life. My gratitude to Dr. Mary Hileman for your motivation and kind words in the moment of need. Sincere thanks to Dr. Mohamed Abdelsalam, for being an outstanding graduate coordinator. I also thank Dr. Albert Cui for his intellectual contributions and Trican Geological Solutions for running some of my crushed shale samples free of charge. Sincere thanks to all the professors at the Boone

Pickens School of Geology for teaching and helping me hone my skills and abilities in geology.

My gratitude to Dr. Hari Parameswar for his intellectual contributions and permission to collect Nuclear Magnetic Resonance (NMR) data in his laboratory at the Department of Physics and Engineering Physics at the University of Tulsa. Thank you, Dr. Frank Blum, for permitting us to run nitrogen sorption measurements in your Laboratory at Oklahoma State University. And thanks to Ugo Arua for running the sorption experiments.

This research was supported by the Oklahoma State University, Boone Pickens School of Geology, American Association of Petroleum Geology, Geological Foundation of Oklahoma, Society of Petrophysicist and Well Log Analyst, National Association of Black Geoscientist and the Department of Energy United States' Carbon Safe project. Thank you.

My family was very supportive, and I would like to thank my parents, and especially my mother, Manyi Rose Afor, whose strength has motivated me twenty-six years after my father's passing. I would also like to thank my siblings, Lawson, Precilia, Dinah, Thomas, Felicia, Ruth, Dorothy, Lilian and their families for their constant love and support. Most importantly, I would like to thank my loving husband for his support and care as well as allowing me to keep late hours in the laboratory.

Thank you Solid Rock Church and most especially pastors John and Daniel for hosting and blessing my wedding as well as preaching and teaching the uncompromised word of God.

I am also deeply grateful to my friends and colleagues, in particular Andrew Katumwehe, Sahar Mohammadi, Khumo Lesaene, Gamal Zidan, Jingyao Meng, Ibukun Bode, Liang

Xue, Avinash Chandra, Stone Urban, Conn Wethington, Gerret Powel, Pouyan Ebrahimi, Babak Shabani, Micah Mayle, Victor Nyalugwe Charles Missi, Njinju Emmanuel, Laurie Whitesell, Georgina Lukoczki, Tadesse Alemu, Afshin Aghayan, Fidelis Atuo, Jun Fu, Yolande Mbah Mbole and other graduate students for standing by me throughout my doctorate program and for being a motivation and support system. You made my time here at Oklahoma State University memorable and I am thankful.

Thank you, Sandy Earls, Tabitha Schneider and Heather Diane Lindsey for making sure all my paperwork was in good condition.

Name: MERCY ACHANG

Date of Degree: July, 2018

Title of Study: THE INFLUENCE OF PARTICLE SIZE, MICROFRACTURES, MOISTURE CONTENT ON THE PERMEABILITY OF CRUSHED SHALE SAMPLES

Major Field: GEOLOGY

ABSTRACT

Permeability, porosity and pore size distribution in shale are essential for the evaluation and optimization of hydrocarbon recovery. The absence of standardized procedures for measuring permeability is thought to result in the lack of repeatable and accurate permeability estimates for crushed shale since the permeability of the same sample measured by different laboratories can vary by orders of magnitude. Also, changes in stress, moisture content, microfractures whether natural or induced by crushing, and hydrocarbon content during retrieval of samples from the subsurface to the laboratory influence permeability as well. Moisture loss results from transportation storage of samples for hours to decades before permeability analysis. This is a fundamental preservation problem which can be solved by normalizing or restoring moisture. This research investigates (1) the relationship between crushed particle size and crushed-rock pressure-decay permeability, (2) microfractures in particles of different sizes, (3) the mass of sample required for accurate permeability measurements with a shale matrix permeameter (4) permeability in as-received and moisture equilibrated crushed shale samples and (5) pore size distribution in crushed and whole-rock shale samples. The methods used are; core description scanning electron microscopy, helium porosimetry, and crushed-rock permeability. Results suggest that matrix permeability increases with particle size, particles of all sizes in the Woodford Shale core studied contain microfractures. Permeability values are dependent on the technique used for permeability analysis, and pressure decay curves have three distinct segments: hyperbolic, exponential and pseudo-steady state. Replicate sample runs indicate that permeability measurements are more repeatable for moisture equilibrated samples than as-received samples across a range of particle sizes.

According to pore size distributions determined by nuclear magnetic resonance (NMR), an increase in the area under the T_2 distributions is suggested to be related to artificial pore space created by crushing the shale. Both whole rock samples and crushed shale have unimodal and bimodal T_2 distributions. Pore size distributions determined from low pressure and temperature nitrogen sorption are dominated by mesopores where a large quantity of gas is sorbed. Pore shapes are slitlike based on NMR and SEM analysis.

PUBLICATION DISSERTATION OPTION

This dissertation has been structured into two sections: The first section is a brief overview of the dissertation and an introduction of the scientific questions that were investigated. Also included in this section are one published article and two manuscripts in review for publication.

Paper 1: The influence of particle size, microfractures, and pressure decay on measuring the permeability of crushed shale samples. International Journal of Coal Geology, Volume 183, 1 October 2017, Pages 174-187: https://doi.org/10.1016/j.coal.2017.09.012

Paper 2: The Influence of Moisture on the Permeability of Crushed Shale Samples. This work has been Accepted with revisions for publication: Petroleum Science by Springer: ID PETROSCI-2018-0040

Paper 3: Comparison of Pore Size Distribution on Crushed and Core Plug Shale Samples Using Nuclear Magnetic Resonance (NMR)**.** This work has been submitted to the Elsevier Journal, Fuel.

TABLE OF CONTENTS

LIST OF FIGURES

CHAPTER II. THE INFLUENCE OF PARTICLE SIZE, MICROFRACTURES, AND PRESSURE DECAY ON MEASURING THE PERMEABILITY OF CRUSHED SHALE SAMPLES

APPENDICES

CHAPTER III. THE INFLUENCE OF MOISTURE ON THE PERMEABILITY OF CRUSHED SHALE SAMPLES

CHAPTER IV. COMPARISON OF PORE SIZE DISTRIBUTION ON CRUSHED AND WHOLE-ROCK SHALE SAMPLES USING NUCLEAR MAGNETIC RESONANCE.

CHAPTER I

INTRODUCTION AND GENERAL OVERVIEW

1.0 Motivation and problem

Shale is a fissile, fine-grained sedimentary mudrock consisting mainly of clay minerals, carbonate, silica and organic matter (Loucks and Ruppel, 2007). Shale that is rich in organic matter forms extensive, continuous-type petroleum accumulations (Schmoker and Oscarson, 1995). Organic-rich shale formations act as self-contained petroleum systems comprising the source rock, migration conduit, and reservoir rock for natural gas, natural gas liquids, and oil.

Precision directional drilling and multi-stage hydraulic fracturing have transformed tight rocks, including shale, into commercially viable, world-class petroleum reservoirs. This has stirred interest in petrophysical characterization of porosity, permeability, and fluid saturation in shale. Knowledge of porosity and permeability is essential for reservoir characterization, resource and reserve estimation, identification of bypassed pay, analyzing reservoir seals, and optimization of production. Quantification of pore size distribution is required for fluid flow modeling and the delineation of flow units in the reservoir (Yasin et al., 2017). When shale cores or cuttings are recovered from the subsurface and taken to the laboratory for permeability measurement, these samples do not retain their native subsurface properties. Changes in stress, fluid saturation, microfractures, moisture and hydrocarbon content influence matrix permeability values measured in the laboratory (Bustin et al., 2008; Chalmers and Bustin, 2010).

Acquiring accurate and repeatable permeability measurements in the laboratory is a concern since there are no standard procedures for measurement (Cui et al., 2009; Sondergeld et al., 2010a; Suarez-Rivera et al., 2012; Tinni et al., 2012). The same samples sent to different laboratories for permeability measurements yield results that can differ by orders of magnitude. In an attempt to minimize microfractures and reduce stress-release artifacts, Luffel et al. (1993) suggested crushing the rock to a particle size of 0.7 mm. However, micro-CT scans by Tinni et al. (2012) show that samples crushed to 0.7 mm still have microfractures. The aim of this project is to analyze how variables such as moisture content, crushed rock particle size, microfracturing and curve fitting techniques influence the determination of crushed rock permeability. This was accomplished by using the pressure-decay method and to identify how these variables impact repeatability of results and relate to the native reservoir. This research program also included a comparison of pore size distribution between whole-rocks and crushed shale samples using nuclear magnetic resonance (NMR) techniques and scanning electron microscopy (SEM).

Moisture loss is a fundamental preservation problem associated with transportation and storage of samples prior to permeability analyses being performed in the laboratory. Some samples are stored for hours to decades before they are analyzed (RP40, 1998). Chenevert and Amanullah (1997) have suggested shale should be preserved with its native moisture for accurate measurement of physical properties such as saturation, porosity, permeability, and bulk volume. Clarkson et al. (2011) have shown that water saturation in crushed samples can change from 40% to 2% at 20°C within 12 hours. To help retain moisture, most laboratories store cores in polythene bags to minimize dehydration. However, the cores still dehydrate over time (Chenevert and Amanullah., 1997) since laboratory conditions are different from subsurface temperature and pressure. Also, the physical presence of salt on the Danker#1-28 sample was an indication of moisture loss over time. Moisture equilibration is a procedure that is commonly used for the proximate analysis of coal (Standards and International, 2007). Coal is a sedimentary rock that is susceptible to moisture loss following sampling, and this is especially true of coal at low thermal maturity (e.g., lignite, subbituminous, and high volatile C bituminous coal). Moisture equilibration or conditioning is the process by which hygroscopic materials reach equilibrium with the ambient relative humidity of the air by adsorbing or desorbing moisture until the material neither loses nor gains moisture from the environment. Moisture equilibration can be performed rapidly on crushed rock samples but is challenging if not impossible to apply to core plugs where equilibration times may be on the order of months or years. Chenevert and Amanullah (1997a, b) have shown how loss of moisture in preserved shale samples leads to inaccurate estimation of physical properties and the development of capillary artifacts but no investigations have been performed specifically to determine how moisture content affects matrix permeability.

Nuclear magnetic resonance (NMR) is a robust method for characterizing porosity, permeability, pore size distribution, fluid saturation, and fluid type in shale (Coates et al., 1999). NMR is a technique based on the response of an atomic nucleus (e.g., hydrogen) to an external magnetic field (Coates et al., 1999; Kenyon, 1997). When Carr-Purcell-Meiboom-Gill (CPMG) pulse sequences are applied during an NMR experiment, the transverse and longitudinal relaxation that results is used to infer porosity, pore size distribution, fluid type, and fluid mobility. Crushed and whole-rock pore size distribution (PSD) and porosity from NMR has been analyzed to detect differences in porosity and pore size distribution to assess reservoir properties and to characterize damage to rock particles induced by crushing.

Gas transport in shale is a combination of diffusion in nanopores and Darcy flow in larger pores and fractures (Gensterblum et al., 2015; Javadpour, 2009; Javadpour et al., 2007; Sondergeld et al., 2010b). Gas in shale is stored in the open pore space as free gas and sorbed to pore surfaces as adsorbed gas. Thus, determining the quantity of sorbed gas in shale reservoirs is required for proper characterization of fluid transport. Low-pressure nitrogen sorption measurements can be used to characterize pore size distribution, pore volume, and other parameters such as surface area, microporosity, and pore shape; all factors which control the sorption capacity and reservoir quality of shale (Rouquerol et al., 1994; Thommes et al., 2015). For example, pore shape influences pore volume, connectivity, and rock strength (Labani et al., 2013; Zhang et al., 2016)..

Clarkson (2013), Heller and Zoback (2014), and Sondergeld et al. (2010) have identified three major problems with measuring shale matrix permeability: (1) the suggested 0.7 mm particle size contains microfractures, and so pressure decay measurements may not be representative of matrix permeability, (2) there is no standard moisture restoration procedure to compensate for loss of inherent moisture in samples that have been stored for extended periods and (3) no experimental data are available that demonstrate the influence of moisture content on the permeability of shale. Also, there is no comparative study that has been done using NMR to compare pore size distribution in crushed and whole-rock shale samples, thereby determining the effects of crushing shale on porosity over a range of crushed rock particle sizes.

2.0 Research Question and Objectives

The research questions are:

a. What is the relationship between particle size and crushed rock pressure-decay permeability? Do all particle sizes contain microfractures, and how does permeability determined from crushed rock pressure-decay curves compare with permeability determined using different techniques?
b. How does moisture equilibration influence the permeability of crushed shale samples?
c. How do pore size distributions in crushed rocks compare to those in whole-rock samples?

The objectives of this research are to:

a. Determine the relationship between crushed shale particle size and matrix permeability by analyzing pressure-decay curves using late time analysis (Cui et al., 2009).

b. Perform controlled experiments to evaluate the relationship between moisture content and permeability.

c. Compare pore size distributions of whole-rock and crushed samples using NMR and gas porosimetry.

To answer the above research questions, shale was crushed to different particle sizes, and permeability experiments were conducted. Samples were moisture equilibrated using the American Society for Material and Testing (ASTM) standard for coal moisturization (Standards International, 2007), and permeability was compared in as-received and moisture-equilibrated samples. Microfractures and shale fabrics were analyzed via scanning electron microscopy (SEM), and routine petrographic analysis and core analysis (porosity, fluid saturation) was used to characterize samples.

3.0 Significance of Study

The results of this dissertation research have provided new information that is relevant for determining an effective and optimal particle size for shale matrix permeability measurements. We have shown that it is useful to report permeability from the hyperbolic and exponential component of time vs. LnFr plot (Cui et al. 2009). In addition, we have established that the permeability of moisture-equilibrated shale samples is more repeatable and is less than permeability measured on an as-received basis in shale samples.

Finally, this research has provided a robust method for measuring matrix permeability by redefining particle size parameters, sample run time, and pressure-decay curve analysis. The relationship between shale moisture content and shale matrix permeability has also been demonstrated for the first time.

References Cited

Bustin, R.M., Bustin, A.M., Cui, A., Ross, D., Pathi, V.M., 2008. Impact of shale properties on pore structure and storage characteristics, SPE shale gas production conference. Society of Petroleum Engineers.

Chalmers, G.R., Bustin, M.R., 2010. PS The Effects and Distribution of Moisture in Gas Shale Reservoir Systems.

Chenevert, M., Amanullah, M., 1997. Shale preservation and testing techniques for borehole-stability studies. SPE Drilling & Completion 16, 146-149.

Clarkson, C.R., Jensen, J.L., Blasingame, T., 2011. Reservoir engineering for unconventional reservoirs: what do we have to consider? SPE 145080., North American Unconventional Gas Conference and Exhibition. Society of Petroleum Engineers.

Coates, G.R., Xiao, L., Prammer, M.G., 1999. NMR logging: principles and applications. Haliburton Energy Services Houston.

Cui, X., Bustin, A., Bustin, R.M., 2009. Measurements of gas permeability and diffusivity of tight reservoir rocks: different approaches and their applications. Geofluids 9, 208-223.

Gensterblum, Y., Ghanizadeh, A., Cuss, R.J., Amann-Hildenbrand, A., Krooss, B.M., Clarkson, C.R., Harrington, J.F., Zoback, M.D., 2015. Gas transport and storage capacity in shale gas reservoirs–A review. Part A: Transport processes. Journal of Unconventional Oil and Gas Resources 12, 87-122.

Javadpour, F., 2009. Nanopores and apparent permeability of gas flow in mudrocks (shales and siltstone). Journal of Canadian Petroleum Technology 48, 16-21.

Javadpour, F., Fisher, D., Unsworth, M., 2007. Nanoscale gas flow in shale gas sediments. Journal of Canadian Petroleum Technology 46.

Kenyon, W., 1997. Petrophysical principles of applications of NMR logging. The Log Analyst 38.

Labani, M.M., Rezaee, R., Saeedi, A., Al Hinai, A., 2013. Evaluation of pore size spectrum of gas shale reservoirs using low pressure nitrogen adsorption, gas expansion and mercury porosimetry: A case study from the Perth and Canning Basins, Western Australia. Journal of Petroleum Science and Engineering 112, 7-16.

Loucks, R.G., Ruppel, S.C., 2007. Mississippian Barnett Shale: Lithofacies and depositional setting of a deep-water shale-gas succession in the Fort Worth Basin, Texas. AAPG bulletin 91, 579-601.

Luffel, D., Hopkins, C., Schettler Jr, P., 1993. Matrix permeability measurement of gas productive shales, SPE Annual Technical Conference and Exhibition. Society of Petroleum Engineers.

RP40, A., 1998. Recommended practices for core analysis. Feb.

Rouquerol, J., Avnir, D., Fairbridge, C., Everett, D., Haynes, J., Pernicone, N., Ramsay, J., Sing, K., Unger, K., 1994. Recommendations for the characterization of porous solids (Technical Report). Pure and Applied Chemistry 66, 1739-1758.

Schmoker, J., Oscarson, S.A., 1995. Descriptions of continuous-type (unconventional) plays of the US Geological Survey 1995 National assessment of United States oil and gas resources. US Geological Survey.

Sondergeld, C., Newsham, K., Comisky, J., Rice, M., Rai, C., 2010a. Petrophysical Considerations in Evaluating and Producing Shale Gas Resources. Paper SPE 131768 presented at the SPE Unconventional Gas Conference, Pittsburgh, Pennsylvania, USA, 23–25 February.

Standards, A.I., International, A., 2007. Standard test method for equilibrium moisture of Coal at 96 and 97 percent relative humidity and 30 degress celcius, D1412 − 07.

Suarez-Rivera, R., Chertov, M., Willberg, D.M., Green, S.J., Keller, J., 2012. Understanding permeability measurements in tight shales promotes enhanced determination of reservoir quality, SPE Canadian Unconventional Resources Conference. Society of Petroleum Engineers.

Thommes, M., Kaneko, K., Neimark, A.V., Olivier, J.P., Rodriguez-Reinoso, F., Rouquerol, J., Sing, K.S., 2015. Physisorption of gases, with special reference to the evaluation of surface area and pore size distribution (IUPAC Technical Report). Pure and Applied Chemistry 87, 1051-1069.

Tinni, A., Fathi, E., Agarwal, R., Sondergeld, C.H., Akkutlu, I.Y., Rai, C.S., 2012. Shale permeability measurements on plugs and crushed samples, SPE Canadian Unconventional Resources Conference. Society of Petroleum Engineers.

Yasin, Q., Du, Q., Yuan, G., Ismail, A., 2017. Application of hydraulic flow unit in pore size classification, 2017 SEG International Exposition and Annual Meeting. Society of Exploration Geophysicists

Zhang, Q., Liu, R., Pang, Z., Lin, W., Bai, W., Wang, H., 2016. Characterization of microscopic pore structures in Lower Silurian black shale (S 1 l), southeastern Chongqing, China. Marine and Petroleum Geology 71, 250-259.

CHAPTER II

THE INFLUENCE OF PARTICLE SIZE, MICROFRACTURES, AND PRESSURE DECAY ON MEASURING THE PERMEABILITY OF CRUSHED SHALE SAMPLES

Mercy Achang[a], Jack C. Pashin[a], Cui, X[b]

International Journal of Coal Geology (2017), 183:174-187

[a] Boone Pickens School of Geology, Oklahoma State University, Stillwater, OK, 74078, USA

[b]Trican Geological Solutions, T2P 4G8, S.W. Calgary, Alberta, Canada

Abstract

Measurement of matrix permeability is essential for predicting, evaluating, and modeling the performance of shale reservoirs. However, the repeatability and accuracy of these measurements can be questioned because procedures have not been standardized. As a result, permeability measurements from the same sample by different laboratories can vary by orders of magnitude. Microfracturing related to changes in stress during core retrieval and crushing during sample preparation is thought to be a significant source of error. Different interpretations of pressure decay curves could also account for inconsistent permeability values. The goals of this research were to analyze relationships among crushed particle size, microfractures, and matrix permeability, as well as to evaluate the ways in which pressure decay curves are interpreted and to determine the sample mass best suited for analysis. Crushed rock pressure-decay measurements of particles of different sizes were obtained using a shale matrix permeameter, and permeability was estimated by curve fitting using Core Laboratories software and by other methods that assess the geometry and evolution of pressure decay curves. Results indicate that the relationships between permeability and particle size vary considerably when determined by different methods. Analysis of pressure decay curves reveals three distinct segments. The early segment is characterized by hyperbolic decay, whereas the late segment is characterized by exponential decay. A third segment records a pseudo-steady state where pressure has declined to the extent that decay can no longer be characterized. Decay was measured for about 2000 s; most decay curves stabilize within 500 s, and data collected beyond 500 s are dominated by noise associated with the pseudo-steady state and are beyond the resolution of the apparatus used.

Analysis of early hyperbolic curves yields permeability values one to two orders of magnitude greater than whole curve analysis. The hyperbolic pressure decay segment appears to be influenced by microfractures and other large pores near the surface of samples, whereas the late time segment and whole curve correlate more strongly with the microporous to nanoporous rock matrix. Also, permeability values derived from whole curve analysis are sensitive to measurement duration, and different values are obtained when permeability is determined from different time windows. SEM images of all particle sizes analyzed reveal microfractures with diameters ranging from 60 to 1,020 nm, but no correlation was found between microfracture aperture and particle size. The optimal sample mass used in our shale permeameter is 50-100 g, which facilitates resolution of the major elements of the decay curve. Optimal particle sizes are between 1.0 and 1.4 mm.

Keywords: Matrix permeability; Crushed shale; Microfractures; Hyperbolic and Exponential segments.

1. Introduction

Accurate measurement of matrix permeability is essential for predicting, evaluating, and modeling the performance of shale reservoirs (e.g., Soeder, 1988; Luffel et al., 1993; Cui et al., 2009). However, the repeatability and accuracy of these measurements are limited because procedures have not been standardized. The goal of this paper is to critically assess the crushed rock pressure-decay method of permeability determination in shale and to identify variables, such as rock particle size, microfracturing, and curve fitting techniques that may affect the repeatability and comparison of results. When shale samples are retrieved from the subsurface, they often do not retain their native reservoir properties, and those properties continue to change during storage. Changes in stress, moisture and hydrocarbon content can have a significant effect on the matrix permeability measured in the laboratory (Bustin and Bustin, 2012; Chalmers et al., 2012b) (Fig II - 1). Properties of the core that are effectively stable upon retrieval include lithology, sedimentary structure, bioturbation, organic matter content, and thermal maturity. By contrast, changing pressure and temperature upon retrieval affect moisture content, volatile hydrocarbon content, fracturing, and porosity—and thus matrix permeability (Fig II - 1). Matrix permeability is an essential variable for reservoir characterization, reservoir simulation, well design, stimulation design, and field design. Natural and induced microfractures in core and sample cuttings often lead to overestimation of matrix permeability (Luffel et al., 1993; Guidry et al., 1996). Luffel et al. (1993) suggested that shale samples should be crushed to a size of 0.7 mm to minimize microfractures, increase the surface area accessible by gas, and improve the accuracy of measurements. However, mercury injection capillary pressure (MICP) measurements and CT scans of 0.7 mm shale particles indicate that microfractures are still common (Heller et al., 2014; Javadpour et al., 2007; Sondergeld et al., 2010; Tinni et al., 2012). The high pressures (207-414

MPa) applied during MICP measurements may lead to stress-relaxation fracturing of the samples (Clarkson, 2013).

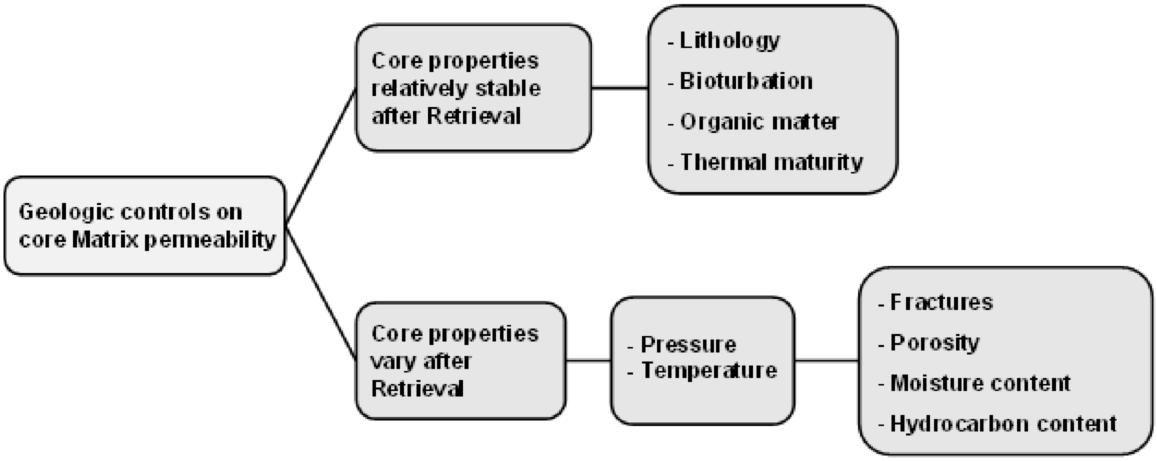

Fig II - 1. Geologic controls on matrix permeability in shale when core is retrieved from the subsurface.

According to Clarkson et al. (2011), Heller et al. (2014), and Sondergeld et al. (2010), a major problem with measuring shale matrix permeability is that the particles contain microfractures, and so the corresponding pressure decay measurements may not be representative of matrix permeability. Hence, it is not clear that the 0.7 mm particle size suggested by Luffel et al. (1993) is optimal for measuring permeability using crushed shale samples. The desire to produce repeatable matrix permeability values has led to the use of diverse permeability measurement methods on shale core plugs and crushed samples (Cui et al., 2009; Luffel et al., 1993; Sondergeld et al., 2010; Tinni et al., 2012). Even so, repeatability of results remains a major issue because different laboratories still report vastly different results from pressure decay analysis of the same shale samples.

Pressure-transient measurement techniques, such as pulse-decay and pressure-decay methods, are commonly used to determine the matrix permeability of shale. Pulse decay and oscillating pressure techniques are used to measure permeability in core plugs (Brace et al., 1968; Dicker and Smits, 1988; Kranz et al., 1990; Jones, 1997; Gensterblum et al., 2015; Hannon, 2016; Sander et al., 2017). Pressure decay (a.k.a. pressure decline) techniques, by contrast, are typically used to measure permeability in crushed shale samples (Cui et al., 2009; Guidry et al., 1996; Rezaee, 2015; Tinni et al., 2012). Also, Profile permeability[1] Pressure-Decay methods exist and are used to identify and quantify thin, highly permeable beds. In the pulse decay and pressure decay methods, pressure is recorded over time, and the shape of the resulting pressure decline curve is used to estimate permeability. Transient methods were devised partly because the traditional steady state approach used to determine permeability in porous tight rocks requires hours to three months to measure permeability (Boulin et al., 2012; Hannon, 2016); moreover, fractures within plugs may lead to overestimation of permeability (Guidry et al., 1996; Luffel et al., 1993). An advantage of pressure decay methods is rapid turnaround, which makes this type of analysis attractive to commercial laboratories. Indeed, individual determinations can be made in 30 min or less (Luffel et al., 1993; Rezaee, 2015; Sander et al., 2017).

Permeability is estimated from crushed-rock pressure-decay curves mainly by history matching (Chavent et al., 1975; Oliver and Chen, 2011) and late time analysis (Cui et al., 2009). Typical crushed rock pressure-decay curves are shown in Appendix A (Fig A - 1). In history matching, permeability is obtained by curve fitting to match the history of pressure decay. Ning et al. (1993) wrote a history matching program that uses a diffusivity algorithm to match pressure decline. Ning

---

[1] Note: Profile permeability Pressure-Decay methods used to identify and quantify thin, highly permeable beds, permeability barriers, and depositional/diagenetic features. The permeability automatically measured in both Y and X-axis. (CoreLab pressure-decay-profile-permeameter-pdpk-400)

et al. (1993) employed an optimization routine to find the combination of porosity and permeability that yields the best match between laboratory data and a diffusivity equation. Luffel et al. (1993) and Core Laboratories (2013) both used pressure decay algorithms to analyze permeability in shale. However, these algorithms have not been made available in literature for evaluation and general use.

The objectives of this research are to (1) determine the relationship between crushed particle size and crushed-rock pressure-decay permeability, to (2) evaluate microfractures in different particle sizes, to (3) evaluate crushed-rock pressure-decay curves and permeability determinations measured by different techniques, and (4) determine the mass of sample required for accurate permeability measurements with the SMP 200.

2. Materials and methods

2.1. Core description

An H-gauge core[2] from the Danker #1-28 well (API number 35081238170000[3]), was recovered from the Woodford Shale (Devonian) in Lincoln County Oklahoma, USA, and was donated to the Boone Pickens School of Geology by Sundown Energy. The slabbed core was photographed, and rock type, color, physical sedimentary structures, biogenic structures, and diagenetic structures were described following standard stratigraphic and sedimentologic procedures (e.g., Lazar et al., 2015a, b). A graphic core log was constructed to reveal the vertical succession of rock types, bedding styles, and sedimentary structures. The core was sampled at various depths for laboratory

---

[2] A drill bit that has an outside diameter of approximately 96 mm and core (inside) diameter of about 63.5 mm.

[3] API number; is a unique, permanent, numeric identifier assigned to each well drilled for oil and gas in the United States by the American Petroleum Institute.

analysis; sample numbers corresponding to the core footages from which the samples were taken was used.

Rock-Eval pyrolysis and LECO TOC analysis were used to evaluate the organic matter content, kerogen type and thermal maturity of the shale samples. The Fluid saturation of each sample was measured by Dean-Stark analysis (Handwerger et al., 2011).

2.2. SEM analysis

The butt slab of the core was sawn into two halves perpendicular to bedding, and one of the halves was crushed using a hammer and metal slab. The particles were sieved using the following US mesh sizes: 10 (2.03 mm), 12 (1.70 mm), 14 (1.40 mm), 16 (1.18 mm), 18 (1.00 mm). 20 (0.85 mm), 25 (0.70 mm) and 30 (0.60 mm). Thirty particles of each size class were selected randomly for SEM analysis (Table 1); they were affixed to a cylindrical stub and coated with a gold-palladium alloy using a Balzers MED 010 sputter coater to minimize imaging artifacts caused by charging of surfaces. The particles were imaged using an FEI Quanta 600 SEM to characterize texture and microfractures.

Table 1: Mesh size and approximate particle population used for crushed particle SEM analysis for microfracture identification.

US. Mesh size	Number of particles	SEM Analysis
10 (2.0 mm)	30	yes
12 (1.7 mm)	30	yes
14 (1.4 mm)	30	yes
16 (1.2 mm)	30	yes
18 (1.0 mm)	30	yes
20 (0.85 mm)	30	yes
25 (0.71 mm)	30	yes
30 (0.60 mm)	30	yes

2.3. Ion milling

Four shale samples were selected at 2 ft intervals from the Danker #1-28 core for SEM analysis (Table 2). The samples were cut to a size of 7 X 10 X 2.5 mm and argon-ion milled with a JEOL IB-19500CP cross section polisher. The milled samples were coated and imaged using the same tools that were used for the crushed shale particles. Images of the samples were then made on the SEM and described to characterize rock composition and rock fabric. An EDS analyzer on the SEM was used to help determine elemental composition.

Table 2: Depths and interval at which samples were chosen for ion milling and SEM analysis for fabric characterization.

Sample ID	Depth (ft)	Depth (m)	Ion milled	SEM
Sample 1	4900 - 4902	1492.13 - 1494.13	1	1
Sample 2	4904 - 4907	1494.74 - 1495.65	1	1
Sample 3	4907 - 4909	1495.65 - 1496.26	1	1
Sample 4	4909 - 4911	1496.26 - 1496.87	1	1

2.4. Bulk density

The bulk volume of selected core samples was determined using the Archimedes fluid (water and mercury) displacement method. Grain volume was measured using a pycnometer following the procedures of Chalmers et al. (2012a) and Rezaee (2015). The mass of samples was determined using a Mettler Toledo mass balance (model MS303S with 1 mg precision). Bulk density was estimated from a plot of the mass and bulk volume. The average bulk density was used to determine porosity.

Samples were selected on the bases of core description, porosity measurement and geophysical log characteristics. Samples 2, 3, 4 were chosen for permeability analysis because they represent typical charcteristics of the Woodford Shale in the Danker core based on the criteria mentioned above. Sample 1 contains abundant pyrite nodules and bands and thus appeared unrepresentative of the overall Woodford Shale interval in the Danker core.

2.4. Experiment

Crushed shale samples were used for permeability estimation with a Core Laboratories SMP 200 shale matrix permameter (Fig II -2). Helium was used as the permeating gas because it is inert and forms an extremely thin Langmuir monolayer of adsorbed gas. The permeameter was powered for 30 min before running samples to allow time for the pressure transducer to stabilize. A pressure decay leak test was run to ensure that the apparatus was tightly sealed so that a leakage rate of < 3.1E-5 psi/s was recorded (Core Laboratories, 2013). Next, 1 mm-diameter glass beads were used as test samples to provide a baseline pressure-decay response for nonporous particles (Fig II -3). The sample holder was then filled with 55-60 g of crushed sample. The filled sample holder was placed on a shaker for 30 s to ensure uniform particle packing and to reduce air-filled space between particles. The temperature was held constant at 24±1˚C by placing the permeameter in a temperature controlled box. The fill valve was then opened to begin pressure-time measurements, and the reference cell of the permeameter was filled with helium at an initial pressure of about 200 psig (1.4 MPa). The measurement valve was then opened for the helium to expand and flow into the sample cell.

Pressure drops rapidly as the gas fills the headspace and declines more slowly as the gas enters the shale matrix. Fisher et al. (2017) have suggested that the sudden drop in pressure is a result of gas compression and and that the Joule-Thompson effect is a minor component. Pressure-time data were recorded for 2,000 s following the release of gas into the sample cell. This is the set run time for the SMP 200 permeameter. Five replicate runs were performed on each sample to ensure that results were repeatable (Appendix A; Fig A - 1). After each run, a pressure-time curve was displayed (Fig II -3), and the basic data were offloaded into spreadsheets. Permeability values were initially obtained by curve fitting using the pressure-decay software that Core Laboratories provides with the SMP 200. Late time analysis (Cui et al., 2009) also was used to estimate permeability, as were various exponential and hyperbolic curve fitting techniques.

Three distinct curve segments are observed when applying the techniques of Cui et al. (2009) to pressure decay results (Fig II -4). The first segment, commonly called the early time segment, exhibits hyperbolic decay (decreasing decay rate), whereas the second segment, which is called the late time segment, exhibits exponential decay (constant rate of decline). Pressure appears to equilibrate late in the test, and this third segment is commonly referred to as pseudo-steady equilibrium (Cui et al., 2009; Pacheco-Roman and Hejazi, 2015).

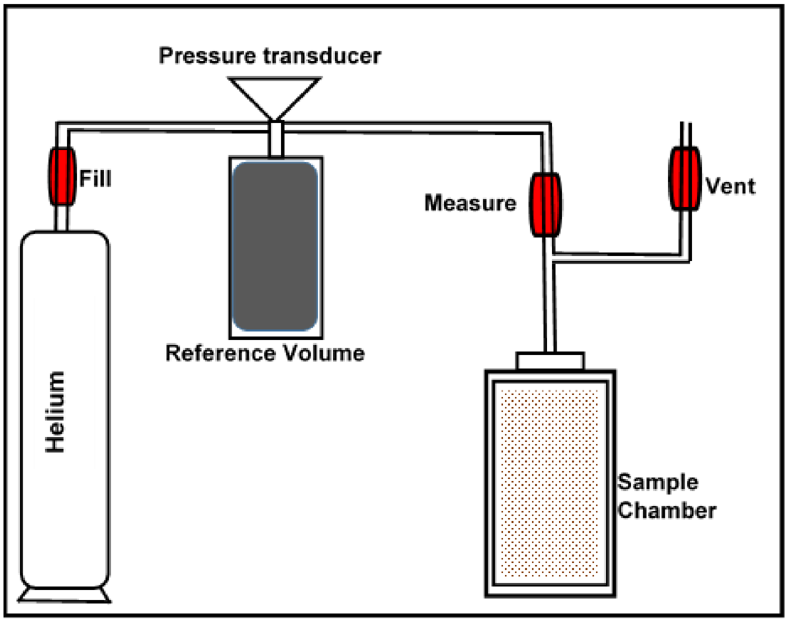

Fig II -2. Schematic diagram of the shale matrix permeameter (SMP 200).

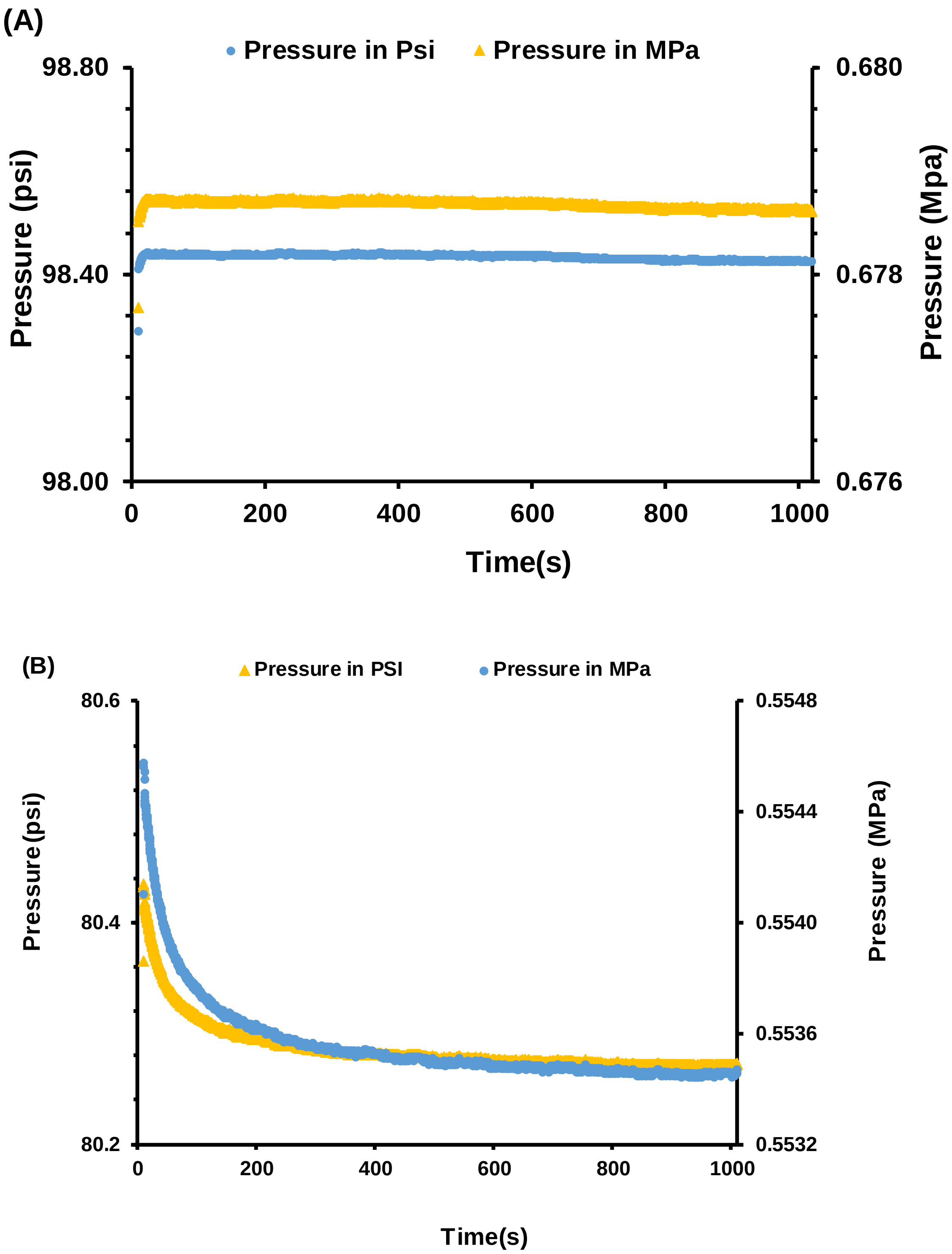

Fig II -3. Example pressure-decay curve derived from from (A) glass beads and (B) crushed shale in the SMP 200 shale matrix permeameter.

Data were reduced for curve analysis using the procedures of Cui et al. (2009), where Ln FR is calculated and plotted against time (Fig II -4). Ln FR is the natural logarithm of the gas fraction in the void volume of the system that will flow into the shale matrix. The slope (S_1) of Ln FR is entered into eq (1) to estimate permeability,

$$k = \frac{R^2\, \emptyset \mu c_g\, S_1}{\alpha^2} \tag{1}$$

where k is the permeability of the shale particles, S_1 is the slope of the decay curve, Ø is shale porosity, µ is the viscosity of the permeating fluid, c_g is the gas compressibility, and α is the first root of equation (2).

$$tan\alpha = \frac{3\alpha}{3+\alpha^2 K_c} \tag{2}$$

$$K_c = \frac{\rho_b V_c}{M\emptyset} \tag{3}$$

$$V_c = V_r + V_s - V_b \tag{4}$$

K_c is the ratio of the gas storage capacity of the void space in the reference and sample holders to the total void space in the sample particles. Vc is the total volume of open space in the reference and sample cell. Vr is the volume of the reference cell, ρ_b is the bulk density, M is the mass of the sample and Ø porosity. The value of Kc either increases or decreases the exponential segment obtained from the solution of the LnFR vs time plots used for permeability estimation, and additional details are found in Cui et al. (2009). Also, the mass of the sample in sample holder of the SMP 200 is required to calculate Kc, as is discussed later in this work.

Using eq (1) for early time analysis, the slope of the tangent of the hyperbolic curve segment is S_1 (Fig II -4). For late time analysis, by contrast, S_1 is the slope of the exponential segment.

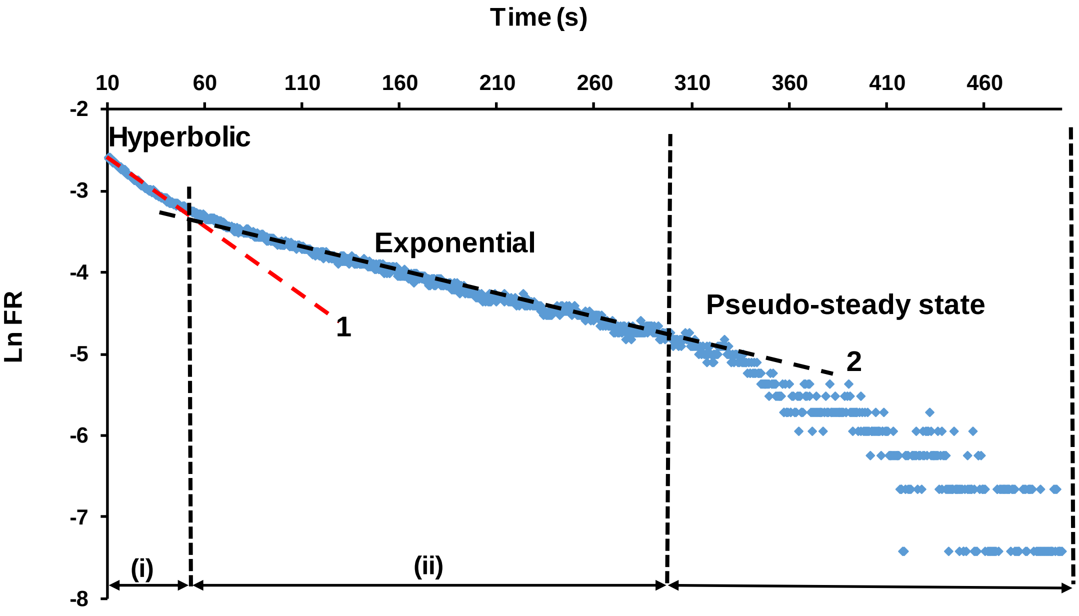

Fig II -4. Example plot of time versus Ln FR with (i) early time or hyperbolic segment (ii) late time or exponential segment and (iii) pseudo-steady-state equilibrium (i.e., unstable or unresolved segment). The sample particle size is 1 mm and is from the Danker #1-28 core at depth 4907 ft (1495.7 m).

3.1 Results

3.2 Rock properties

The Woodford Shale in the Danker #1-28 core is composed of fine-grained, dark gray to very dark gray silty shale and shaly siltstone (Fig II -5). The shale is laminated, and the dark color owes to elevated organic matter and pyrite content. Paper-thin pyrite laminae with variable continuity are abundant and are a distinctive feature of the core. Marcasite nodules are common, and thin marcasite bands are developed locally. Fossil content includes abundant *Tasmanites* algal cysts, sparse conodont elements, and radiolarian tests; bioturbation is sparse. A synsedimentary fault is in the upper part of the core at a depth of 4901 ft (1494 m). Minor faults with slickensides were observed between 4908 and 4914 ft (1496-1498 m).

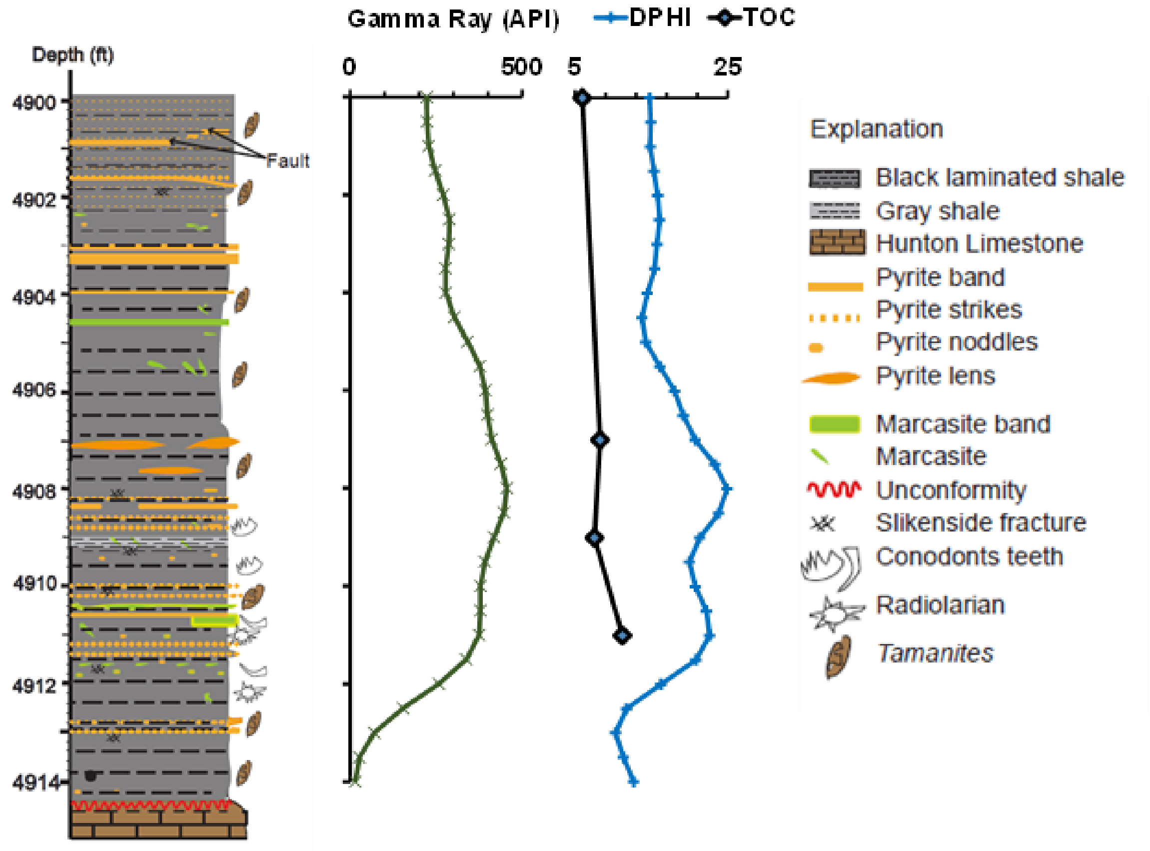

Fig II -5. Graphic log of the Woodford Shale in the Danker #1- 28 core accompanied by, gamma ray, total organic carbon, and density porosity curves.

The gamma ray (GR) values in the Woodford core are greater than 150 API units with a peak value of 475 units at 4908 ft (1496 m) (Fig II -5). Density porosity increases from 2.0% at 4900 ft

(1493.5 m) to a peak value of 25.0 % at 4908 ft (1496 m) then decreases to 1.0% at 4914 ft (1498 m) and TOC concentrations from 5.6 % to 11.2 %.

Dean-Stark analysis of fluid saturation indicates that water, oil, and gas saturation fall in a narrow range in the samples analyzed (Table 3). More data on porosity from sample 2 is found in Appendix A (Table A-1).

Table 3: Bulk density, porosity and fluid saturation of samples1, 2, 3 and 4 used for studies.

			Trican		Terra Tek	Saturation		
Sample ID	Depth (ft)	Depth (m)	Bulk density (g/cc)	Total Porosity %	Bulk density (g/cc)	Water (% PV)	Gas (% PV)	Oil (% PV)
Sample 1	4900-4902	1492.13 - 1494.13	2.45	2.54	2.50	62.8	31.5	5.71
Sample 2	4904-4907	1494.74 - 1495.65	2.45	2.49	/	/	/	/
Sample 3	4907-4909	1495.65 - 1496.26	2.36	4.03	/	/	/	/
Sample 4	4909-4911	1496.26 - 1496.87	2.26	4.14	2.32	54.21	39	6.78

Rock-Eval pyrolysis data indicate organic matter in the Woodford Shale in the Danker #1-28 core, has a bulk composition equivalent to type II kerogen. In terms of thermal maturity (Table 4), T_{max} averages 429°C, suggesting it is near the lower margin of the oil window. The calculated vitrinite reflectance (R_o) value is 0.56 %, which is comparable to optically measured R_o values from Woodford Shale in Lincoln County, Oklahoma (Cardott, 2012).

Table 4: Summary of Rock-Eval pyrolysis results from the Danker #1-28 core.

Sample ID	Depth (ft)	Depth (m)	S1 (mg/g)	S2 (mg/g)	S3 (mg/g)	T_{max} (ºC)	HI	OI	PI
Sample 1	4900-4902	1492.13 - 1494.13	1.78	29.57	0.28	429	497	5	0.06
Sample 2	4904-4907	1494.74 - 1495.65	2.04	40.31	0.34	426	489	4	0.05
Sample 3	4907-4909	1495.65 - 1496.26	1.87	37.24	0.37	429	495	5	0.05
Sample 4	4909-4911	1496.26 - 1496.87	2.27	57.80	0.37	429	516	3	0.04

3.3 SEM results

SEM images of ion milled core samples reveal a heterogeneous fabric dominated by clay, silt, pyrite, and organic matter (Fig II -6). Platy clay particles are elongate parallel to bedding, whereas silt grains have variable roundness, angularity, and sphericity. Pyrite is dominantly framboidal and images as bright elements in backscattered SEM images. Organic matter images as dark masses and includes amorphinite filling the interstices between mineral particles and larger masses constituting cysts. Most pores are too small to be imaged by SEM, although clusters of open pores with a diameter less than 0.5 μm are imaged locally (Fig II -6B).

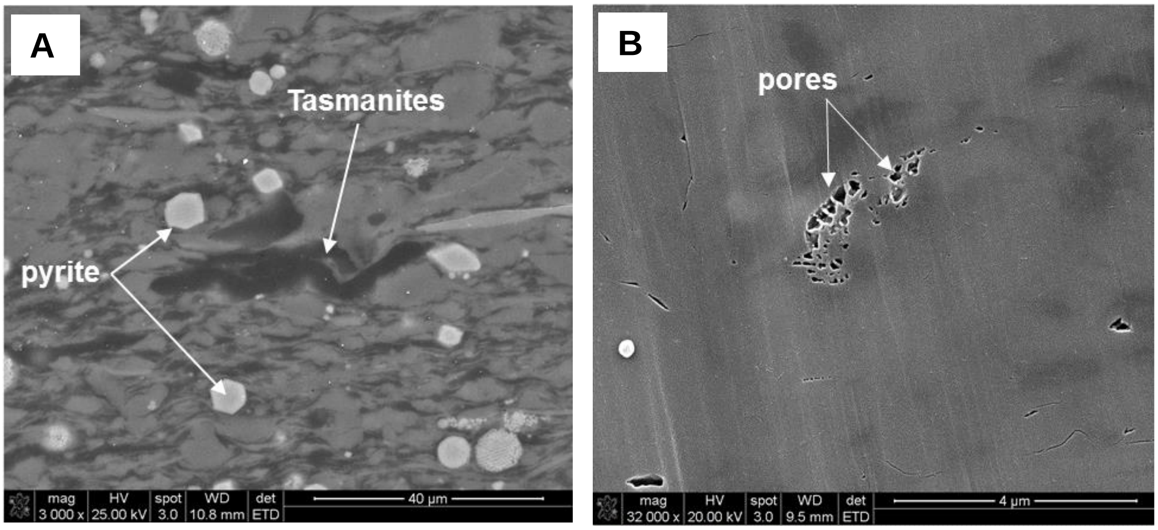

Fig II -6. SEM images of the Woodford Shale in the Danker #1- 28 core from 4910 ft (1496.6 m). (A) Image showing typical rock fabric. (B) Image showing cluster of open pores.

Microfractures were observed in all SEM images of the particles in each size class analyzed. The aperture of the microfractures measured from the images is between 60 to 1020 nm (Fig II -7). Many of the fractures appear to develop within grains, and a few follow the margins of the grains.

Those within grains are ostensibly the result of mechanical breakage during crushing, whereas those forming rims may be fissures formed by desiccation of hydrous clay minerals and kerogen. No trends were observed in the abundance and frequency of microfractures relative to particle size. More samples with microfracture can be seen in the Appendix Z (Fig.A-2).

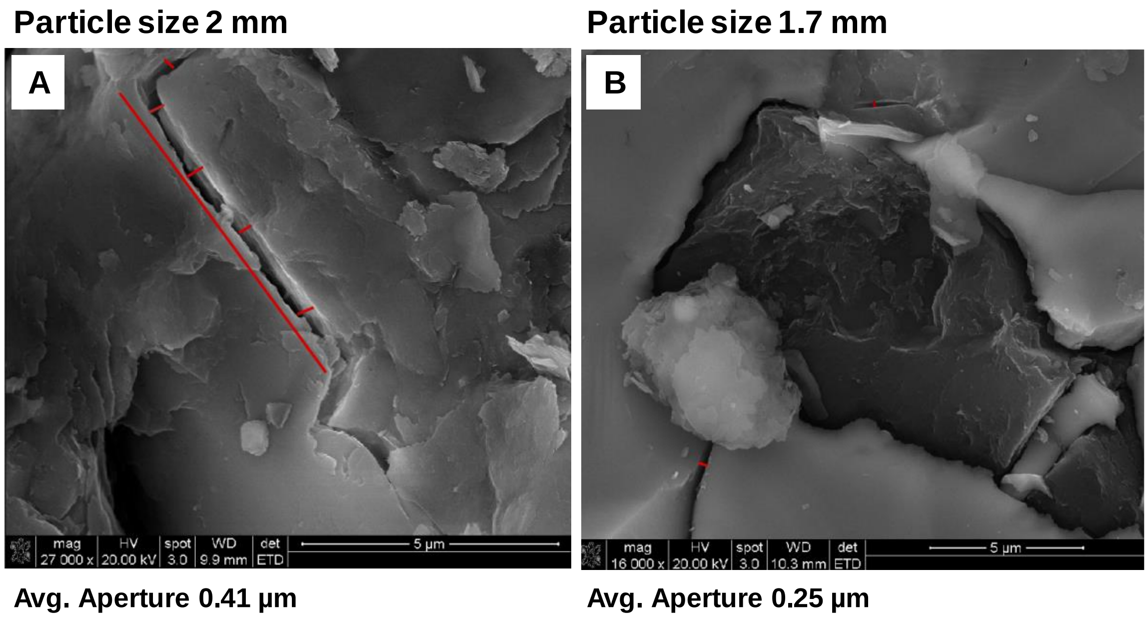
Particle size 2 mm

Particle size 1.7 mm

Avg. Aperture 0.41 µm

Avg. Aperture 0.25 µm

Fig II -7. Scanning electron microscope images of open microfractures (A) within a clay particle and (B) rimming a grain.

3.4 Porosity Results

Porosity, as determined using a pycnometer, averages 2.5% in samples 1 and 2 (Fig II -8). In these two samples, a variation of measured porosity is insensitive to particle size. Porosity is higher in samples 3 and 4. These samples do show an inverse relationship between measured porosity and particle size, with porosity decreasing from 4.6 to 3.4%, respectively.

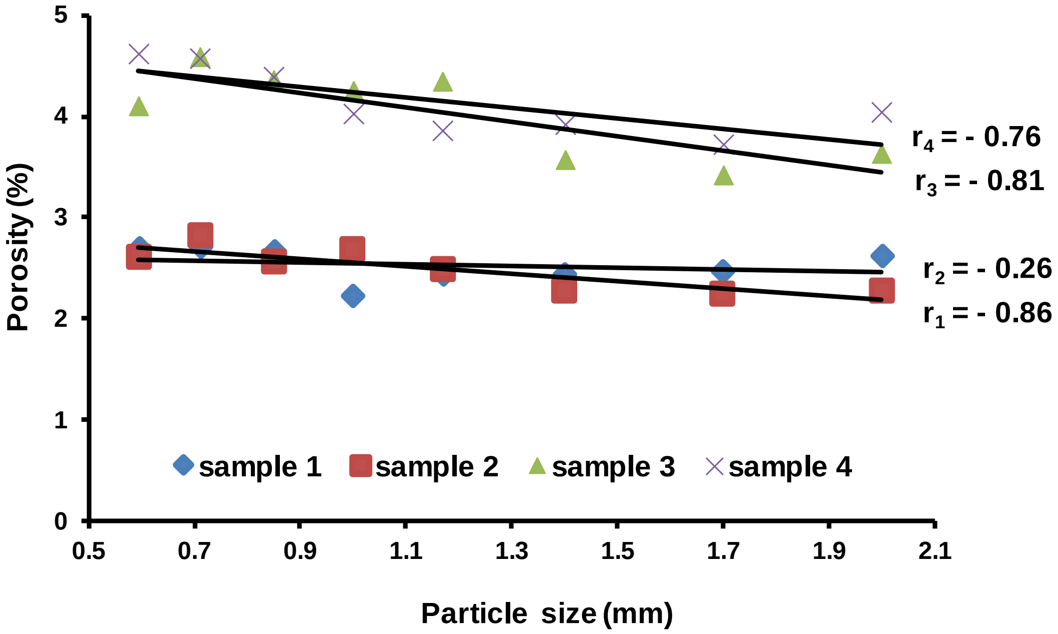

Fig II -8. Plot of porosity vs. particle size in selected Woodford shale samples. Porosity is effectively constant in particle sizes for sample1 and inversely related in sample 2, 3 & 4. Results from Trican Lab.

3.5 Transient permeability values

Permeability values determined using the whole curve analysis method vary depending on how much of the curve is fit (Fig II -9) and the time window analyzed. Each partial curve determination yields a different permeability value. Permeability numbers are highest for short time windows between 0 and 40 to 60 s and decrease as the upper limit of the time window increases toward 500 s. The data beyond 500 s are typically considered noise in most cases or cannot be resolved by the equipment. Sample 2 (Fig II -9), shows how permeability decreases from 10.2 nD to 0.6 nD as the time window increases from 0-40 s to 0-800 s (Appendix A; Fig. A-3). Interestingly, permeability values for each time window vary little with changing particle size.

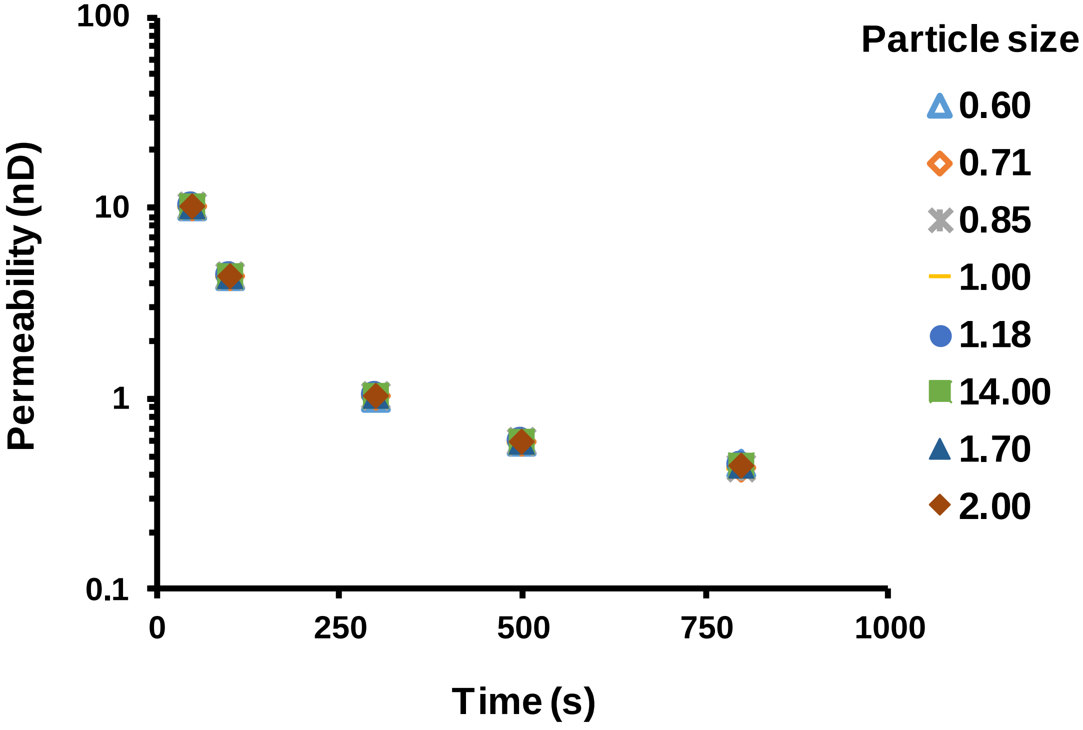

Fig II -9. Permeability vs. time plots from whole curve analysis of sample 2.

For LnFR vs. time plots (Cui et al., 2009), the duration of measurements depends on the particle size, the amount of sample in the sample holder, and Kc. These variables contribute to the geometry and duration of the exponential decay segments but do not influence the hyperbolic segment. Specifically, the exponential segment increases in duration as the mass in the sample holder increases from 15 g to 100 g then begins to decrease as the sample approaches the brim of the sample cell (Fig. 10). See Appendix A (Figs. A-4 to A-7 for additional data. For very small masses in the sample holder (less than 30 g), the exponential decay segment is difficult to discern (Fig II - 10).

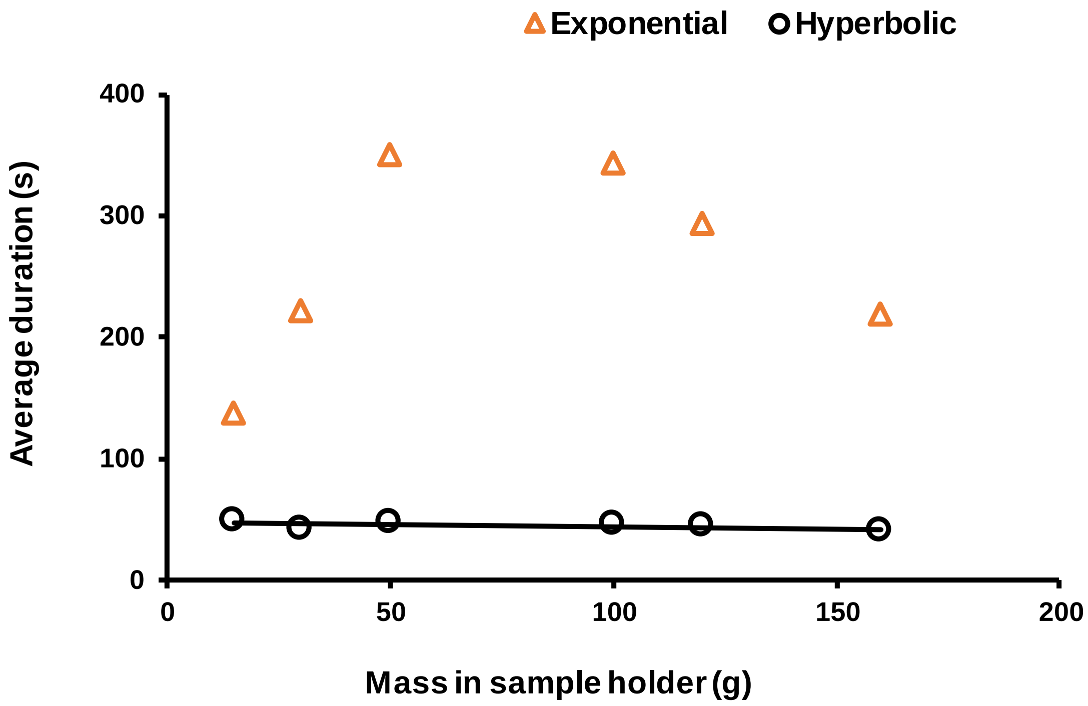

Fig II -10. Average duration of the hyperbolic and exponential decay episodes as the sample holder is filled with different sample masses (Sample 2, particle size = 1.18 mm).

Analysis of sample mass in the sample holder (Fig II -11) indicates that the smallest mass in the sample holder has the largest Kc value, which corresponds to the smallest duration for the measurement of the exponential decay segment (Fig II -10). For identical masses with different particle sizes (

Fig II -*11*B), the Kc values are relatively stable for particle sizes of 0.85, to 1.40 mm, after which it increases (Appendix A; Figs. A-5, A-6).

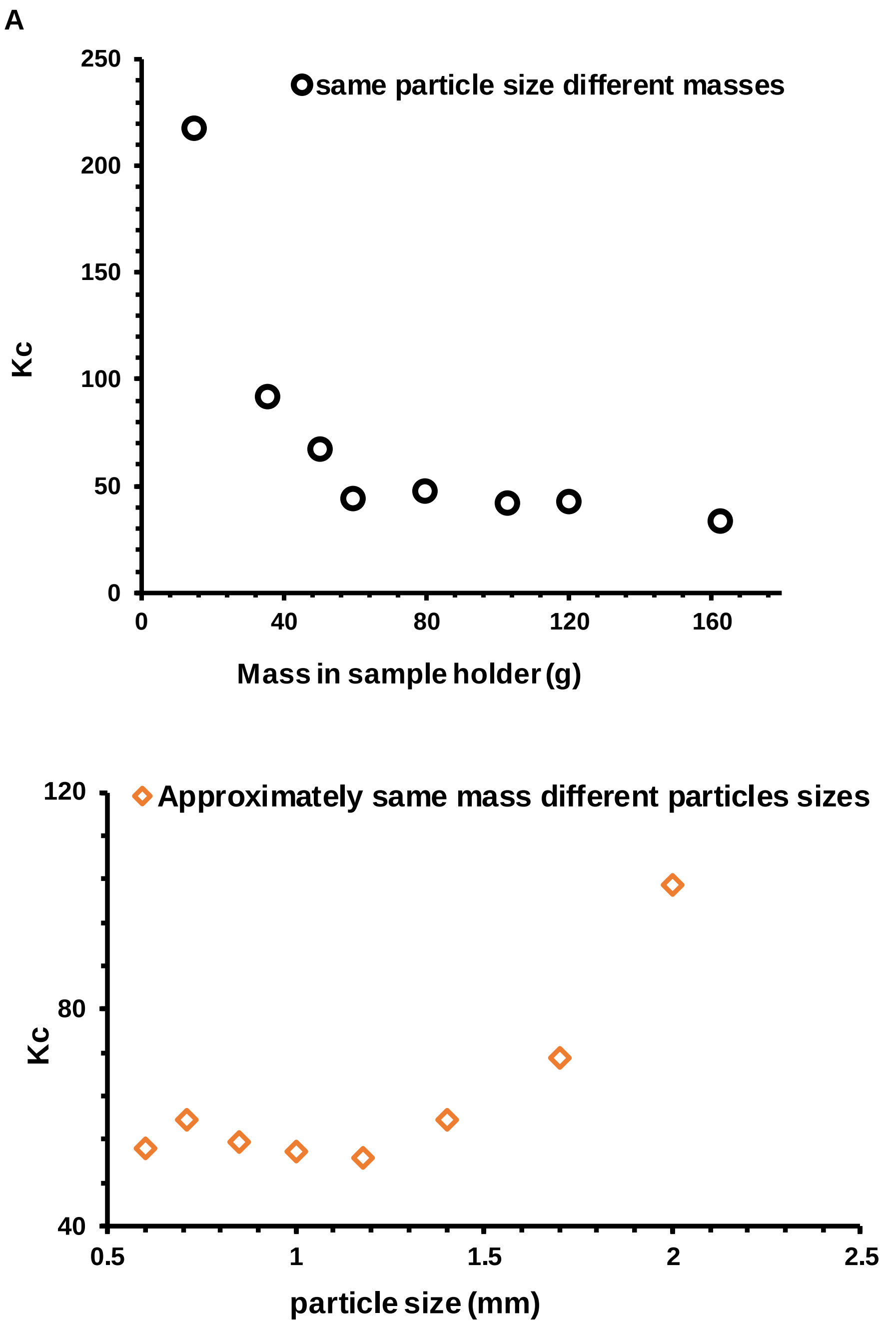

Fig II -11. (A) Mass in the sample holder versus K_c. Mass in the sample holder decreases as the ratio of the gas storage capacity of the void space in the reference and sample holders to the total void space in the sample particles (Kc) also decreases. (B) Plotting Kc versus particle size indicates indicates effective stability at particle sizes smaller than 1.7 mm.

The relationship between Kc and exponential decay duration with the mass of sample in the sample holder is shown in Fig II -12. Kc decreases from 220 to 44 as the duration increases to a maximum of about 400 s for sample masses of 50 g and 100 g then, decreases to 200 s while Kc stays relatively constant (Appendix A; Figs. A-4, A-5, A-6).

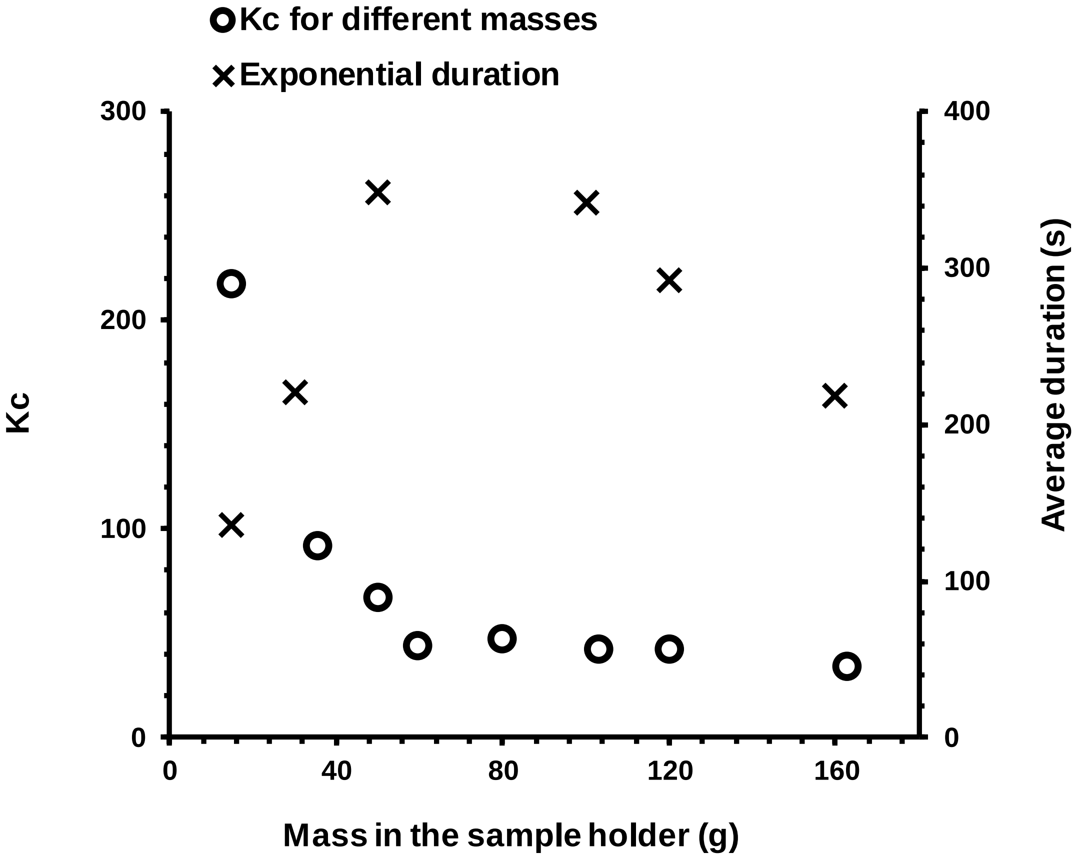

Fig II -12. Variation in Kc and duration of the exponential decay segment as the mass of crushed shale in the sample holder changes.

3.6 Particle size and permeability analysis

3.6.1 Whole curve analysis

Plotting permeability vs. particle size using the whole curve fitting technique for pressure decay yields different results for each sample. Permeability variation in sample 2 is effectively invariant with respect to particle size and has a very weak correlation coefficient (r) of -0.36. Permeability increases with particle size in sample 3 and even more so in sample 4 (Fig II -13) with high regression coefficients of 0.88 and 0.89, respectively.

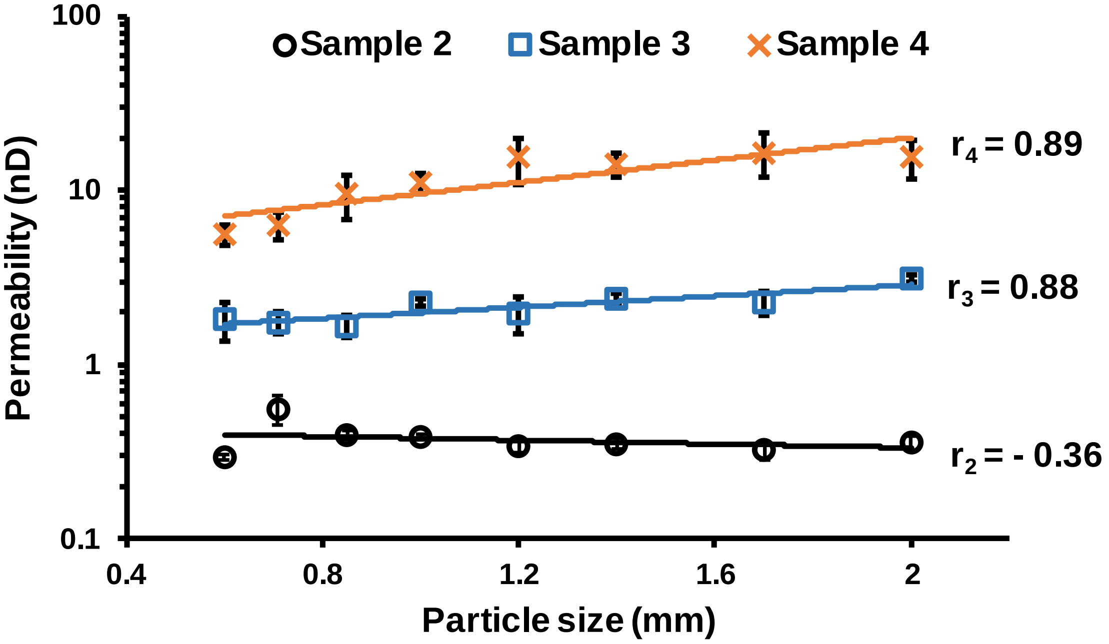

Fig II -13. Variation of permeability with particle size using the whole curve fitting technique employed in the Core Laboratories software that ships with the SMP 200 shale matrix permeameter.

3.6.2 Hyperbolic segment analysis

In the samples analyzed, permeability determined from the early, hyperbolic (Fig II -4) part of the pressure decay curves increases with particle size (Fig II *-14*). Compared to whole curve analysis (Fig II -13, Fig II -14), permeability is two orders of magnitude greater for early hyperbolic time analysis and this is supported by stronger regression coefficient of 0.98, 0.74, and 0.93 for samples 2, 3, 4 respectively. The hyperbolic segment of the LnFR vs. time plot is steeper for larger particles, thus yielding greater slopes corresponding to higher permeability. The hyperbolic segment has a duration between 40-60 s, which is relatively stable but the exponential segment-depends on the measurement duration.

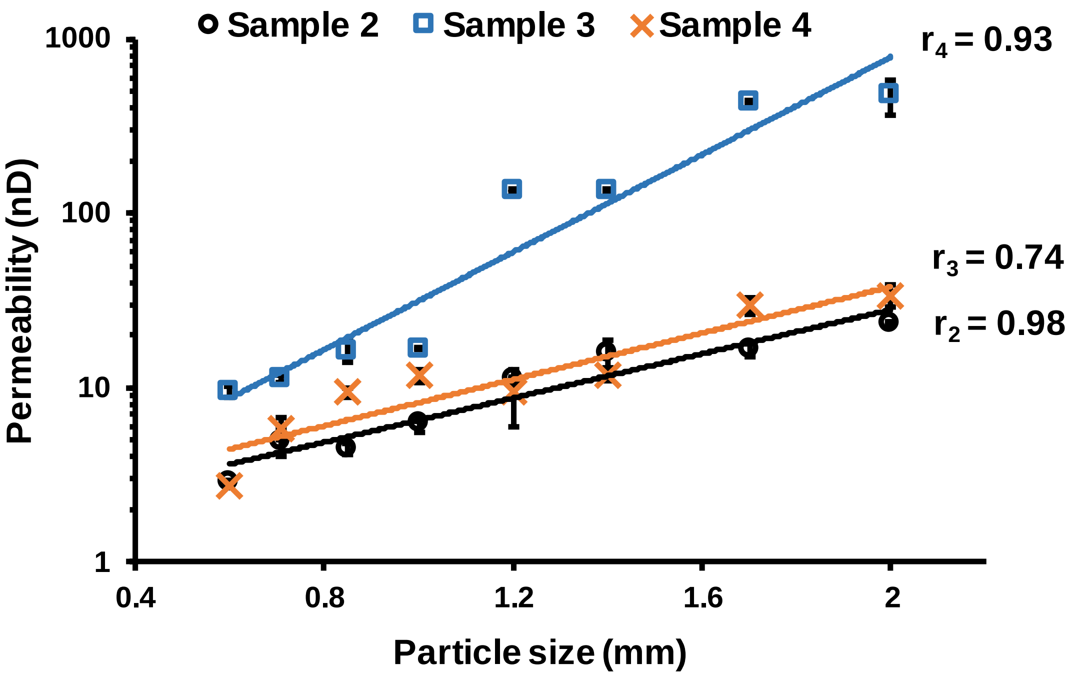

Fig II -14. Variation of permeability with particle size as calculated from the early, hyperbolic segment of pressure-decay curves.

3.6.3 Exponential segment analysis

The permeability values obtained from the late, exponential segment of the pressure decline curves also record increasing permeability with particle size (Fig II -15). There is a strong correlation between particle size and permeability depicted by regression coefficients all greater than 0.5. For each sample analyzed with a duration greater than 500 s, there is a larger exponential segment that permits more accurate determination of the slope.

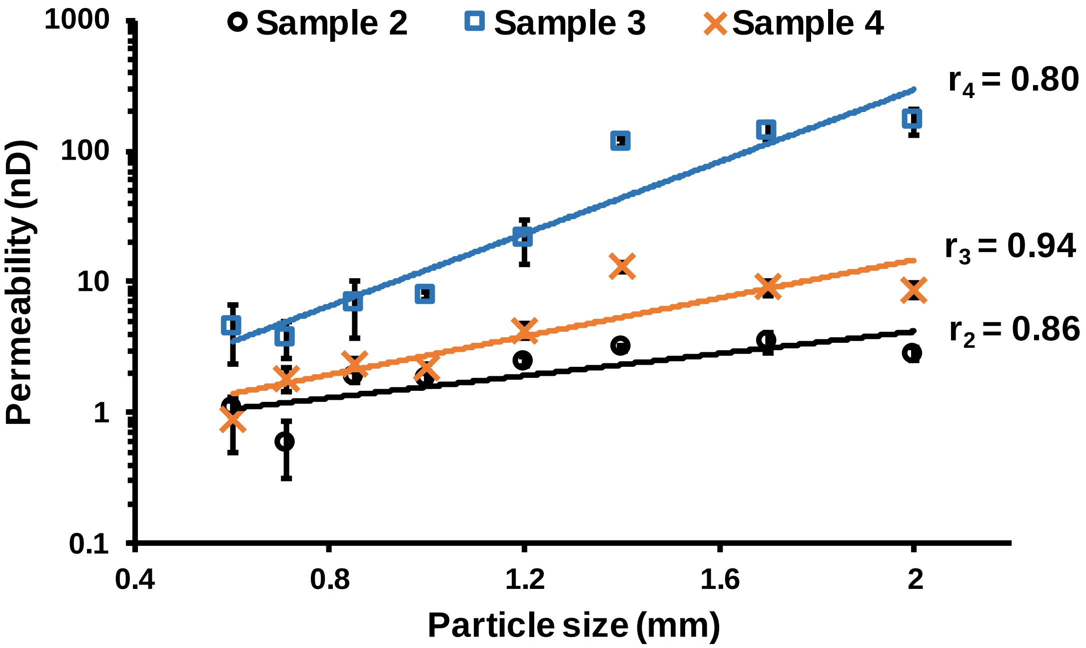

Fig II -15. Permeability vs. particle size determined from the exponential segment ran at measurement duration of, 500 s.

3.6.4 Comparison of permeability calculated using different techniques

Results from analysis of sample 2 portray the relationships among permeability determinations based on different techniques (Fig II -16). Permeability obtained by history matching the complete pressure-decay curve using the Core Laboratories software yields the lowest permeability values of the three methods analyzed here. This is because data from the pseudo-steady equilibrium phase are included in the calculation. Importantly, the values derived from whole curve fitting exhibit low sensitivity to particle size.

Permeability values reported by late time exponential analysis of the pressure decline are one to two orders of magnitude greater than those derived by whole curve analysis (Fig II -16). As mentioned earlier, these results are strongly sensitive to particle size. Values derived from the exponential decay curve segment with measurement duration of 500 s, are intermediate. In sample 2, results from the whole curve analysis are insensitive to particle sizes with a regression coefficient of -0.36. By contrast, results from the late exponential and early hyperbolic segments are more sensitive to particle size while those derived from whole curve analysis are not sensitive to particle size.

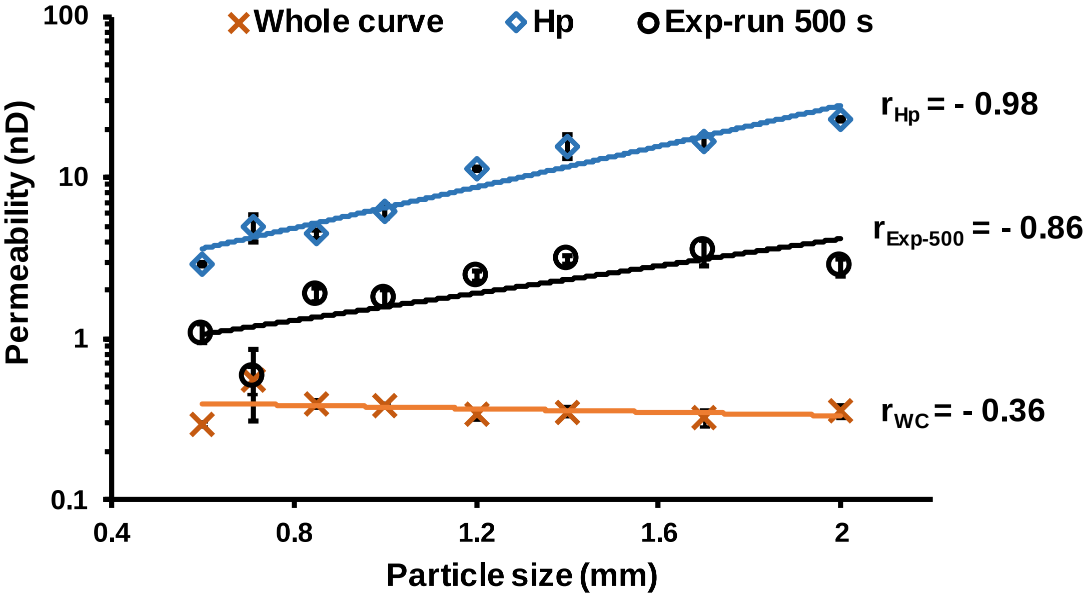

Fig II -16. Variability of permeability with particle size as calculated using three different methods in sample 2. Whole curve (WC) values were derived by analysis of the complete pressure-decay using Core Laboratories software, late time exponential (Exp) and early hyperbolic (Hp) segments are calculated from LnFR vs time plots.

4.0 Discussion

A key result of this research is that different techniques used to interpret pressure decay curves yield disparate results. Our experiments with the SMP 200 indicate that crushed-rock pressure decay tests are repeatable and that temperature regulation was the key to obtaining consistent results

(See Appendix A; Fig A - 8). The complexity lies in the interpretation of the pressure decay curves, and each method has distinct pros and cons.

The whole-curve history matching algorithm implemented by Core Laboratories yields the most consistent results across the particle size range analyzed. However, permeability determinations can vary significantly depending on what part of the curve is interpreted, and so interpretation of partial curves does not yield stable results (Fig II -9). Moreover, the permeability determination is strongly affected by the inclusion of late-stage pseudo-steady state data, which typically lie between 40 s and 500 s duration and beyond (Fig II -3, Fig II -4). And so the resulting permeability values are very low and arguably include a large fraction of data with limited value for decay curve interpretation. These values from the exponential segment, however, are on the order of those obtained by applying pulse decay methods to core plugs (e.g., Hannon, 2016). Nevertheless, Ghanizadeh et al. (2015a), Ghanizadeh et al. (2015b), Cui et al. (2013), Cui and Brezovski (2013), Tinni et al. (2012), Suarez-Rivera et al. (2012) have reported differences between crushed permeability and plug permeability for identical samples.

The interpretation of the hyperbolic segment of the pressure decay curve was used to determine permeability based on the LnFR vs. time plot. This technique constitutes an interpretation of the hyperbolic segment (Fig II -4) rather than the exponential segment of the LnFR vs time. The results yield the highest permeability values of the three techniques used here, as well as a marked sensitivity of results to particle size (Fig II -13, Fig II -16) and mass of sample in the sample holder. An advantage of the technique is that results can be obtained rapidly since the measurement time is about 40 s. A limitation, however, is that the results may be influenced significantly by microfractures induced by crushing the sample. Indeed, SEM analysis confirms the presence of microfractures in all the samples that were analyzed during this study (Fig II -7; Appendix A, Fig.

A-2), and Tinni et al. (2012) observed similar factures in particles that were scanned by CT following impregnation with mercury.

The region where Kc is relatively stable corresponds to the largest exponential duration and sample masses of 50 and 100 g (Fig II-11, 12 and 13). This region is considered the most reliable for the determination of the slope of LnFR to estimate permeability (Fig II -10, 11 and 12). Cui et al. (2009) have shown a correlation between Kc and the analytical solutions of pycnometer experiments where Kc values greater than 50 were shown to have a log-linear FR function. Our results show that Kc does not only need to be greater than 50 as suggested in Cui et al. (2009) paper, but depend on the mass in the sample holder and for the SMP 200, masses less than 50 yield very large Kc values but small exponential segments for proper analysis of permeability (Appendix A; Figs. A-4, A-5).

Permeability interpreted from the exponential segment of the pressure decay curve (Fig. 4) yields intermediate permeability values, which are sensitive to particle size (Fig II -15), and running the experiment for 500 s was sufficient to resolve the exponential part of the curve. The uniform slope of the curve in plots of LnFR vs. time results in a stable and thus reliable permeability value. More plots of LnFR vs time are in Appendix A (Figs. A-5, A-6). One issue is that decay curves with a short exponential segment may yield results with less certainty than those with a longer segment, where the slope of the LnFR vs. time plot is more tightly constrained. A point of caution is that permeability determined from the exponential decay segment may represent filling of microporosity and nanoporosity and may exclude the effects of gas filling and moving through larger pores, which may be an essential aspect of reservoir performance. Also, the length of the exponential segment depends on particle size, the mass of sample in the sample holder, and measurement duration. Particle sizes between 1 and 1.4 mm have a stable exponential segment, and this is supported by a Kc value lying with the stable range in (Fig II -11)

O'Connor and Seidle (2011) noted that early decline of many shale wells is hyperbolic, whereas later decline as wells reach maturity is commonly exponential. Although it is impossible to draw a direct parallel between a well and a permeameter, one possibility is that the hyperbolic decline is influenced by hydrofractures and large pores close to the fracture surfaces, whereas late-stage exponential decline more closely reflects the effects of desorption and diffusion of gas from deep in the nanoporous framework of shale. Because of this, it appears that values determined from the hyperbolic and exponential portions of LnFR vs. time plots each have value, and reporting both numbers is worthwhile.

Permeability in the samples analyzed correlates positively with TOC content, confirming that storage within the microporous organic framework of kerogen has a strong effect on permeability (e.g., Loucks et al., 2012). A decrease in measured porosity with increasing particle size (Fig II -*8*) is attributed to smaller particles having a proportionally larger surface area because of fracturing and perhaps other damage during crushing. Tinni et al. (2014) also observed that porosity increases with decreasing particle size. Ghanizadeh et al. (2015) has suggested that crushing of cores increases accessibility of fluids to pore and pore connectivity. Profice et al. (2012) demonstrated that pressure decay is influenced more by porosity than intrinsic permeability. Accordingly, accurate measurement of effective porosity is essential for pressure decay permeability analysis. The SMP 200 apparatus used in this study performs pressure decay tests at low pressure, and so gas slippage (a.k.a., the Klinkenberg effect) is an important consideration for interpreting results (Gensterblum et al., 2015; Profice et al., 2012; Sondergeld et al., 2010). Initial reservoir pressure can be several MPa and declines throughout the productive life of a well. Hence, Klinkenberg and in-situ “effective stress” corrections are essential for relating low-pressure permeameter results to real-world reservoir performance, and the laboratory results reported here are most directly applied to late-life reservoirs where pressure has been depleted. Importantly, most laboratories run pressure decay tests at different operating pressures and temperatures, and so care must be taken when comparing data from different laboratories.

What particle size class should be used for analysis has long been a central question regarding permeability determination from tight rocks (e.g., Luffel et al., 1993; Cui et al., 2009, Suarez-Rivera, 2012; Profice et al., 2012), and there is no simple answer to this question. Profice et al. (2012), Cui et al. (2009), and the current study show that permeability depends on particle size, porosity and TOC content of the samples. The maximum 2.0 mm particle size used in this study was dictated by the Core Laboratories software, and future investigations should focus on LnFR vs. time analysis of even larger size fractions to better understand the range and utility of possible test results.

If porosity is high and particle size is small, it is difficult to obtain robust pressure-decay curves. Also, pressure fluctuations associated with valve actions within the permeameter and induced temperature effects from the rapid expansion of gas into the sample chamber can affect measurement and reproducibility (Profice et al., 2012). Analysis time is different among nearly all investigators (e.g., Tinni et al., 2012; Sakhaee-Pour and Bryant, 2012; Heller et al., 2014; Peng and Loucks, 2016), and so it is desirable to use methods with minimal sensitivity to run time. This was a particular problem with the whole-curve history matching approach (Fig II -9). Based on our results from the SMP 200, data should be recorded for about 500 s, and it is important to define the boundaries among the hyperbolic, exponential, and pseudo-steady state decay curve segments and to be clear about how the decay curve was analyzed relative to these segments.

5.0 Conclusions

This research assessed some techniques used in the analysis of pressure decay curves and indicates that care must be taken when comparing permeability from different analytical datasets, as the data might have been generated and interpreted by different techniques. Permeability from the hyperbolic pressure decay segment is highest, whereas that from the exponential segment is intermediate, and values determined from the whole curve yield the lowest values. Permeability is influenced by measurement duration, the mass of sample in the sample holder, pressure variability from different laboratories, particle size, and the presence of microfractures. For more reliable matrix permeability results from the SMP 200 shale matrix permeameter, measurement duration should be greater than 500 s.

It is useful to report the permeabilities obtained from both the hyperbolic and exponential segments of LnFR vs. time plots. However, permeability from the hyperbolic segment is always higher than that from the exponential segment. Permeability determined from the hyperbolic segment is influenced by microfractures, larger pores and crushing-related particle damage and is thus not fully representative of the matrix permeability. All particle sizes of the crushed shale investigated had microfractures with average aperture ranging from 60 to 1020 nm but showed no correlation between particle size and fracture width. The mass of the sample in the sample holder and Kc significantly influence the slope of LnFR vs time and thus affect the permeability determination.

Acknowledgments

This paper is based on Doctoral research at Oklahoma State University (Achang). This work was supported in part by grants from the Oklahoma Geological Foundation, Society of Petrophysical Well Log Analysis (SPWLA), and National Association for Black Geologists. Trican

Geological solutions contributed data and analytical services to this study. We thank Jim Puckette for providing access to the Danker #1- 28, Lincoln County Oklahoma, USA and Eliot Atekwana for constructive comments on an early draft of this manuscript. The authors are grateful to the reviewers, who made numerous suggestions that improved the quality of this contribution.

Appendix A

Sample 2_2 mm

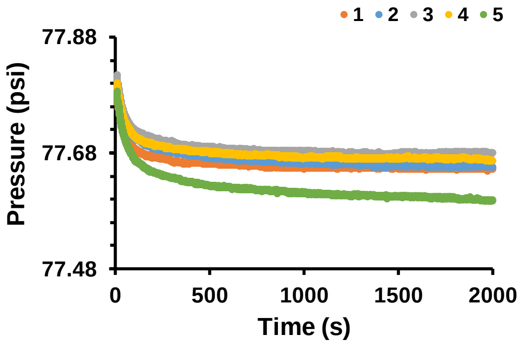

Sample 2_1.7 mm

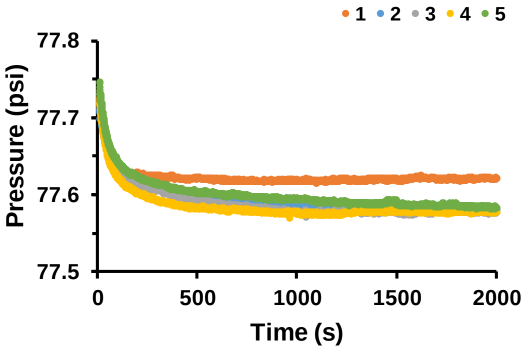

Sample 2_1.4 mm

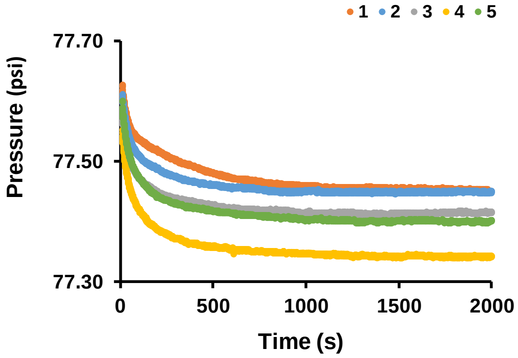

Sample 2_1.2 mm

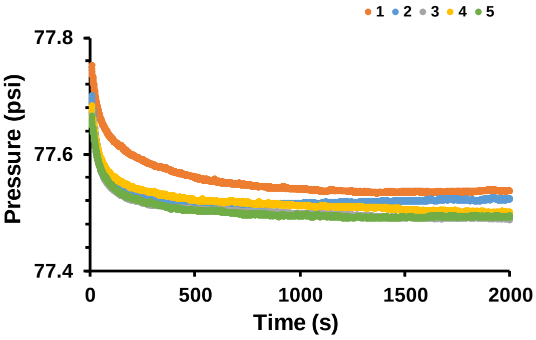

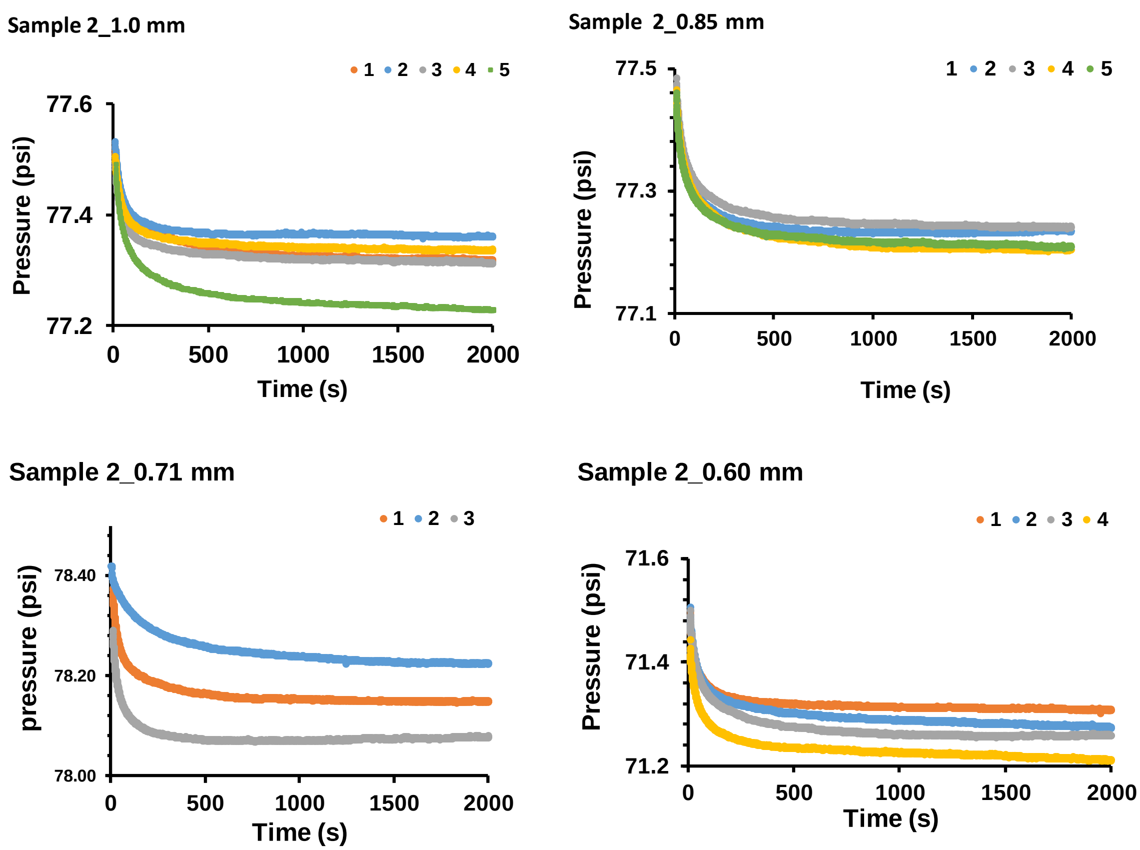

Fig A - 1. Pressure decay graph of sample 2 at depth 4904 ft for particle sizes of 2.0, 1.70, 1.40, 1.20, 1.00, 0.85, 0.71, and 0.60 mm respectively. The Total Organic Content (TOC) at this depth is 8.25 %.

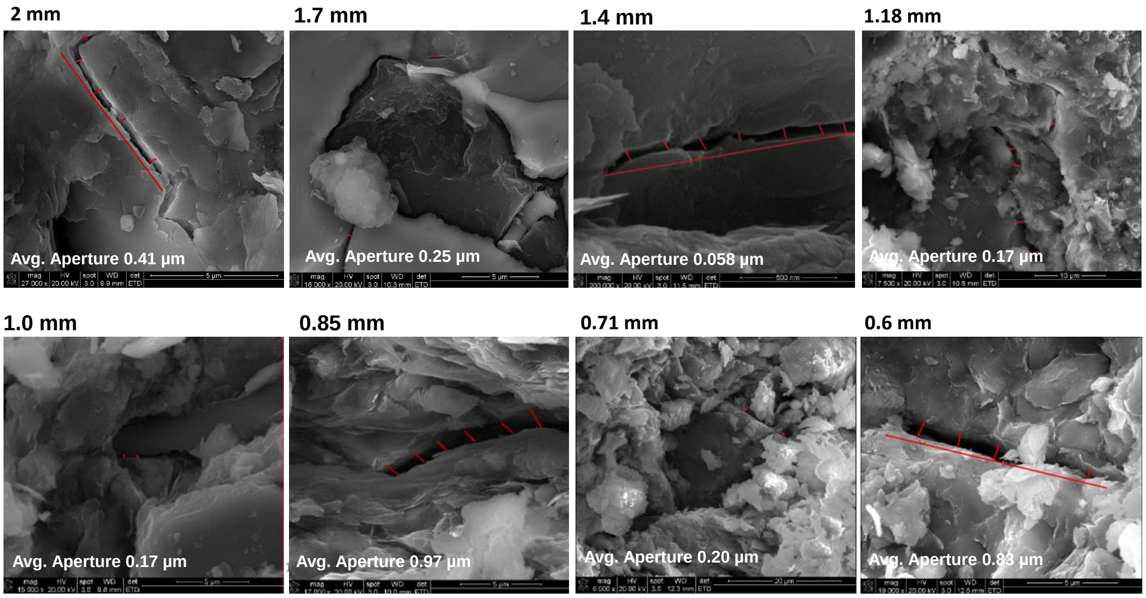

Fig A - 2. SEM images of Woodford Shale in the Danker 1-#28 core indicating microfractures and average apertures.

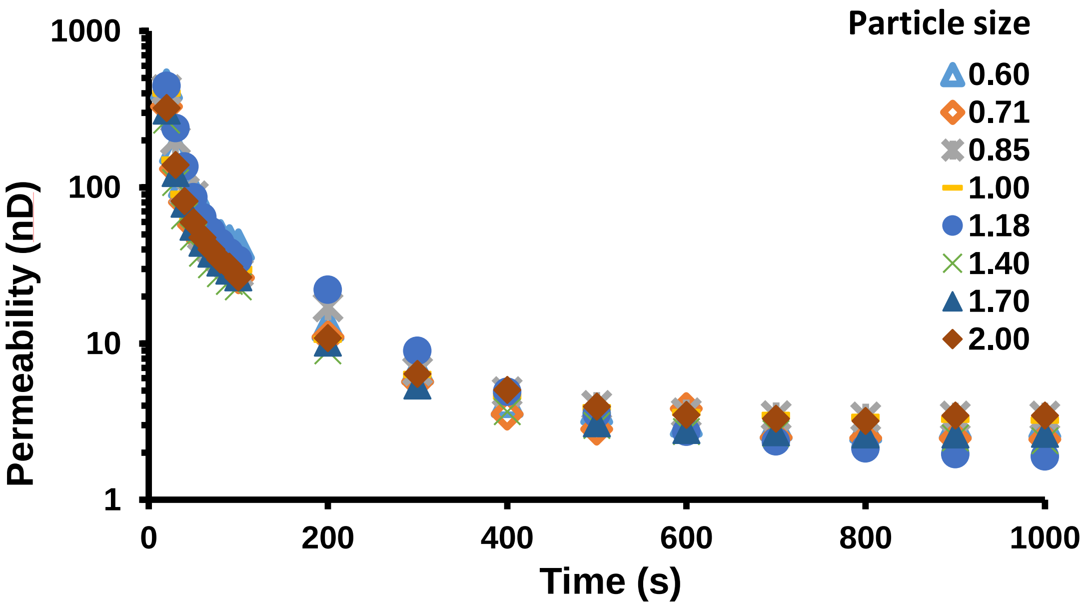

Fig A - 3. Variation in permeability with time when whole curve analysis is used to determine permeability.

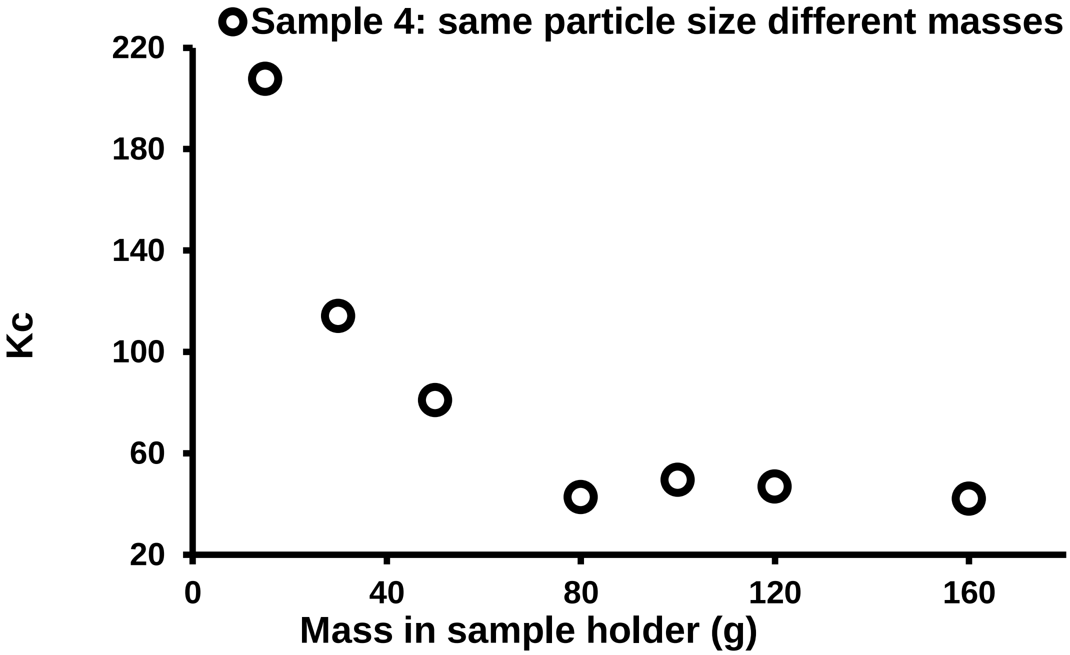

Fig A - 4. Plot of change in Kc as mass in the sample holder changes for sample 4.

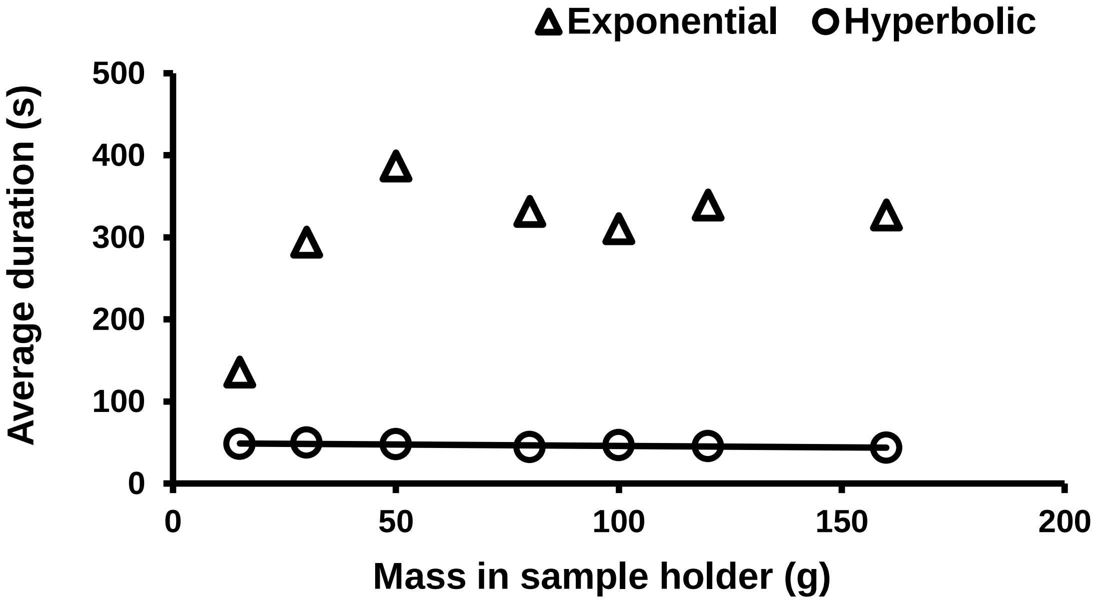

Fig A - 5. Average variation in duration with increase in particle size for sample 4 at depth 4909-4911 ft.

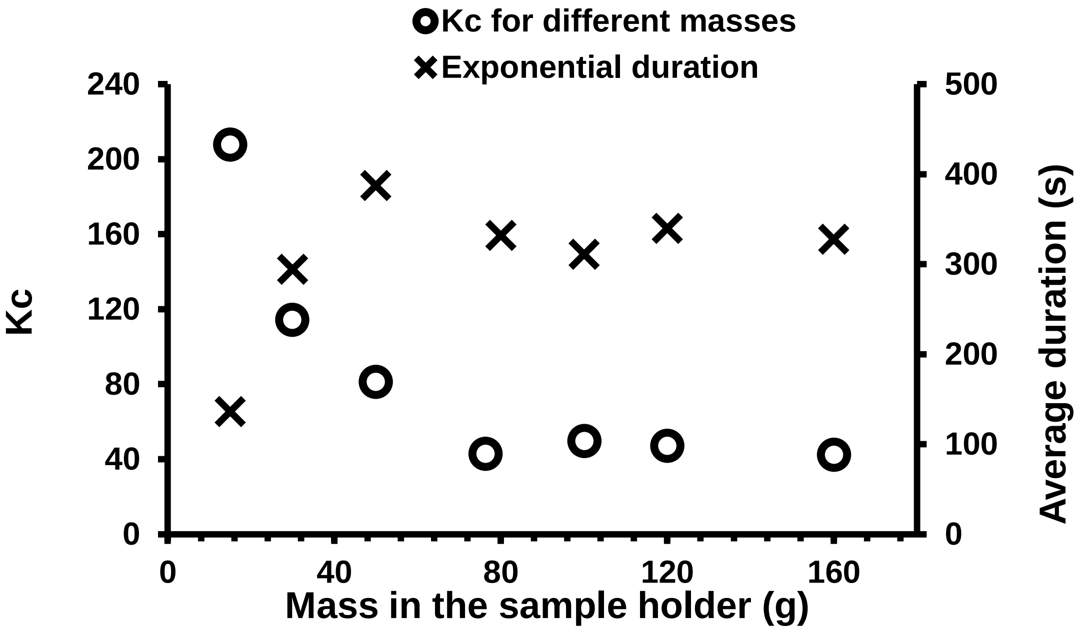

Fig A - 6. Variation of Kc with exponential duration and mass in the sample holder.

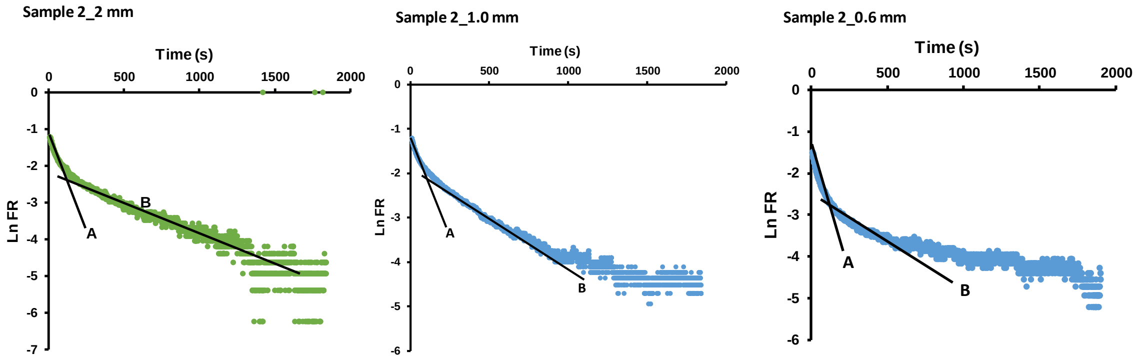

Fig A - 7. Plot of LnFR vs. time for particle size 2 mm, 1.0 mm and 0.6 mm at depth of 4904 ft. Line A indicates the hyperbolic segment while line B indicated the exponential segment.

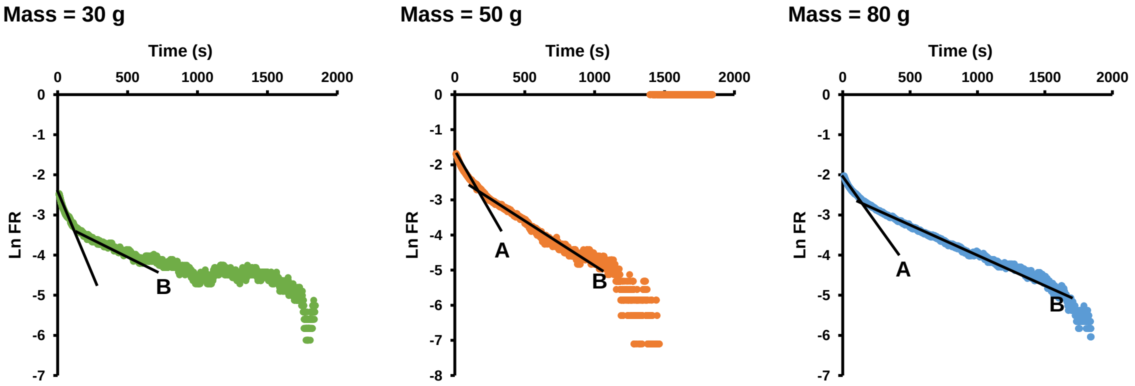

Fig A - 8. Plots of LnFR vs. time and mass variation of mass in sample holder

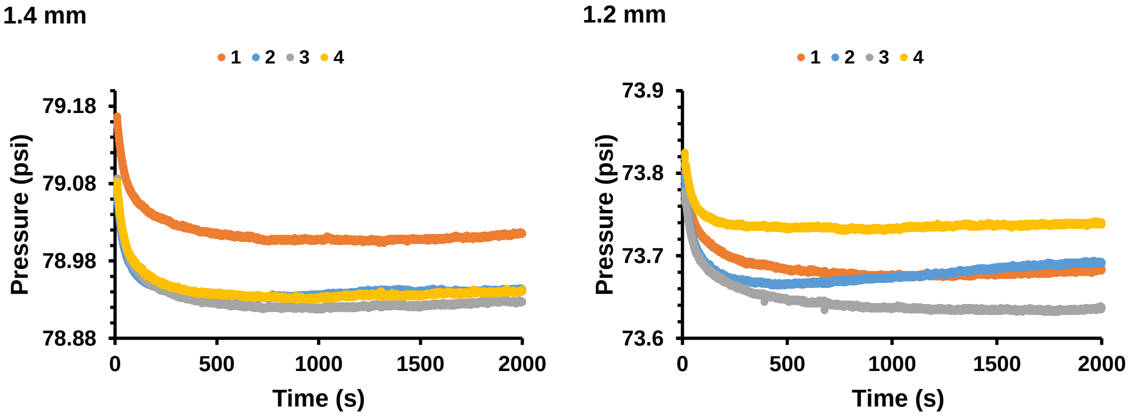

Fig A - 9. Pressure decay graph of sample 4 at depth 4909-4911 ft for particle sizes 1.4 mm, 1.2 mm, with a Total Organic Content (TOC) of 11.20 %. Run 2 for sample 4 with particle size 1.2 mm experienced an increase in temperature of 2°C after 500 s and is observed as the pressure-time curve inclines.

Table 5: Table of sample 2 indicating variation in shale particle size, grain density, porosity, permeability, and error analysis.

Repeats	2.0 mm (mesh size 10)			1.7 mm (mesh size 12)			1.4 mm (mesh size 14)			1.2 mm (mesh size 16)		
	Grain density	Porosity	Permeability	Grain density	Porosity	Permeability	Grain density	Porosity	Permeability	Grain density	Porosity	Permeability
1	2.449	0.012	3.656	2.447	0.011	4.877	2.460	0.016	2.475	2.458	0.015	1.783
2	2.449	0.012	3.425	2.450	0.012	2.101	2.459	0.016	3.294	2.456	0.015	Bad
3	2.449	0.012	2.003	2.451	0.013	3.031	2.460	0.016	3.243	2.457	0.015	1.285
4	2.449	0.012	2.196	2.452	0.013	5.024	2.456	0.016	17.548	2.457	0.015	1.213
5	2.449	0.014	2.723	2.452	0.013	2.372	2.465	0.018	3.407	2.457	0.015	1.859
Mean	2.449	0.0123	2.801	2.450	0.012	3.481	2.460	0.017	3.105	2.457	0.015	1.535
Std	0.000	0.0011	0.730	0.002	0.001	1.384	0.003	0.001	0.426	0.001	0.000	0.333
Std of mean	0.000	0.0005	0.326	0.001	0.000	0.619	0.001	0.000	0.190	0.000	0.000	0.149
Rel error	0.00%	3.82%	11.65%	0.04%	2.83%	17.79%	0.06%	2.52%	6.13%	0.01%	0.65%	9.70%

Repeats	1.0 mm (mesh size 18)			0.85 mm (mesh size 20)			0.71 mm (mesh size 25)			0.61 mm (mesh size 30)		
	Grain density	Porosity	Permeability	Grain density	Porosity	Permeability	Grain density	Porosity	Permeability	Grain density	Porosity	Permeability
1	2.462	0.017	1.279	2.463	0.0173	1.637	2.453	0.038	Bad	2.474	0.022	1.042
2	2.458	0.015	2.547	2.465	0.0183	2.477	2.43	0.004	0.321	2.478	0.023	0.668
3	2.463	0.018	1.578	2.466	0.0187	2.097	2.465	0.018	1.175	2.480	0.024	1.433
4	2.461	0.018	1.557	2.468	0.0195	1.595	2.462	0.018	Bad	2.479	0.024	1.177
5	2.470	0.020	2.023	2.467	0.0191	1.634	2.466	0.019	3.329		0.117	6.462
Mean	2.463	0.018	1.797	2.4658	0.0186	1.888	2.455	0.019	1.609	2.478	**0.042**	1.080
Std	0.004	0.002	0.497	0.0019	0.0008	0.388	0.015	0.012	1.550	0.003	0.042	0.319
Std of mean	0.002	0.001	0.222	0.0009	0.0004	0.174	0.007	0.005	0.693	0.001	0.019	0.142
Rel error	0.08%	4.39%	12.37%	0.03%	1.96%	9.20%	0.3%	27.9%	43.1%	0.05%	44.56%	13.19%

References Cited

Boulin, P., Bretonnier, P., Gland, N., Lombard, J.-M., 2012. Contribution of the steady state method to water permeability measurement in very low permeability porous media. Oil & Gas Science and Technology–Revue d'IFP Energies nouvelles 67, 387-401.

Brace, W.F., Walsh, J., Frangos, W., 1968. Permeability of granite under high pressure. Journal of Geophysical Research 73, 2225-2236.

Bustin, A.M., Bustin, R.M., 2012. Importance of rock properties on the producibility of gas shales. International Journal of Coal Geology 103, 132-147.

Cardott, B. J., 2012. Thermal maturity of Woodford Shale gas and oil plays, Oklahoma USA. International Journal of Coal Geology, 103, 109-119.

Chalmers, G.R., Bustin, R.M., Power, I.M., 2012a. Characterization of gas shale pore systems by porosimetry, pycnometry, surface area, and field emission scanning electron microscopy/transmission electron microscopy image analyses: Examples from the Barnett, Woodford, Haynesville, Marcellus, and Doig units. American Association of Petroleum Geologists Bulletin 96, 1099-1119.

Chalmers, G.R., Ross, D.J., Bustin, R.M., 2012b. Geological controls on matrix permeability of Devonian Gas Shales in the Horn River and Liard basins, northeastern British Columbia, Canada. International Journal of Coal Geology 103, 120-131.

Chavent, G., Dupuy, M., Lemmonier, P., 1975. History matching by use of optimal theory. Society of Petroleum Engineers Journal 15, 74-86.

Clarkson, C.R., Jensen, J.L., Blasingame, T., 2011. Reservoir engineering for unconventional reservoirs: What do we have to consider?. North American Unconventional Gas Conference and Exhibition. Society of Petroleum Engineers Paper 145080-MS.

Core Laboratories, 2013. Shale Matrix Permeameter Operation Manual, pp 1-42, Tulsa, Core Laboratories.

Cui, A., Brezovski, R., 2013. Laboratory permeability measurements of unconventional reservoirs: useless or full of information, A Montney Example From The Western Canadian Sedimentary Basin. SPE 167047 presented at the Unconventional Resources Conference, Brisbane, Australia, pp. 11-13.

Cui, A., Wust, R., Nassichuk, B., Glover, K., Brezovski, R., Twemlow, C., 2013. A nearly complete characterization of permeability to hydrocarbon gas and liquid for unconventional reservoirs: a challenge to conventional thinking, Unconventional Resources Technology Conference. Society of Exploration Geophysicists, American Association of Petroleum Geologists, Society of Petroleum Engineers, pp. 1716-1732.

Cui, X., Bustin, A., Bustin, R.M., 2009. Measurements of gas permeability and diffusivity of tight reservoir rocks: different approaches and their applications. Geofluids 9, 208-223.

Dicker, A., Smits, R., 1988. A practical approach for determining permeability from laboratory pressure-pulse decay measurements, International Meeting on Petroleum Engineering. Society of Petroleum Engineers.Paper 17578-MS

Fisher, Q., Lorinczi, P., Grattoni, C., Rybalcenko, K., Crook, A.J., Allshorn, S., Burns, A.D., Shafagh, I., 2017. Laboratory characterization of the porosity and permeability of gas shales using the crushed shale method: Insights from experiments and numerical modelling. Marine and Petroleum Geology.

Gensterblum, Y., Ghanizadeh, A., Cuss, R.J., Amann-Hildenbrand, A., Krooss, B.M., Clarkson, C.R., Harrington, J.F., Zoback, M.D., 2015. Gas transport and storage capacity in shale gas reservoirs–A review. Part A: Transport processes. Journal of Unconventional Oil and Gas Resources 12, 87-122.

Ghanizadeh, A., Bhowmik, S., Haeri-Ardakani, O., Sanei, H., Clarkson, C.R., 2015a. A comparison of shale permeability coefficients derived using multiple non-steady-state measurement techniques: Examples from the Duvernay Formation, Alberta (Canada). Fuel 140, 371-387.

Ghanizadeh, A., Clarkson, C., Aquino, S., Ardakani, O., Sanei, H., 2015b. Petrophysical and geomechanical characteristics of Canadian tight oil and liquid-rich gas reservoirs: I. Pore network and permeability characterization. Fuel 153, 664-681.

Guidry, K., Luffel, D., Curtis, J., 1996. Development of laboratory and petrophysical techniques for evaluating shale reservoirs: Final Technical Report, October 1986–September 1993. Gas Shale Project Area, ResTech, Inc., Houston, TX, GRI-95/0496. 306 pp.

Handwerger, D.A., Keller, J., Vaughn, K., 2011. Improved petrophysical core measurements on tight shale reservoirs using retort and crushed samples. SPE Annual Technical Conference and Exhibition. Society of Petroleum Engineers. Paper, SPE 147456.

Hannon, M.J., 2016. Alternative approaches for transient-flow laboratory-scale permeametry. Transport in Porous Media 114, 719-746.

Heller, R., Vermylen, J., Zoback, M., 2014. Experimental investigation of matrix permeability of gas shales. American Association of Petroleum Geologists Bulletin 98, 975-995.

Javadpour, F., Fisher, D., Unsworth, M., 2007. Nanoscale gas flow in shale gas sediments. Journal of Canadian Petroleum Technology 46, p. 55-61.

Jones, S., 1997. A technique for faster pulse-decay permeability measurements in tight rocks. SPE Formation Evaluation 12, 19-26.

Kranz, R., Saltzman, J., Blacic, J., 1990. Hydraulic diffusivity measurements on laboratory rock samples using an oscillating pore pressure method. International Journal of Rock Mechanics and Mining Sciences & Geomechanics Abstracts. Elsevier, p. 345-352.

Lazar, O.R., Bohacs, K.M., Macquaker, J.H., Schieber, J., Demko, T.M., 2015a. Capturing key attributes of fine-grained sedimentary rocks in outcrops, cores, and thin sections: nomenclature and description guidelines. Journal of Sedimentary Research 85, 230-246.

Lazar, O.R., Bohacs, K.M., Schieber, J., Macquaker, J.H., Demko, T.M., 2015b. Mudstone Primer: Lithofacies Variations, Diagnostic Criteria, and Sedimentologic-stratigraphic Implications at Lamina to Bedset Scales.198 pp

Loucks, R. G., Reed., R. M., Ruppel., S. C., and Hammes, U., 2012. Spectrum of pore types and networks in mudrocks and a descriptive classification for matrix-related mudrock pores. American Association of Petroleum Geologists Bulletin 96, 1071-1098.

Luffel, D., Hopkins, C., Schettler Jr, P., 1993. Matrix permeability measurement of gas productive shales, SPE Annual Technical Conference and Exhibition. Society of Petroleum Engineers. SPE 26633, pp. 261-270.

Ning, X., Fan, J., Holditch, S., Lee, W., 1993. The measurement of matrix and fracture properties in naturally fractured cores, Low Permeability Reservoirs Symposium. Society of Petroleum Engineers. Paper, 25898-MS.

Oliver, D.S., Chen, Y., 2011. Recent progress on reservoir history matching: A review. Computational Geosciences 15, 185-221.

Pacheco-Roman, F.J., Hejazi, S.H., 2015. Estimation of solubility and diffusivity of gases in heavy oils by use of late-time pressure-decay data: An analytical/graphical approach. SPE Journal. Paper, 170957-PA.

Peng, S., Loucks, B., 2016. Permeability measurements in mudrocks using gas-expansion methods on plug and crushed-rock samples. Marine and Petroleum Geology 73, 299-310.

Profice, S., Lasseux, D., Jannot, Y., Jebara, N., Hamon, G., 2012. Permeability, porosity and Klinkenberg coefficient determination on crushed porous media. Petrophysics 53, 430-438.

Rezaee, R., 2015. Fundamentals of gas shale reservoirs. John Wiley & Sons.

Sakhaee-Pour, A., Bryant, S., 2012. Gas permeability of shale. SPE Reservoir Evaluation & Engineering 15, 401-409.

Sander, R., Pan, Z., Connell, L.D., 2017. Laboratory measurement of low permeability unconventional gas reservoir rocks: A review of experimental methods. Journal of Natural Gas Science and Engineering 37, 248-279.

Soeder, D. J., 1988. Porosity and permeability of eastern Devonian gas shale. SPE Formation Evaluation, March 1988, p. 116-124.

Sondergeld, C., Newsham, K., Comisky, J., Rice, M., Rai, C., 2010. Petrophysical considerations in evaluating and producing shale gas resources. SPE Unconventional Gas Conference, Pittsburgh, Pennsylvania, USA, 23–25 February, Paper SPE 131768.

Suarez-Rivera, R., Fjaer, E., 2012. How important is the poroelastic effect to completion design on tight shales?, 46th US Rock Mechanics/Geomechanics Symposium. American Rock Mechanics Association. Paper, ARMA 12-657.

Tinni, A., Sondergeld, C., Rai, C., 2014. Particle size effect on porosity and specific surface area measurements of shales, International symposium of the society of core analysts, Avignon, France, September 8–11, 2014.

Tinni, A., Fathi, E., Agarwal, R., Sondergeld, C.H., Akkutlu, I.Y., Rai, C.S., 2012. Shale permeability measurements on plugs and crushed samples, SPE Canadian Unconventional Resources Conference. Society of Petroleum Engineers.Paper, SPE 162235.

CHAPTER III

THE INFLUENCE OF MOISTURE ON THE PERMEABILITY OF CRUSHED SHALE SAMPLES

Mercy Achang[1,*], Jack C. Pashin[1], Eliot A. Atekwana[2]

Accepted with revision: Petroleum Science by Springer: Manuscript ID PETROSCI-2018-0040

[1]Boone Pickens School of Geology, Oklahoma State University, Stillwater, OK 74078, USA

[2]Department of Geological Sciences, University of Delaware, Newark, DE 19716, USA

Abstract

Shale cuttings and cores recovered from the subsurface and stored for hours to decades tend to dry out and lose moisture and hydrocarbons, leading to an increase in the effective matrix permeability. Moisture loss in shale sample is a fundamental sample preservation problem which can be solved by applying a standard moisture equilibration procedure to restore lost moisture. The aim was to investigate the relationship between permeability and variable moisture as well as-received, as-received moisture equilibrated and saturated moisture equilibrated samples. Samples were crushed and moisture equilibrated at 97% relative humidity. Results show that moisture equilibration in the samples was achieved after 72 hours. The permeability of the saturated moisture equilibrated and as-received moisture equilibrated sample decreased exponentially with increase in moisture content. The high correlation coefficient between permeability and particle size (r = 0.96

and 0.97) for moisture equilibrated samples compared to 0.76 for as-received samples suggest that moisture equilibration improves permeability measurements in crushed shale samples. Furthermore, permeability measurements are repeatable for moisture equilibrated samples compared to samples that were not equilibrated (as-received). We conclude that moisture content affects permeability and moisture equilibration normalizes and improves the repeatability of permeability measurements in crushed shale.

Keywords: Crushed shale; Matrix permeability, Moisture equilibration.

1.0. Introduction

Shale is a fissile mudrock composed of clay minerals, carbonate, silica and organic matter (Ingram et al. 1953; Loucks et al. 2012). When shale cuttings and cores are recovered from the subsurface and stored, they tend to dry out, and measurable changes in moisture content may occur in a matter of hours and continue for decades (Clarkson et al. 2011). The loss of moisture and hydrocarbons increases the effective permeability of stored samples and induces capillary artifacts that affect permeability measurements (Chenevert et al. 1997). For example, Clarkson et al. (2011) determined that fluid saturation of crushed samples can decrease from 40% to 2% in less than 12 hours at 20°C. Clarkson et al. (2011) showed that the rate of dehydration in shale is faster in crushed samples and cuttings than in whole cores and suggested the need to use preserved samples that have not lost moisture (e.g., preserved in polythene bags or dipped in wax) to determine petrophysical properties of stored samples. Most laboratories store cores in polythene bags to minimize dehydration. However, the cores and cuttings still dehydrate over time since the temperature and sample stress conditions during storage differ from those in the subsurface.

Moisture conditioning is a common procedure for the proximate analysis of coal (ASTM, D1412-07), which is prone to moisture loss following sampling, especially at lignite and subbituminous rank. Moisture equilibration or conditioning is the process by which hygroscopic materials reach equilibrium with the ambient relative humidity of the air by absorbing or desorbing moisture until the material neither loses nor gains moisture from the environment. For example, coal and shale naturally contain water and are susceptible to moisture loss. Moisture equilibration can be performed rapidly on crushed shale samples, but is difficult if not impossible for core plugs or even cuttings, where conditioning would require equilibration times on the order of months to years. Even then, the rock may still not reach equilibrium moisture at ambient temperature and pressure. According to the ASTM (D1412-07) standard method for coal moisture equilibration, samples are to be saturated (wet) before equilibration. However, for coal samples that deteriorate when treated with water, it is recommended that they are equilibrated directly without wetting provided the samples were collected and prepared with minimal loss of moisture (ASTM, D1412-07). Chenevert et al. (1997) have shown that moisture in shale should be preserved at native or bed moisture values to accurately measure physical properties (e.g., saturation, porosity, permeability, and bulk volume). However, no investigations have been performed to systematically determine the relationship between moisture content and matrix permeability in shale. Moisture loss in shale is a sample preservation problem that calls for a standard procedure to restore moisture in cores and cuttings before permeability measurements are made. If a shale sample contains expandable clay, the inherent moisture content will influence clay volume, pore volume, and permeability. Expandable clays when moisturized increase in volume and will reduce pore volume and the size of pore throats, thus decreasing porosity and permeability (Morris et al. 1982). To determine the bulk and quantitative mineralogical composition of shale, X-ray diffraction (XRD) was used (Butt 2012, Środoń et al. 2001, Ronald 1967).

One way to investigate the effect of moisture in preserved shale samples is to measure the permeability of the samples as-received and at different moisture content. Moisture content can be varied by oven drying a water-saturated sample for different time periods. The effect of moisture equilibration on permeability can be established by comparing the permeability of as-received samples and moisture equilibrated samples. The objective of this study was to perform controlled experiments to evaluate the relationship between moisture content and matrix permeability in as-received shale samples and moisture equilibrated shale across a range of different crushed particle sizes. To accomplish this aim, we used the standard methods for moisture equilibration of coal (ASTM D1412-07) and measured permeability using the pressure-decay permeability method applied by Achang et al. (2017).

2.0. Materials and methods

2.1. Workflow for sample analyses

The core that was used for this study is from the Danker #1-28 well (API number 350812381700003), which was recovered from the Woodford Shale (Devonian) in Lincoln County, Oklahoma, USA, and was donated to the Boone Pickens School of Geology by Sundown Energy. A description and graphic log of the core is available in Achang et al. (2017). Quantitative XRD analysis indicates quartz and orthoclase (potassium feldspar) range from 44%-72%, clay 10%-22%, calcite1%-3%, dolomite 7%-24%, and pyrite and marcasite, 3% - 37% in the 14 ft (4.4 m)). Also, the shale contains chlorite, illite, and kaolinite which are non-expandable, including minimal quantities of expandable clay and is thus minimally reactive with water. Samples from the core were taken from depths of 4907-4909 ft (1495.7-1496.3 m) and 4909-4911 ft (1496.3-1496.9 m) and crushed with a hammer and metal slab and sieved to particles sizes of 2.00, 1.70, 1.40, 1.20, 1.00, 0.85 mm, 0.71, and 0.60 mm. The as-received samples used in this research are the same as those used in Achang et al. (2017). The workflow for the procedure used in this study is shown in (Fig II - 1). A Core Laboratories Shale Matrix Permeameter (SMP 200) was used for measurement of permeability by the pressure decay method. The pressure decay curves were analyzed for permeability using the methods described by Cui et al. (2009) and Achang et al. (2017).

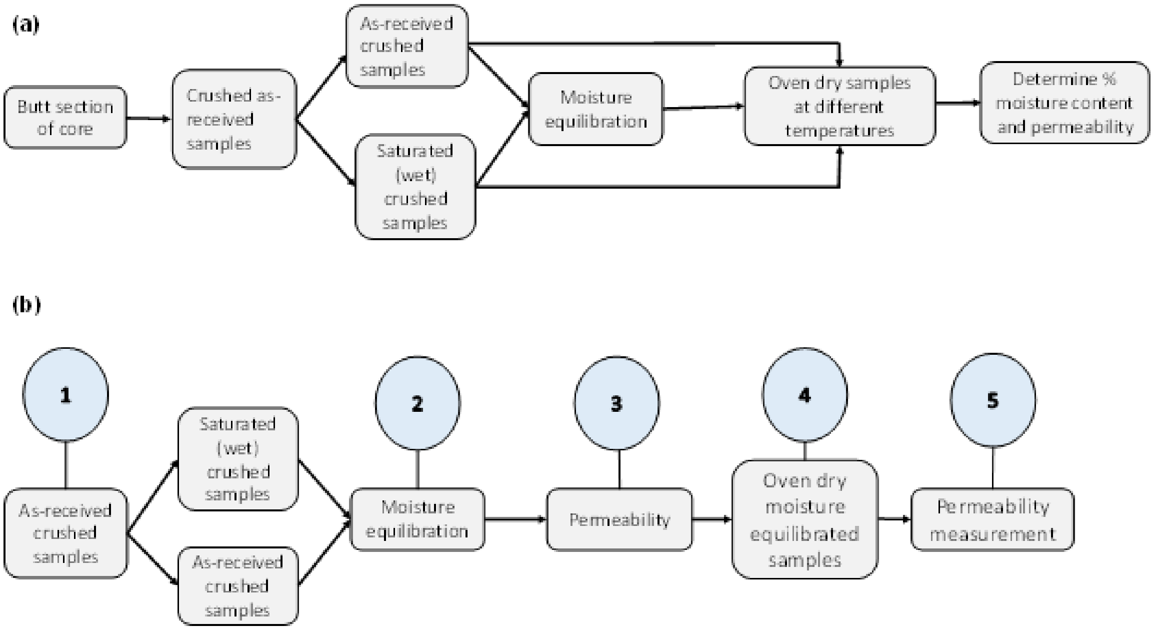

Fig III - 1. Schematic diagram of the procedure for (a) permeability determination at different moisture contents and (b) moisture equilibration and permeability determination. Numbers 1-5 indicate the major steps in the workflow.

2.2. Moisture equilibration of as-received samples

The moisture equilibration process is detailed in ASTM (2007) and begins with saturating crushed samples with water as shown (Fig III - 1 a & b) step 1 & 2. Five duplicate samples weighing 20 g with a particle size of 1.4 mm were placed in a conical flask and 100 ml of deionized water (18.2 MΩ cm) was added to wet the samples. A metal spatula was used to thoroughly stir and mix the sample. The water-sample mixture in the conical flask was placed in a desiccator for 3 h at a pressure 1.2 MPa (170 psig) indicated on the pressure gauge and a temperature of 23°C. Next, the desiccator was opened, the mixture was poured into a Büchner-type funnel, and the water was drained. A Mettler Toledo balance was used to determine the mass of a 90 mm diameter Pyrex glass petri dish. A portion of wet samples were added to the petri dish, and the mass of the saturated (wet) sample and the petri dish were recorded. The mass of the sample was estimated to be 15 g by subtracting the mass of the petri dish from the combined mass of sample and petri dish. The 15 g sample in the petri dish was placed in a vacuum desiccator containing saturated potassium sulfate (to maintain relative humidity at 97 %) sitting in a water bath maintained at 30°C and 30 mm Hg (0.58 psig or 4 kPa) for moisture equilibration. All five samples were placed in the desiccator for moisture equilibration. A sample was withdrawn from the desiccator on a daily basis, the mass measured, then dried in an oven at 105°C until the sample reaches constant mass. It generally took 1 h 30 min for constant mass to be attained; the duration of 1h 30 min was established by drying the sample at 30 min intervals and determining when the mass of the sample became invariant. After drying, the petri dish containing the sample was removed from the oven, cooled for 30 min in a desiccator and weighed. The reading was recorded and the percent equilibrium moisture was calculated using the following equation:

$$\text{Equilibrium moisture (\%)} = \left(\frac{B-C}{B-A}\right) X\,100 \qquad (1)$$

where A = weight of petri dish, B = weight of petri dish and wet shale and C = weight of petri dish and dried shale in grams. The moisture equilibration procedure described above was used for all the samples saturated with water before equilibration (saturated moisture equilibrated) and the wetting step was skipped for samples moisture equilibrated without wetting (as-received moisture equilibrated).

2.2.1. Length of Moisture Equilibration

To determine how long as-received samples and wet saturated samples should be moisture equilibrated, 3 sets of 5 samples of 15 g each and 1.4 mm particles were used. 5 samples were saturated with water for 3 h (saturated moisture equilibrated) and another 5 samples for 24 h (saturated moisture equilibrate), respectively. The remaining 5 samples were kept in the as-received (stored) state. All the samples were moisture equilibrated as described above by placing them in a desiccator containing saturated potassium sulfate at a pressure of 30 mmHg (0.58 psig or 4 kPa). The desiccator was then placed in a water bath regulated at 30°C. One sample was withdrawn after 24 h, 48 h, 72 h, 96 h, and 120 h, weighed and oven-dried to a constant weight. The weights were used to determine the moisture equilibration behavior for the water-saturated samples and for the as-received (unsaturated) moisture equilibrated samples.

2.3. Variation in moisture content and permeability

To estimate the initial moisture content of the sample, 15 g of crushed shale (particle size=1.4 mm) from a depth of 4909-4911 ft (1636-1637 m) was oven dried at 105°C for 1h 30 min then cooled in a desiccator, and the final mass measured. The difference in the weights was equivalent to the mass of the initial moisture content which was converted into percent (%) pore volume. To determine the relationship between moisture content and permeability, the moisture content in the sample was varied by oven drying for 1.4 h at 20 minutes intervals. Fig III - 1. (a) is a flowchart showing the procedure followed for moisture content-permeability experiments

A mass of 80 g (particle size=1.4 mm) of crushed shale was vacuumed saturated with DI water at 230C for 3 h. The sample was placed in an oven at an initial temperature of 40°C for 20 min then removed and cooled in a desiccator for 0.5 h and the permeability measured. The moisture content of the sample was estimated from the weight differences. The temperature of the oven was increased by 20°C and the sample was placed again in the oven for 20 minutes, removed and cooled and moisture content estimated and permeability measured. This drying step was repeated for 20 minutes increments to 120°C. Also, the as-received sample was moisture equilibrated and the moisture content and permeability measured as described above.

2.4. Permeability measurements of as-received and moisture equilibrated samples

The pressure decay curves of 75-80 g of each particle size (0.6 mm, 0.7 mm, 0.85 mm, 1.0 mm, 1.2 mm, 1.4 mm, 1.7 mm and 2.0 mm) of the as-received samples, as-received moisture equilibrated samples and saturated moisture equilibrated samples (Fig III - 1a, steps, 1, 2 and 3) were measured with the Shale Matrix Permeameter (SMP 200). The pressure decay curves for the as-received, as-received moisture equilibrated and saturated moisture equilibrated samples were assessed for the matrix permeability as described in Cui et al. 2009 and Achang et al. (2017). After the permeability of the moisture equilibrated samples were measured, the samples were oven dried (Fig III - 1a step 4 & 5) and the permeability again measured and compared with the as-receives values.

3.0. Results

3.1 Time required for moisture equilibration of as-received moisture equilibrated and saturated moisture equilibrated samples

The time required for moisture equilibration of 15 g samples is 72 h (Fig III - 2). The region where the best fit line for the data appears to be more stable in Fig III - 2 a & b, is the region where mass becomes relatively constant or negligible, indicating equilibrium at a relative humidity of 97%. Samples actually begin to attained equilibrium after 48 h but because 48 h is at the boundary between steep moisture change and little moisture change, a value that was used for the entire study is 72 h for 15 g masses and 96 h for 75 - 80 g mass of crushed shale samples.

The initial moisture content of the as-received sample from the depth 4909 ft (1496.26 m) was estimated to be 0.57 %. The moisture content in the as-received sample increased from 0.57% to 1.50% within 24 h of moisture equilibration and stayed relatively constant at 1.5 % moisture content. The sample reached equilibrium by 48 h and the moisture content did not change significantly for the remainder of the 120 h equilibration period. The moisture content for the saturated moisture equilibrated samples increase to 8-10% within 24 h (Fig III - 2a). The moisture content of the saturated moisture equilibrated samples, which were saturated for 3 h and 24 h, reached equilibrium by 48 h, and then remained effectively constant at approximately 2.9%, and 1.9% (Fig III - 2b), respectively. Overall moisture content gained by as-received (unsaturated) moisture equilibrated samples is 1.5 % compared to 2.9 % and 1.9 % for saturated moisture equilibrated samples (Fig III - 2b).

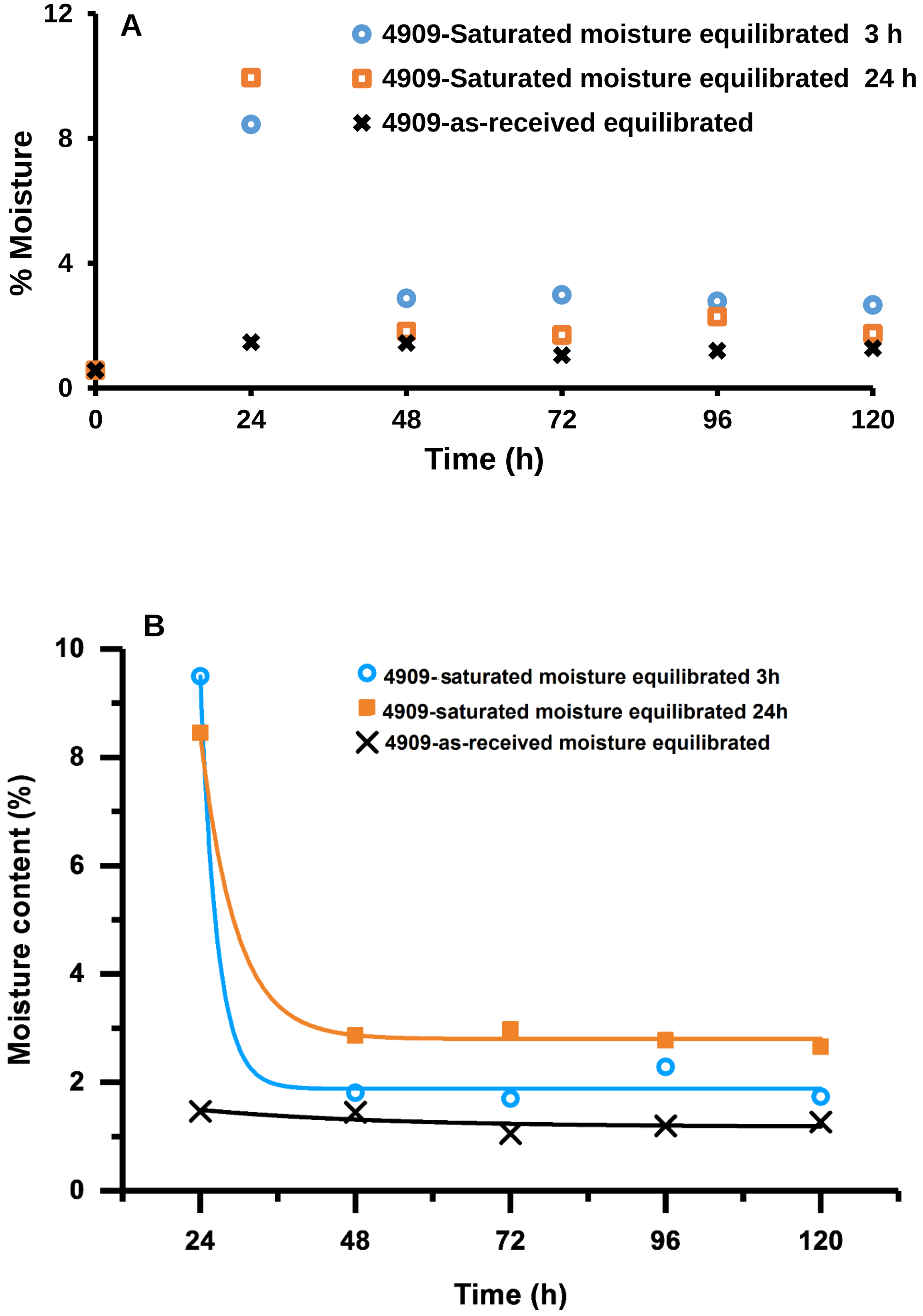

Fig III - 2. (a) time versus moisture change and (b) time versus moisture content gained for saturated equilibrated samples for 3 h and 24 h and as-received equilibrated samples of mass 15g.

The saturated equilibrium moisture content of the 75 g sample was estimated to be 2.2% even though it was not plotted. Following moisture equilibration, samples are exposed to the atmosphere and may lose some moisture prior to permeability measurement. However, some moisture is lost during the transfer of samples from the desiccator to the permeameter, and based on a Mettler Toledo balance results, an average of 0.068 g is lost in 3 h from samples of particle size 1.4 mm at a temperature of 23 0C.

3.2. Variation in equilibrium moisture content versus permeability

A plot of moisture content expressed as percent pore volume versus permeability (Fig III - 3a) shows a decreasing exponential relationship. Regression analysis indicates a negative correlation coefficient of -0.97 for saturated moisture equilibrated samples and -0.86 for as-received moisture equilibrated samples (Fig III - 3b). When the moisture content in the pore volume (PV) is approximately 97%, permeability is only ~0.01 nD for saturated moisture equilibrated samples and 0.22 nD for as-received moisture equilibrated samples. Permeability increases with decreasing moisture from 0.01 nD to 0.3 nD at a moisture content of 70% and increases exponentially to more than 3.0 nD as equilibrium moisture content falls below 10% of pore volume (Fig III - *3*a). Also, the permeability of the as-received moisture equilibrated samples is greater than that of the saturated moisture equilibrated samples and the best-fit regression lines for both samples follow exponential functions (Fig III - 3.a & b).

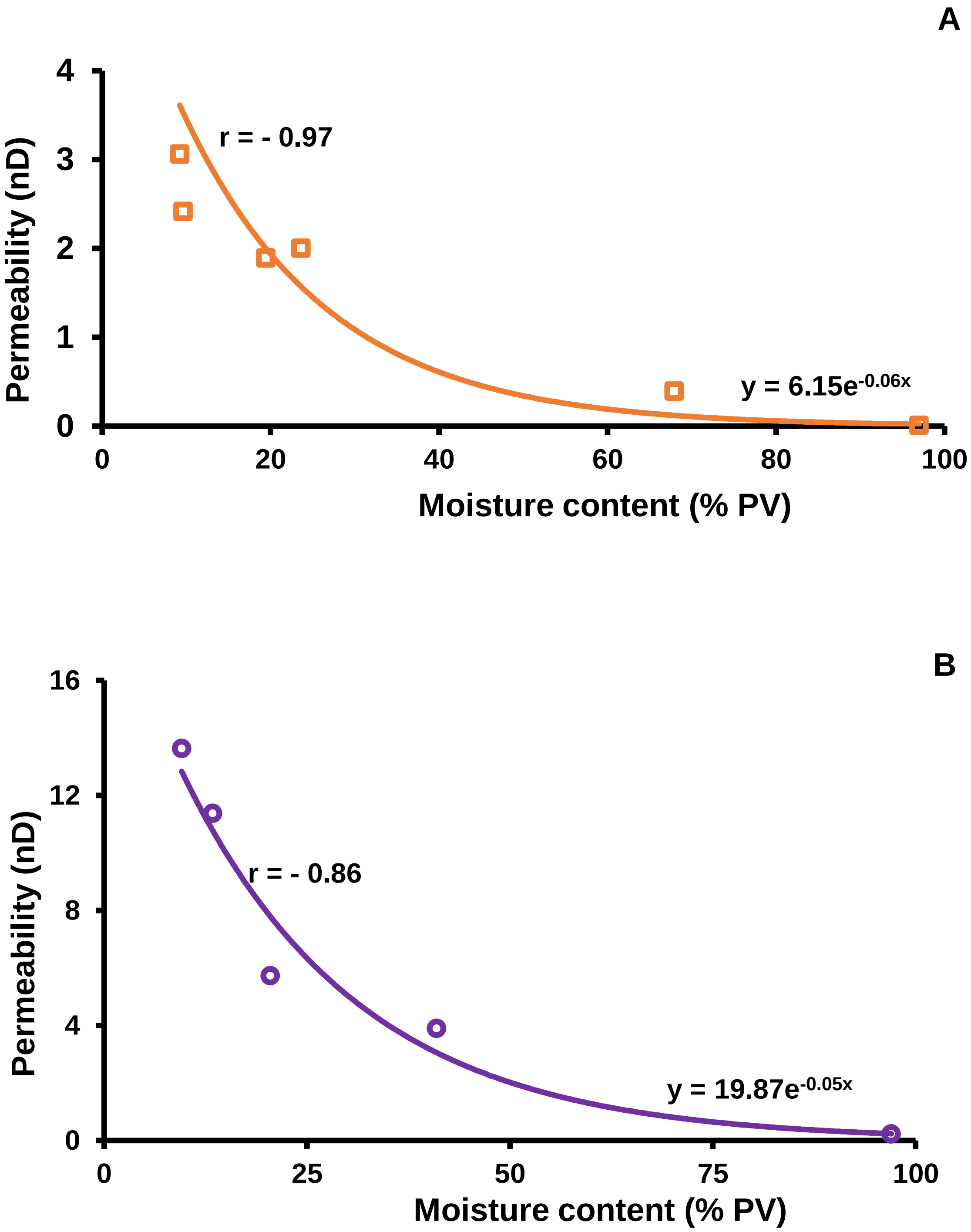

Fig III - 3. Relationship between moisture content (% pore volume) and permeability in a (a) saturated (b) as-received moisture equilibrated shale sample. An exponential relationship is observed between moisture content and permeability. The sample particle size is 1.4 mm and is from a depth of 4909 ft (1496.3 m).

3.3. Permeability measurements of as-received and saturated moisture equilibrated samples

For as-received, saturated moisture equilibrated and as-received moisture equilibrated samples, permeability correlates positively with particle size (Fig III - 4). The as-received samples have higher permeability than the saturated moisture equilibrated and as-received moisture equilibrated samples. For samples from a depth of 4907 ft (1495.65 m) permeability ranges from 4.47 nD to 171.9 nD for as-received samples (Achang et al. 2017), 0.5 nD to 6.8 nD for saturated moisture equilibrated samples. For samples from the depth 4909ft (1496.26 m), as-received permeability ranges from 1.65 nD to 13.05 nD, as-received moisture equilibrated sample permeabilities range from 0.15 nD to 5.3 nD and the permeability of saturated moisture equilibrated samples from 0.16 nD to 6.8 nD. Correlation coefficients of 0.96 and 0.97 were calculated for the saturated moisture equilibrated at depths of 4907 ft and 4909 ft respectively compared to 0.95 and 0.76 for the as-received samples of same depth in turn. The permeability of as-received samples from 4907 ft is greater than that of the saturated moisture equilibrated samples from that depth. The correlation coefficient of the as-received sample (0.76) is smaller than the as-received moisture equilibrated samples (0.96) and saturated moisture equilibrated samples (0.97) samples from 4909 f (Fig III - 4b).

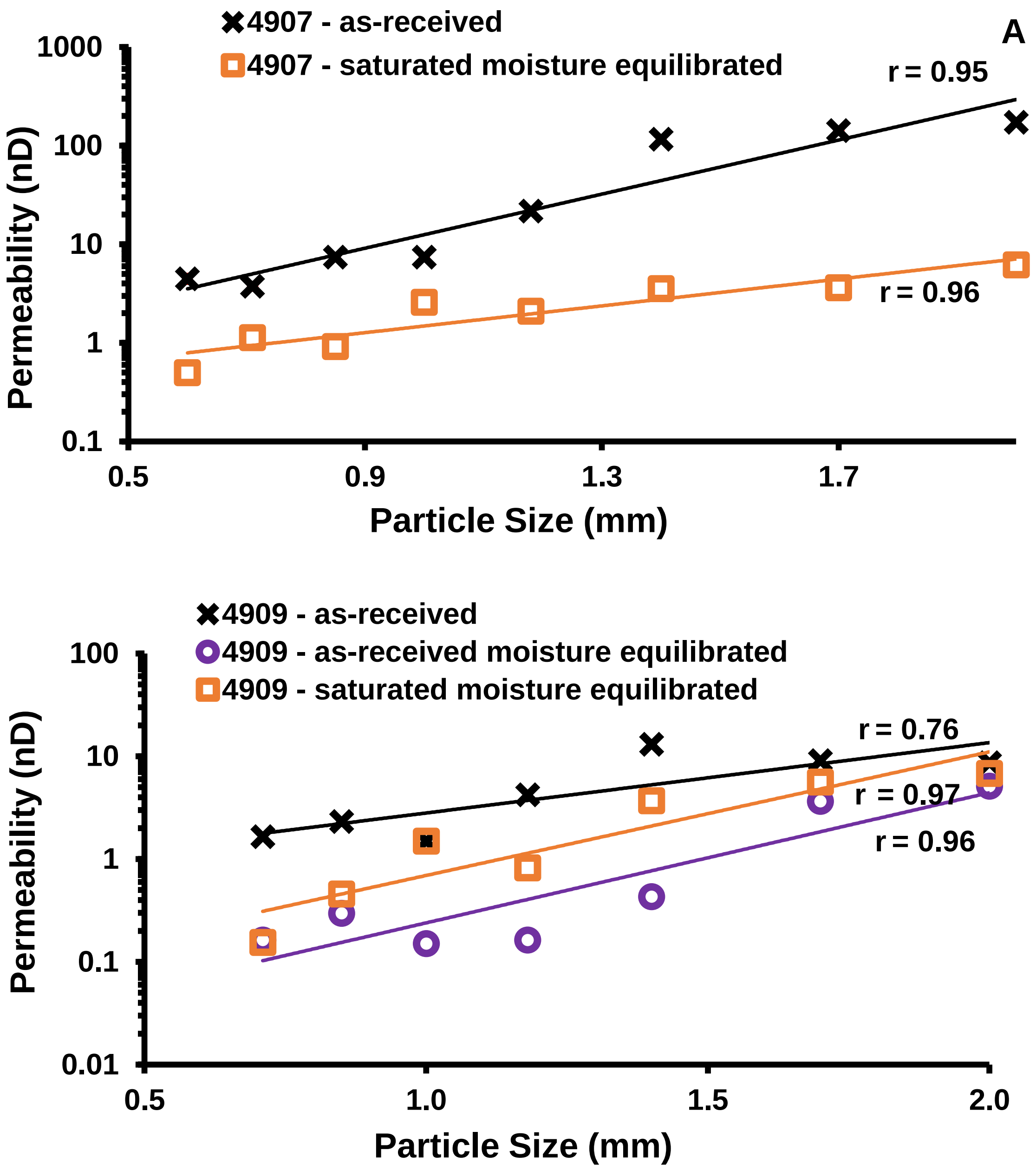

Fig III - 4. Particle size versus permeability for as-received, saturated moisture equilibrated and as-received moisture equilibrated samples from the Danker #1-28 core (a) 4907 ft (1495.65 m) and (b) 4909 ft (1496.26).

Multiple runs to determine the permeability of a sample after moisture equilibration results in greater repeatability than multiple runs of the as-received samples (Table 6 & 2). The relative error of the permeability of as-received samples from 4907 ft ranged from 3.0 to 23.0% and for saturated moisture equilibrated samples from that depth ranged from 11 to 38% across the different particle sizes. For the samples taken from 4909 ft, the relative error for as-received samples saturated moisture equilibrated and as-received moisture equilibrated samples range from 5.7 to 30 %, 3.4 to 24%, and 7.4 to 18 %, respectively. Nevertheless, the results for particle size 0.71 mm and 1.18 mm have an exceptionally large error of 39% and 24 %, respectively

. Overall, the scatter plot of the relative error is shown in Fig III - 5.

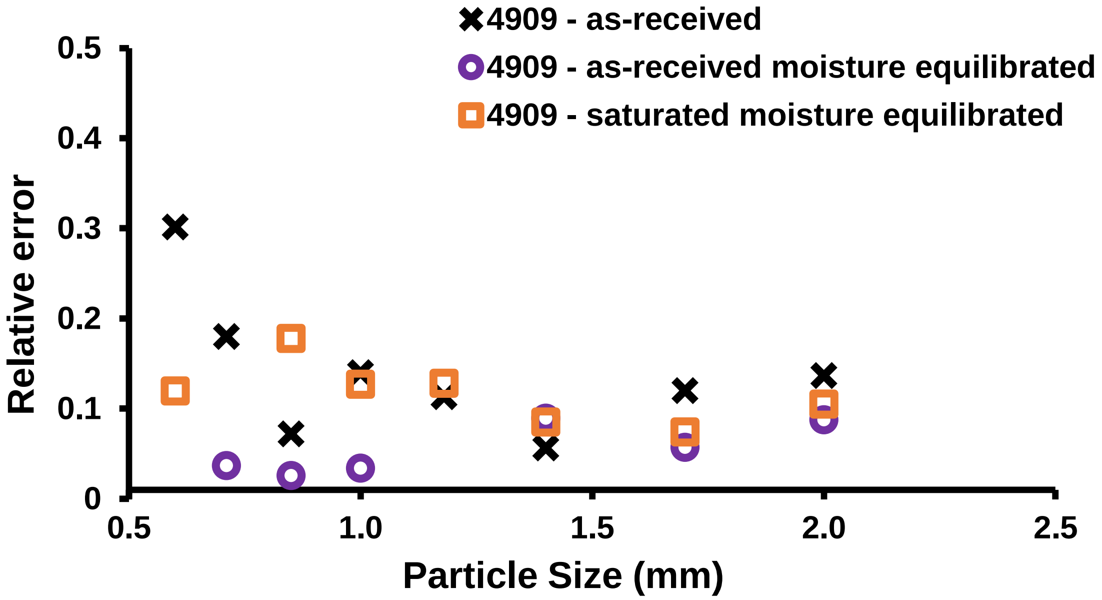

Fig III - 5. Relative error in permeability of as-received, as-received moisture equilibrated and saturated moisture equilibrated samples. The error is relatively stable for particles sizes greater than1.4 mm.

Table 6: Particle size and permeability (exponential decay segment) measurements for as-received samples and saturated moisture equilibrated samples from the Danker #1-28 core at 4907 ft (1495.65 m). For individual particle sizes, of saturated moisture equilibrated samples the permeability is highly repeatable compared to As-received samples.

Sample	Permeability (nD)							
4907	2.0 mm		1.7 mm		1.4 mm		1.2 mm	
Repeats	As-received	Saturated moisture equilibrated	As-received	Saturated moisture equilibrated	As-received	Saturated moisture equilibrated	As-received	Saturated moisture equilibrated
1	248.98	6.11	138.43	4.08	11.93	4.96	11.08	2.33
2	133.37	6.07	192.16	3.38	10.36	3.19	37.09	2.00
3	133.37	5.82	94.92	3.04	7.23	3.50	16.59	1.98
4	/[4]	6.74	/	3.42	6.70	2.79	/	1.98
5	/	6.16	/	4.13	/	3.27	/	2.18
Mean	171.91	6.18	141.84	3.61	9.06	3.54	21.59	2.09
Std	66.75	0.39	39.77	0.38	2.17	0.747	11.19	0.14
Mean of Std	38.54	0.18	22.96	0.17	1.09	0.334	6.46	0.06
Rel error	22.42%	2.83%	16.19%	4.65%	11.99 %	9.43%	29.94%	3.02%

Sample	Permeability							
4907	1.0 mm		0.85 mm		0.71 mm		0.60 mm	
Repeats	As-received	Saturated moisture equilibrated	As-received	Saturated moisture equilibrated	As-received	Saturated moisture equilibrated	As-received	Saturated moisture equilibrated
1	7.98	2.88	3.23	0.56	2.59	1.14	2.34	0.55
2	7.58	2.48	13.21	1.30	4.90	1.47	6.60	0.56
3	6.62	2.40	4.18	0.89	/	2.01	/	0.38
4		3.27	/	/	/	0.47	/	/
5	/	/	/	/	/	0.57	/	/
Mean	7.81	2.58	6.87	0.92	3.75	1.13	4.47	0.50
Std[5]	0.57	0.35	4.50	0.31	1.15	0.57	2.13	0.08
Mean of Std	0.28	0.17	2.60	0.18	0.82	0.26	1.51	0.05
Rel[6] error	5.64%	6.75%	37.78%	19.23%	21.77%	22.62%	33.72%	9.55 %

---

[4] Means no data available

[5]Std means standard deviation

[6] Rel error means relative error.

Table 7: Particle size and permeability measurements for as-received, saturated moisture equilibrated, and as-received moisture equilibrated samples from the Danker #1-28 core at 4909 ft (1496.63 m). For a given particle size, the permeability is highly repeatable for moisture equilibrated samples compares as-received samples.

Sample	Permeability (nD)					
4909	2.0 mm			1.7 mm		
Repeats	As-received	As-received moisture equilibrated	Saturated moisture equilibrated	As-received	As-received moisture equilibrated	Saturated moisture equilibrated
1	7.15	4.47	7.46	11.93	3.59	5.42
2	11.00	6.89	8.48	10.36	3.61	4.64
3	7.86	4.96	5.41	7.23	4.28	5.53
4		4.78	5.85	6.70	3.12	6.95
5		4.55	/	/		/
Mean	8.67	5.13	6.80	9.06	3.65	5.64
Std	2.048	1.004	1.43	2.17	0.414	0.83
Mean of Std	1.182	0.449	0.71	1.09	0.207	0.42
Rel error	13.64%	8.75%	10.48 %	11.99 %	5.68%	7.40 %

Sample	Permeability (nD)					
4909	1.4 mm			1.2 mm		
Repeats	As-received	As-received moisture equilibrated	Saturated moisture equilibrated	As-received	As-received moisture equilibrated	Saturated moisture equilibrated
1	12.01	0.59	4.71	4.88	0.20	0.93
2	14.09	0.37	4.40	3.53	0.04	1.14
3	/	0.35	3.26	/	0.17	0.85
4	/	0.38	3.07	/	0.25	0.78
5	/	0.46	3.07	/		0.42
Mean	13.05	0.43	3.70	4.21	0.16	0.82
Std	1.04	0.086	0.71	0.67	0.080	0.24
Mean of Std	0.74	0.038	0.32	0.48	0.040	0.11
Rel error	5.64 %	8.93%	8.52 %	11.32 %	24.34%	12.81 %

Sample	Permeability (nD)					
4909	1.0 mm			0.85 mm		
Repeats	As-received	As-received moisture equilibrated	Saturated moisture equilibrated	As-received	As-received moisture equilibrated	Saturated Moisture equilibrated
1	1.08	0.14	1.08	2.56	0.29	0.24
2	2.15	0.15	2.15	2.09	0.29	0.79
3	1.64	0.17	1.64		0.32	0.46
4	0.98	0.15	0.98		0.30	0.41
5	1.64		1.64			0.39
Mean	1.50	0.15	1.50	2.33	0.30	0.46
Std	0.47	0.010	0.42	0.24	0.02	0.18
Mean of Std	0.21	0.005	0.19	0.17	0.01	0.08
Rel error	13.98 %	3.37%	12.68 %	7.19 %	2.57%	17.76 %

Sample 4909	Permeability (nD)					
	0.71 mm			0.60 mm		
Repeats	As-received	As-received moisture equilibrated	Saturated moisture equilibrated	As-received	As-received moisture equilibrated	Saturated moisture equilibrated
1	2.16	0.15	0.01	0.28	0.09	/
2	1.09	0.16	0.05	1.00	0.05	/
3	2.21	0.19	0.37	1.41	0.07	/
4	/	0.16	0.08	/	0.06	/
5	/	0.16	0.26	/	0.09	/
Mean	1.65	0.16	0.15	0.89	0.07	/
Std	0.51	0.01	0.14	0.47	0.02	/
Mean of Std	0.30	0.01	0.06	0.27	0.01	/
Rel error	17.98 %	3.65%	39.40 %	30.13 %	11.95 %	/

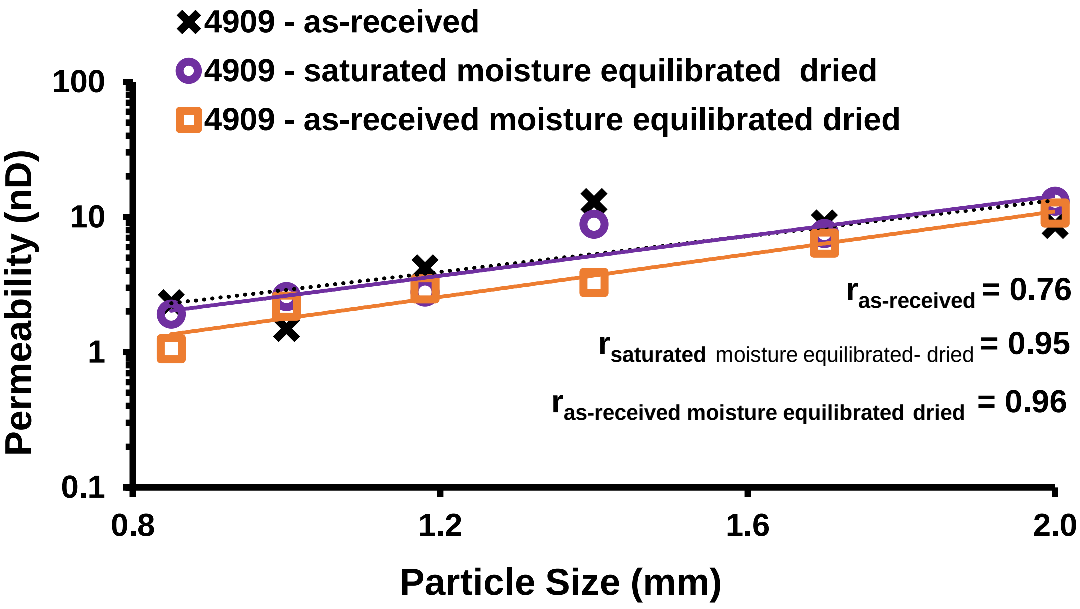

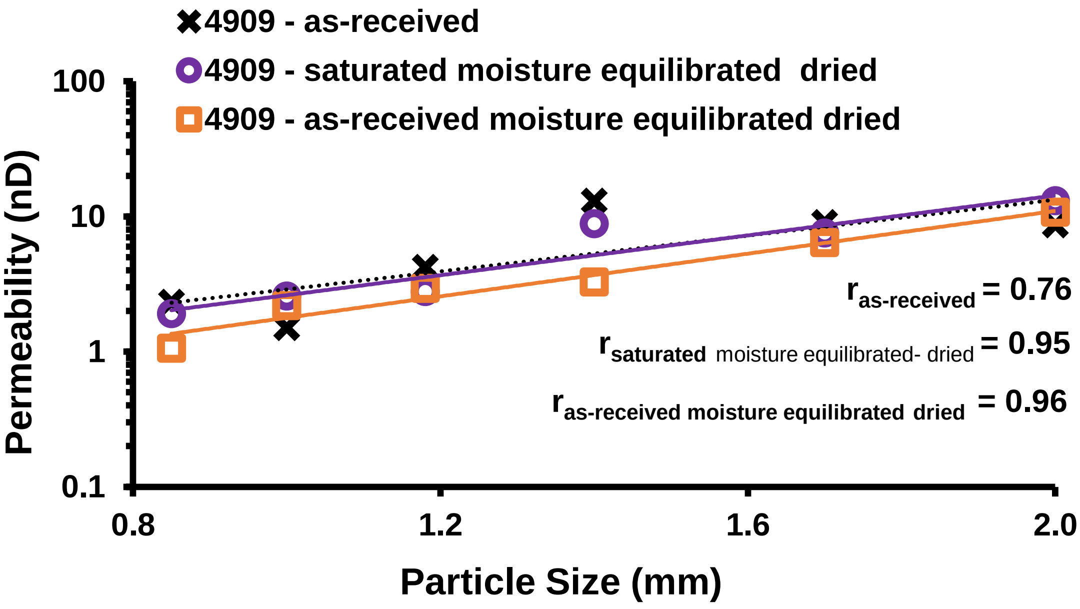

Fig III - 6 is a plot of particle size versus permeability of as-received, as-received moisture equilibrated and saturated moisture equilibrated samples that were subsequently oven dried. The results were plotted and compared with the permeability of the as-received samples. The correlation coefficients derived from the regression analysis of the oven dried samples are 0.95 (saturated moisture equilibrated) and 0.96 (as-received moisture equilibrated) in comparison to 0.76 for the as-received sample.

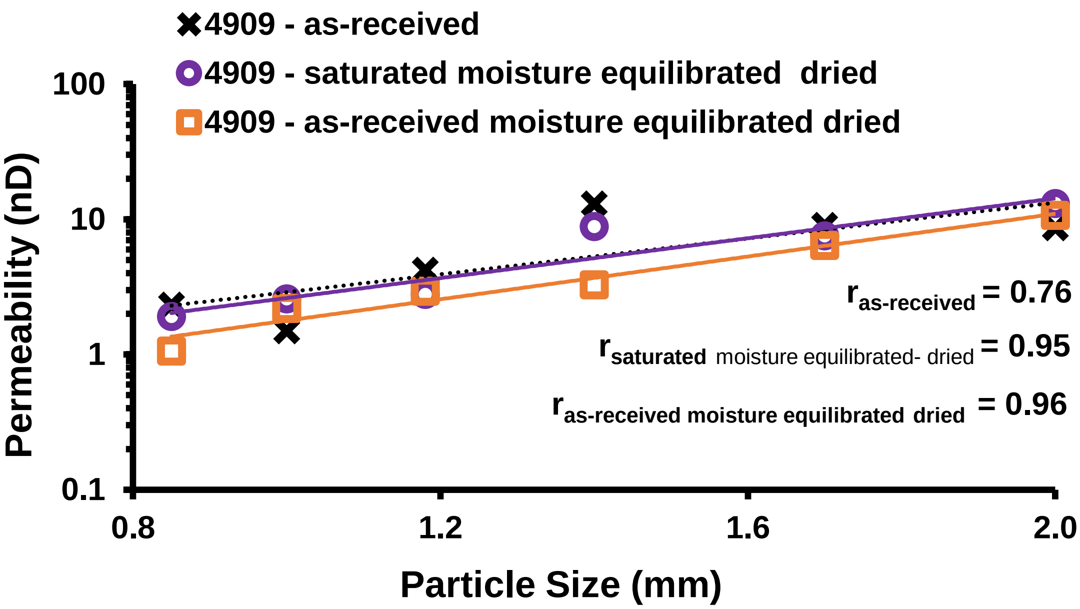

Fig III - 6. Particle size vs. permeability of samples that were oven dried for 1h 30min after moisture equilibration plotted with results derived from as-received samples.

4.0. Discussion

4.1. Variation in equilibrium moisture content expressed as percent pore volume and permeability

The dominant clay minerals in the Danker #1-28 core include chlorite, kaolinite, and illite which are stable and thus, wetting and drying samples had minimal impact on rock fabric. Moisture content is inversely and exponentially proportional to permeability (Fig III - 3). Thus, as the water-filled portion of the pore volume decreases, the permeability to gas increases exponentially in both saturated and as-received moisture equilibrated samples (Fig III - 3 a & b). The permeability for saturated moisture equilibrated samples ranges from 0.1 nD in samples where moisture occupies approximately 97 % of the pore volume and 3.06 nD in samples where moisture occupies about

10% of the pore volume. Additional moisture, including some clay bound water, would be removed if the samples were heated to 140°C and all structural bound water would be removed if the samples were heated beyond 400°C (Handwerger et al. 2011, Sondergeld et al. 2010), potentially increasing permeability further. Therefore, the smaller the % moisture content in the pore volume, the greater the permeability and vice versa.

4.2. As-received and saturated moisture equilibrated

The results of as-received and saturated moisture equilibrated samples show that it is possible for Woodford Shale samples to be moisture equilibrated to moisture contents between 2.9 and 1.9% (Fig III - 2b), which falls within values measured in other Devonian shale formations (Chalmers et al. 2010). Saturating samples with water prior to moisture equilibration results in higher equilibrium moisture values than equilibrating from the as-received state (Fig III - 2). A period of 72 h is required to equilibrate samples of 15 g or less since 48 h is when equilibrium starts. However, for samples of 50 g or larger, it takes 96 h for moisture to equilibrate. The increase in moisture content from 0.6% to 10.0% followed by a decrease to 2.9 % and 1.9 % in saturated moisture equilibrated samples indicates a reversal of the humidity gradient between the samples and water on surfaces of the particle and the desiccator. Following wetting (saturation), the shale is effectively saturated with water and gradually releases the water to the atmosphere in the desiccator until the sample reaches equilibrium with a relative humidity of 97% in the desiccator atmosphere (Fig III - 2). In as-received (as-received) samples, the moisture moves from the atmosphere of the desiccator into the sample, and so the moisture content increases from 0.57 to 1.9% (Fig III - 2). The difference in the moisture content between saturated and as-received moisture equilibrated samples is because, it is easier to remove water from the shale samples than adding water due to capillary forces. Bigourdan et al.(1997) made similar observations when photographic films and library books (organic materials) were exposed to different levels of relative humidity and moisture.

4.3. Moisture equilibrated samples and matrix permeability

The permeability of as-received samples, saturated moisture equilibrated samples and as-received moisture equilibrated samples increases with increasing particle size. The positive correlation between permeability and particle size was first observed by Cui et al. (2009) which they explained using a dual porosity model where connected macropores and micropores are responsible for the increase in permeability with an increase in particle size. Achang et al. (2017) have made similar observations and suggested the positive correlation results mainly from the presence of macropores, particularly in larger particle sizes, and microfractures, which were observed in SEM images and in many cases appear to be a result of crushing the shale for pressure-decay permeability analysis. The high correlation coefficient between permeability and particle size (r = 0.96 and 0.97) for moisture equilibrated samples compared to 0.76 for as-received samples (Fig III - 4) suggests that moisture equilibration improves the robustness of pressure decay permeability measurements in crushed shale samples. Furthermore, permeability measurements are repeatable for moisture equilibrated samples compared to samples that were not equilibrated (Table 6 & 2). The relative errors observed for the largest particles sizes >1.0 mm are more consistent compared to those <1 mm were scattering is dominant. Thus, more complete moisture equilibration of larger particles. Clarkson et al. (2011) showed that crushed particles lose moisture faster than core plugs, and so it follows that smaller crushed particles would lose moisture faster than larger crushed particles for particles sizes <1.0 mm could result from lower effectiveness in equilibration of particle sizes <1.0 mm making them not ideal for moisture equilibration and permeability analysis. Since the permeability of the equilibrated samples is lower than that of the as-received samples. Higher correlations between particle size and permeability (Fig III - 6) indicating that oven drying effectively returns the samples studied close to an as-received state. However, higher correlations between particle size and permeability (Fig III - 6) of dried as-received moisture equilibrated and saturated moisture equilibrated samples again highlights the importance of applying some standard procedure (ASTM, D1412-07) of moisture equilibration to improve the consistency and predictability of pressure-decay permeability determinations.

An important limitation of moisture equilibration is that it probably does not restore shale to its native state, particularly in samples where hydrocarbons have devolatized. However, equilibration is suggested to reduce capillary and effective permeability artifacts related to moisture loss when determining matrix permeability. Moreover, some moisture is lost during the transfer of samples from the desiccator to the permeameter (average of 0.068 g of moisture is lost in 3 h from samples of particle size 1.4 mm) is equivalent to 0.09% of the moisture content by pore volume. The 0.09% error in moisture content is negligible.

5.0. Conclusions

Moisture content is inversely related to permeability in shale and equilibrating shales to an equilibrium moisture content results in more accurate and repeatable measurements and greater predictability of basic relationships, such as that between permeability and particle size. The particle size - permeability relationship of moisture equilibrated samples increase with increasing particle size and moisture equilibrated samples have better correlation coefficients compared to as-received samples suggesting that moisture equilibration improves pressure decay permeability measurements in crushed shale samples. Therefore, moisture equilibration is recommended as a standard way of preparing shale samples for permeability measurements.

Moisture equilibration can be performed to help restore moisture lost during sample storage and can be performed on as-received samples or water saturated samples. The Woodford Shale samples studied in this research have unexpandable clays and so quantitative results were obtained using as-received and saturated samples. The duration for moisture equilibration in the shale samples studied is 72 h for samples equal to or smaller than 15 g and 96 h for samples of 75 g to 100 g. All samples gained moisture during equilibration and saturated samples retained more moisture at equilibrium than unsaturated (as-received) samples. Even though moisture equilibration does not restore the shale sample to its original moisture content, particularly in samples where hydrocarbons have volatized, equilibrium moisturization helps normalize analyses by compensating for moisture loss post core retrieval, transport, and storage.

Acknowledgments

This study was supported in part by Grants-in-Aid Fund from the American Association of Petroleum Geologists and National Association of Black Geoscientists. We thank J. Puckette for providing access to the Danker #1–28 core. The authors thank six anonymous reviewers for comments and suggestions that helped improve the quality of this manuscript

References Cited

Achang, M., Pashin, J., Cui, X. 2017. The influence of particle size, microfractures, and pressure decay on measuring the permeability of crushed shale samples. International Journal of Coal Geology, 183,174 - 187.

Butt, A. S., 2012. Shale characterization using X-Ray diffraction. Master's Thesis, Dalhousie University, Halifax, Nova Scotia.

Carl H.S., Kent E.N., Joseph T.C., Morgan, C.R., and Chandra S. R. 2010. Petrophysical Considerations in Evaluating and Producing Shale Gas Resources. Paper presented at the SPE Unconventional Gas Conference, Pittsburgh, Pennsylvania, USA, 23–25 February (Reprint). SPE-131768

Chalmers, G. R., Bustin, M., R. 2010. PS The Effects and Distribution of Moisture in Gas Shale Reservoir Systems. AAPG search and discovery # 80113.

Chalmers, G.R., Gareth, R.L., Daniel, J.K., Ross, R., Bustin, M. 2012. Geological controls on matrix permeability of Devonian gas shales in the Horn River and Liard basins, northeastern British Columbia, Canada. International Journal of Coal Geology, 103,120-131.

Chenevert, M.E, Amanullah, M.D., 1997. A novel laboratory technique to determine the saturation status of shale. International Symposium of the Society of Core Analyses, SCA-9728.

Clarkson, C. R., Jerry, Jensen, L., Tom Blasingame. 2011. Reservoir engineering for unconventional reservoirs: what do we have to consider? Society of Petroleum Engineers, paper SPE 145080. doi.org/10.2118/145080-MS

Cui, X, AMM Bustin, Robert M Bustin. 2009. Measurements of gas permeability and diffusivity of tight reservoir rocks: different approaches and their applications. Geofluids 9 (3), 208-223.

Ebrahimi-Kahrizsangi, Reza, Majid Abdellahi, Maryam Bahmanpour. 2015. Self-ignited synthesis of nanocomposite powders induced by Spex mills; modeling and optimizing. Ceramics International, 41 (2), 3137-3151.

David Allen Handwerger, John Keller, Kelly Vaughn. Improved petrophysical core measurements on tight shale reservoirs using retort and crushed samples. Society of Petroleum Engineers, paper SPE 147456. doi: 10.2118/147456-MS

Ingram, R. L. 1953. Fissility of mudrocks. Geological Society of America Bulletin 64: 869-878.

Kittrick, J. A., E. W. Hope. 1963. A Procedure for the Particle-Size Separation of Soils for X-ray Diffraction Analysis. Soil Science 96 (5), 319-325.

Loucks, R. G., Robert. M. R., Stephen. C. Ruppel and Ursula Hammes. 2012. Spectrum of pore types and networks in mudrocks and a descriptive classification for matrix-related mudrock pores. AAPG Bulletin 96 (6), 1071-1098.

Morris, K. A., C.M. Shepperd. 1982. The role of clay minerals in influencing porosity and permeability characteristics in the Bridport Sands of Wytch Farm, Dorset. Clay Minerals 17 (1), 41-54.

Rietveld, H.M., 1969, A profile refinement method for nuclear and magnetic structures. Journal of Applied Crystallography, 2 (2): p. 65-61. doi:10.1107/S0021889869006558.

Ronald, J. 1967. Quantitative X-ray diffraction analysis using clay mineral standards extracted from the samples to be analyzed. Clay Minerals 7, 79-91.

Środoń, Jan, Victor A Drits, Douglas K Mc Carty et al. 2001. Quantitative X-ray diffraction analysis of clay-bearing rocks from random preparations. Clays and Clay Minerals 49 (6), 514-528.

ASTM D1412-07 Standard Test Method for Equilibrium Moisture of Coal at 96 to 97 Percent Relative Humidity and 30°C, ASTM International, West Conshohocken, PA, 2007, https://doi.org/10.1520/D1412-07

CHAPTER IV

COMPARISON OF PORE SIZE DISTRIBUTION ON CRUSHED AND WHOLE-ROCK SHALE SAMPLES

Mercy Achang[1,*], [1]Jack C. Pashin, [2]Parameswar Hari

[1]Boone Pickens School of Geology, Oklahoma State University, Stillwater, OK 74078, USA

[2]Department of Physics and Engineering Physics, The University of Tulsa, OK 74104, USA

Abstract

To estimate oil and natural gas resources and reserves and to develop reservoir flow models, it is essential to accurately characterize the porosity, permeability, and fluid saturation of shale. Nuclear magnetic resonance (NMR) is a useful tool for petrophysical characterization of sedimentary rocks because the NMR response of reservoir rocks is independent of conductive materials in pore fluids. Helium porosity, retort fluid saturation, low-pressure nitrogen sorption, and permeability measurements in shale are commonly performed on crushed rock, while NMR analysis requires whole-rock samples, which are challenging to analyze because nanoporosity is dominant and permeability is on the order of nanodarcies. The objective of this study was to compare pore size distribution in crushed and whole-rock shale samples to determine if crushed or whole-rock samples are best suited for NMR investigations in shale. Porosity, pore shape, and geometry also were analyzed. The methods used in this study are NMR, helium porosimetry, and low pressure nitrogen sorption analysis. Results show that the area under the T2 distribution curve in shale is greater than that in whole-rock samples. This area increases with a decrease in crushed-rock particle size, whereas this area in the whole-rock sample remains constant. The increase in the area under the T_2 distribution curve is suggested to be caused by additional pore space that forms when shale is crushed, including fractures. Both crushed and whole-rock shale samples have unimodal and bimodal T_2 distributions. Continuous bimodal distributions indicate connectivity and possibly coupling among pores. Coupling of pores in crushed shale increases with decreasing particle size and is attributed to communication through the interfaces between touching particles in crushed shale. Coupling of particles of crushed rock skews porosity estimates but may be used for the development of more accurate reservoir flow models in hydraulically fractured reservoirs as well as in the estimation of the amount of damage-related porosity resulting from crushing. Most of the pores detected by low-pressure nitrogen sorption are mesopores, which are where a large quantity of shale gas is sorbed. Pore shapes are interpreted as slitlike based on the sorption results and have been verified by pores imaged by a field emission scanning electron microscope (SEM). The pore shapes are useful for interpreting the structural integrity of the shale and suggest how readily the shale will respond to stress during hydraulic fracturing. Even though saturating whole shale samples is challenging, it is beneficial to make both crushed and whole-rock NMR measurements, because modeling and predicting production in shale relies on the ability to accurately characterize matrix and fracture porosity. NMR and He estimates of porosity correlate strongly ($r = 0.93$), indicating that NMR results correspond well to measurements made by traditional methods; however, He porosity is greater than porosity estimated by nitrogen adsorption experiments because He penetrates smaller pores than N_2.

Keywords: pore size distribution, NMR, crush shale, whole samples, coupling, helium porosimetry.

1.0. Introduction

Nuclear magnetic resonance (NMR) is an established tool for the characterization of porosity, permeability, pore size distribution, fluid saturation, and fluid type because the response is independent of conductive minerals in reservoir pore fluids (Coates et al., 1999). Porosity and permeability studies are essential for the estimation of petroleum resources and reserves. Because pore size distribution influences the transport of fluids in sedimentary rocks, it needs to be characterized for fluid flow modeling and to define reservoir flow units. NMR is a technique based on the response of an atomic nucleus (e.g., hydrogen) to an external magnetic field (Coates et al., 1999; Kenyon, 1997). The transverse and longitudinal relaxation that results from the application of the Carr-Purcell-Meiboom-Gill (CPMG) pulse sequences during an NMR experiment is used to study fluid storage capacity (porosity) and pore size distribution in rocks, and is also useful for typing reservoir fluids. NMR pore size distribution in shale is determined based on the assumptions that (1) fast diffusion limits apply (molecules bounce off pore walls and traverse the pore multiple times before relaxation, (2) gradient diffusion and bulk relaxation are negligible as they take much more time than fast diffusion, and (3) surface relaxivity is uniform on the pore walls (Brownstein and Tarr, 1979; Lonnes et al., 2003). NMR response is related to pore size in equation (1) (Coates et al., 1999; Rezaee, 2015; Saidian and Prasad, 2015).

$$\frac{1}{T_i} = \rho_i \frac{S}{V} = \rho_i \frac{C}{r}, \tag{1}$$

where i denotes either T_1 or T_2 relaxation, ρ is surface relativity, S is pore surface area, V is pore volume, r is pore radius, and C is a constant (1, 2, or 3 for planar, cylindrical and spherical pores respectively). Based on equation (1), pore size increases with increasing T_2 times.

Surface relaxivity represents the strength of longitudinal and tranverse relaxation on pore surfaces (the relaxing strength of the grain surfaces). Relaxivity depends on the properties of the solid surface (the mineralogical composition), and the fluid and is useful for scaling relaxation to pore size. However, surface relaxivity is not well known, and the industry standard practice is to relate petrophysical properties to T_2 distributions instead of pore-size distributions with the presumption that each T_2 value corresponds to individual pore sizes, even though the actual value is unknown (Lonnes et al., 2003). The T_2 cutoff is the interpreted boundary between free and immobile water (e.g., clay-bound water and bulk volume irreducible water). The industry standard cutoff value for shale of 3 ms is used in this study (Coates et al., 1999; Lonnes et al., 2003). Nonetheless, recent studies with fully saturated and centrifuged core plugs suggest that values can range between 0.54 and 4.28 ms (Li et al., 2017). Other research on the determination of the T_2 cutoff for irreducible water based on oven-dried samples indicate a value between 0.22 and 0.26 ms (Testamanti and Rezaee, 2017). Bode-Omoleye et al., 2017 has shown that, T_2 cutoff in carbonate mudrocks vary by carbonate facies and the 92 ms cutoff value for free and bound fluids for conventional carbonates leads to an overestimation of bound fluids in unconventional carbonates. Surface relaxivity values for shale have been suggested to be about 0.05 µm/s (Sulucarnain et al., 2012).

Gas transport in shale is a combination of diffusion in nanopores and Darcy flow in larger pores and fractures (Gensterblum et al., 2015; Javadpour, 2009; Javadpour et al., 2007; Sondergeld et al., 2010b). Gas in shale is sorbed to pore surfaces as adsorbed gas and stored in the open pore space as free gas. For a thorough analysis of gas in shale, the contribution of sorption should be considered. Low-pressure nitrogen sorption measurement is used to characterize pore volume, pore size distribution and other parameters such as surface area, microporosity, and pore shape; all of these factors control the adsorption capacity of shale (Rouquerol et al., 1994; Thommes et al., 2015). Pore shape influences pore volume, connectivity, and rock strength (Labani et al., 2013; Zhang et al., 2016). When the low-pressure nitrogen adsorption technique is used for pore size distribution analysis, the pores are distributed thus: pores < 2 nm in diameter are micropores, and those between 2 and 50 nm are mesopores. The pore size of 50 nm corresponds to a relative pressure of 0.96 and greater for nitrogen adsorption isotherm. However, adsorption experiments with relative pressures of 0.96 are considered difficult, and applicability of capillary condensation theory is not well understood (Kaneko, 1994).. Therefore, larger pores (diameter > 200 nm) cannot be measured with this technique (Kuila and Prasad, 2013; Rouquerol et al., 1994; Thommes et al., 2015). Crushed shale is typically used for low-pressure nitrogen sorption analysis to estimate surface area and pore size distribution (Mastalerz et al., 2017; Rezaee, 2015; Wang and Ju, 2015; Wei et al., 2016).

Mercury injection capillary pressure testing (MICP) is another technique used to determine pore size distribution. High pressures (up to 60,000 psi; 414 MPa) are applied to crushed samples, and Washburn's equation is used to estimate pore size distribution (Giesche, 2006). Because of the molecular size of mercury, the pores that can be identified with this method are in the range 3.5 nm to 500 µm (mesopores and macropores) (Clarkson et al., 2013; Giesche, 2006; Kuila and Prasad, 2013; Liu et al., 2017). A common limitation of MICP is the requirement of very high pressures (30,000 – 60, 000 psi) for injection, which may deform the rock sample under investigation and thus affect pore throat geometry and connectivity (Bustin et al., 2008).

Retort analysis to measure free, bound, and structural water saturation, and helium porosimetry for porosity analysis, and the Gas Research Institute (GRI) method for porosity and permeability analysis all make use of crushed rock samples (Luffel et al., 1993; Handwerger et al., 2011, 2012). Crushing decreases the path length for gas to access the entire pore structure, shortens fluid extraction time, and enables better access to pore space in shale. In addition, crushing increases sample surface area which can quicken rock petrophysical analysis but also may introduce analytical artifacts related to crushing-related fracturing of particles (Luffel et al., 1993; Spears et al., 2011).

Core plugs from shale can be used for a variety of purposes, such as measurement of permeability using the steady state technique and the pulse decay technique (Gensterblum et al., 2015; Lasswell, 2014; Sander et al., 2017; Tinni et al., 2012) Porosity and permeability also can be analyzed by NMR analysis, which is well suited for nanoporous materials like shale (RP40, 1998; Shafer, 2013). This study seeks to (1) compare NMR response and the derived pore size distributions in crushed and whole shale samples, (2) compare pore size distributions determined from NMR and low-pressure nitrogen sorption, and (3) analyze NMR response and pore geometry across a range of particle sizes.

2.0. Experimental materials and methods

2.1. Samples

The core that was used for this study was recovered from the Danker #1-28 well (API number 350812381700003). The Danker well was drilled in Lincoln County, Oklahoma, USA, and the core was donated to the Boone Pickens School of Geology by Sundown Energy. The core was taken from 4900 ft (1493.5 m) to 4914.5 ft (1497.9 m) and includes the Woodford Shale (Devonian), which is an important petroleum source rock and reservoir rock in the southern Midcontinent of the USA (Cardott, 2013; Passey et al., 2010). A description and graphic log of the core is available in Achang et al. (2017).

Samples were taken from the Danker #1-28 core at depths of 4907-4911 ft (1495.65–1496.87 m) and crushed to particle sizes of 2.00, 1.70, 1.40, 1.20, 1.00, 0.85, and 0.71 mm, which are commonly used in laboratory analysis. Two whole-rocks were cut from the same interval of 1496.26-1496.87 m into cubelike forms with dimensions of 10 x 8 x 5 mm. This size was determined by the size and efficiency of the Bruker minspec (mq 20) NMR probe, which can accommodate samples with a maximum volume of 10 ml. Low-pressure nitrogen adsorption measurements were performed with a Quantachrome 2200e apparatus, and porosity was measured with a Core Laboratories Shale Matrix Permeameter (SMP 200) and with He-pycnometery. Four shale samples of 7 ×10 × 2.5 mm were ion milled with the JEOL IB-19500CP cross section polisher and imaged with a FEI Quanta

600 Field Emission SEM. SEM images also were taken of crushed rock particles to identify fractures and other features that may indicate damage during sample preparation.

2.2. NMR measurements

A Bruker Minispec (mq20) NMR unit was used to measure T_2 transverse relaxation using Carr, Purcell, Meiboom, and Gill (CPMG) pulse sequences (Coates et al., 1999). The magnetic field strength of the instrument ranges from 0.17 T (1700 Gauss) to 1.41 T (14,000 Gauss) with a resonant frequency of 20 MHz. After the equipment was turned on, 2 hours was allowed for stabilization of the electronics and the magnets at a temperature of 40°C. A Julabo temperature bath was used to stabilize the temperature of the probe at 25°C. A standard sample (daily check sample) was run to verify the proper functioning of the equipment. Whole-rock and crushed samples were vacuum saturated with deionized water for 24 h at 23°C. The inter-echo spacing (TE) was estimated using the NMR instrument. For the whole samples, TE is 0.1 ms and for crushed samples, TE is 0.06 ms (the lower limit of TE for the NMR unit is 0.04 ms). The wait time used is 5 s and the number of scans was set at 10. Samples were run for < 3 min. The whole rocks were placed in the probe individually, and replicate T_2 relaxation readings were recorded for each sample. Also, 10 ml of crushed sample was placed in the probe, and the T_2 relaxation time was measured. After each measurement, the data is inverted to obtain T_2 distributions for the whole-rock and crushed samples (muti-exponential inverse Laplace transform based on Contin software was used to invert the data). Scanning Electron Microscopy (SEM) was used to analyze shale fabric and pore geometry.

Limitations of measurements

Fig IV - 1 illustrates replicate runs of the crushed shale and whole-rock samples. The crushed sample has a TE value of 0.06 ms and the whole-rock sample has a value of 0.1 ms. Repeat runs for the whole rock samples show significant differences (Fig IV - 1A), whereas those for crushed shale samples are effectively identical (Fig IV - 1B).

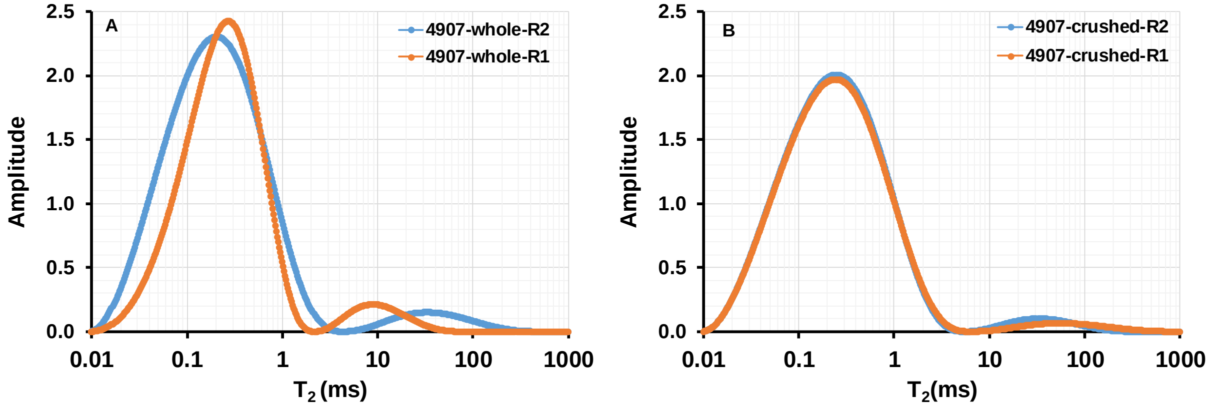

Fig IV - 1. Replicate runs of T_2 distribution (A) for whole and (B) crushed shale samples. R1 = run 1, R2 = run 2.

Studies on the effect of temperature on NMR surface relaxation indicate that T_2 distribution can shift as temperature increases (Godefroy et al., 2001, 2002). The slight differences in the T_2 profile of the whole-rock sample could be due to temperature changes, whereas the runtime for the crushed sample is shorter and thus minimally affected by temperature variation. Therefore, during measurements samples should not be left in the probe longer than is required to obtain quality results.

2.3. Low-pressure nitrogen adsorption measurements

Low-pressure nitrogen adsorption tests were performed using the Quantachrome Instruments Nova 2200e surface area and pore size analyzer. This instrument makes use of a static manometric technique, where changes in pressure of calibrated gas volumes at constant temperature (77°K) are measured. The absorbed volume (V_{ads}) and relative pressure (P/P_0) at STP are measured (P is the pressure of the sorbent; i.e., the sample; and P_0 is the saturation pressure in the system). The crushed samples (0.10 g) are degassed at 100°C to remove free water, gas and other hydrocarbons for 4 h. A known amount of pure gas is admitted to a confined, calibrated volume containing the adsorbent. The pressure in the confined volume falls as gas is adsorbed until equilibrium is established. The amount of gas adsorbed at the equilibrium pressure is the difference between the amounts of gas admitted into the confined calibrated volume containing the sample and the gas required to fill the pore space in the sample (Rouquerol et al., 1994; Thommes et al., 2015; Wei et al., 2016). The adsorption isotherms were generated automatically with the instrument's Novawin software, which employs a number of theoretical models for sorption analysis. The total pore volume was derived from the amount of vapor adsorbed at a relative pressure close to unity by assuming the pores are filled with liquid adsorbate. The average pore size is then estimated assuming cylindrical pores with equation (2)

$$r_p = 2\frac{V_{ads}}{S}, \tag{2}$$

where the average pore radius is r_p, the total volume of nitrogen adsorbed is V_{ads}, and S is the surface area (Labani et al., 2013; Rouquerol et al., 1994).

Pore size and pore size distribution were estimated using the Barrett, Joyner, and Halenda (BJH) methods by applying the Kelvin equation (3) (Barrett et al., 1951; Labani et al., 2013; Rouquerol et al., 1994; Thommes et al., 2015). Care has to be taken since Kelvin's equation is not applicable for pores with diameter < 1.7 nm (Kuila and Prasad, 2013).

$$ln\left(\frac{P}{P_0}\right) = \frac{2\gamma V_m}{RTr_k} cos\theta, \tag{3}$$

where P is the gas pressure, P_0 is the saturation pressure of the sorbent (sample), γ is the surface tension of nitrogen at 77°K, V_m is the molar volume of nitrogen, R is the molar gas constant, r_k is the Kelvin radius of the pore, T is the boiling point of nitrogen (77°K), and θ is the contact angle between the sample and mercury.

The total specific surface area was calculated using the Brunauer, Emmett, and Teller (BET) model (Brunauer et al., 1938), and the shapes of the sorption isotherm and the sorption-desorption hysteresis pattern were used to predict pore shape using the work of Thommes et al. (2015) as a guide.

3.0. Results

3.1. Shale samples

The Woodford Shale in the Danker #1-28 core is dominantly laminated and contains abundant thin pyrite laminae (Fig IV - 2A). The core also contains numerous pyrite lenses and microfossils, including *Tasmanites* algal cysts and conodonts. Rock-Eval pyrolysis indicates that the T_{max} value of the shale is 429°C, which is roughly equivalent to a vitrinite reflectance of 0.56%, which is typical in the area where the core was retrieved (Cardott, 2012). Total organic content (TOC) is 7.53% at 4907 ft (1495.7 m) and 11.2% at 4909 ft (1496.3 m).

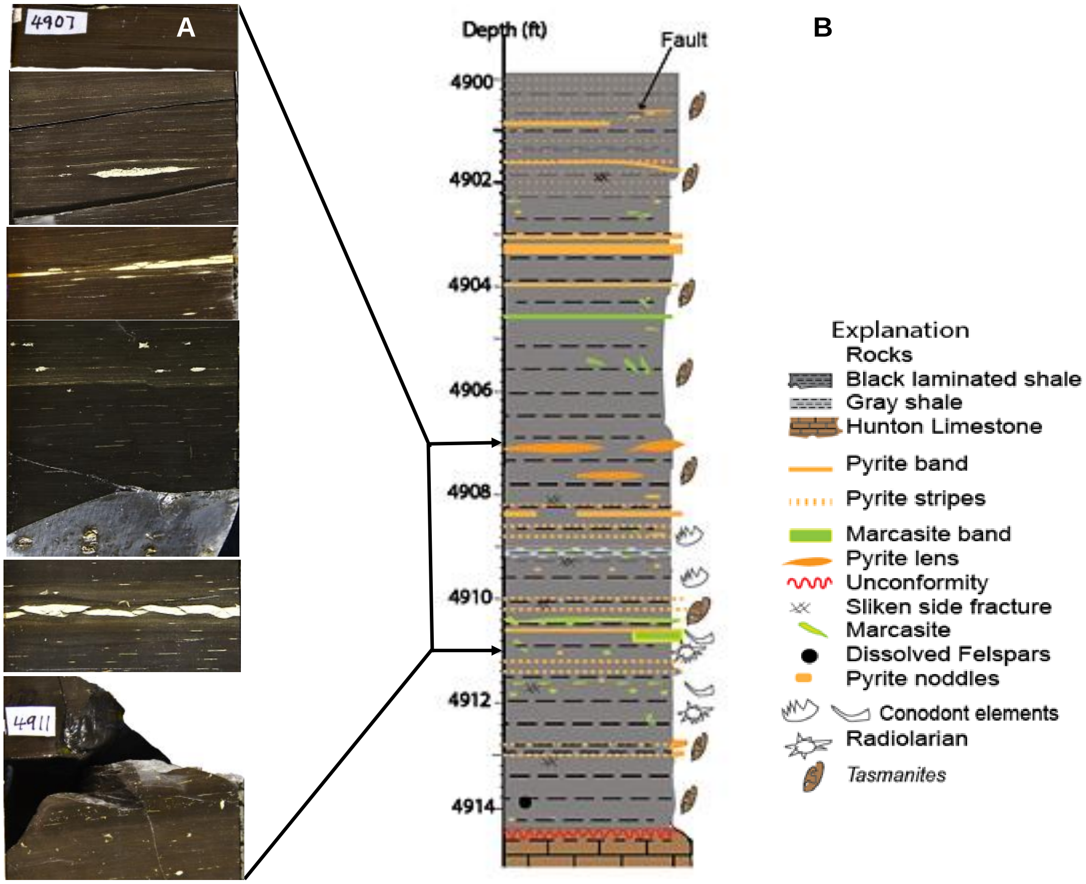

Fig IV - 2. Sample photograph and a graphic log of the Danker #1-28 core. (A) Photograph of slabbed core and (B) stratigraphic column of the Danker #1-28 core showing major rock types and sedimentary features.

3.2. T_2 distribution of whole-rock versus crushed samples

The raw data obtained from a spin-echo decay during an NMR measurement (Fig IV - 3A) was inverted to obtain a T_2 distribution (Fig IV - 3B) using a multiexponential Inverse Laplace Transform (ILP). In the case of the Minspec (mq 20), Contin software was used for inversion.

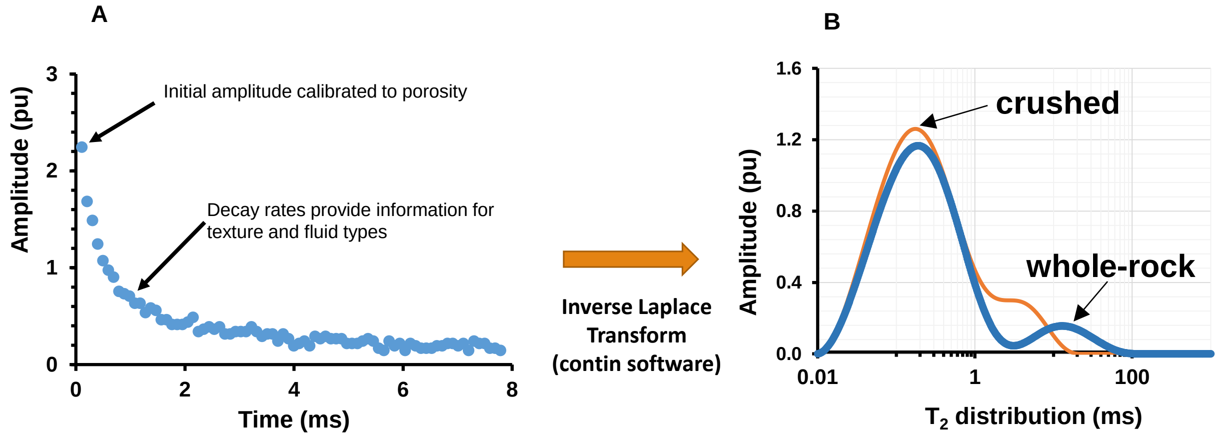

Fig IV - 3. (A) decay of the spin-echo train, which is a function of the amount and distribution of hydrogen present in pore fluid. The maximum amplitude is proportional to the porosity for fully saturated samples. (B) T_2 distribution of inverted spin-echo train use to estimate pore-size distribution.

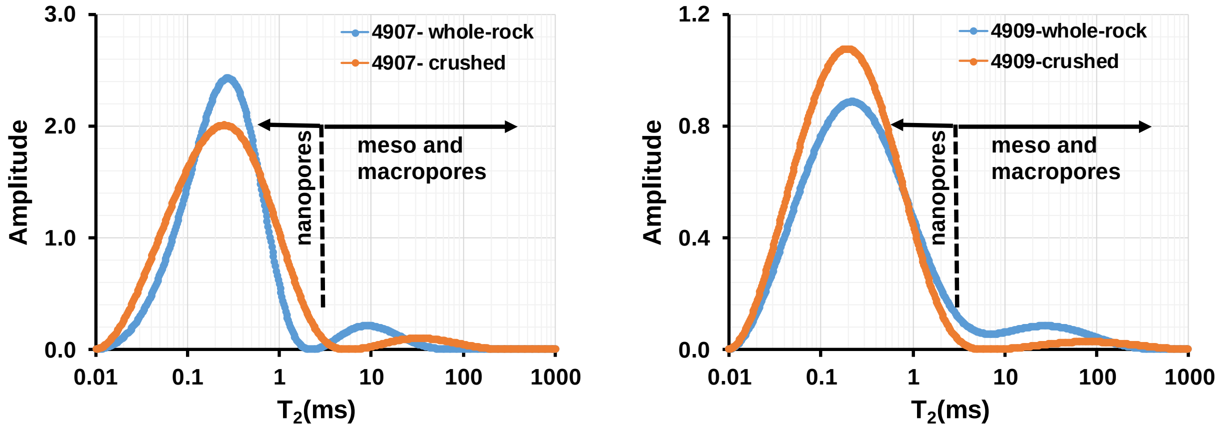

Fig IV - 4. T_2 distribution curves for whole and crushed shale samples from the Danker #1-28 core. (A) T_2 distribution curves for sample 4907. (B) T_2 distribution curves for sample 4909.

The dashed line on the T_2 distribution curves (Fig IV - 4) is the 3 ms marker for the T_2 cutoff. The part of the curve to the left of the 3 ms line is proportional to microporosity and nanoporosity (<2 nm) and to the right is proportional to mesoporosity and macroporosity (> 2 nm). The area under the T_2 distribution curves is proportional to total porosity. The T_2 distribution curves from the Danker core samples have a bimodal distribution. For $T_2 < 3$ ms the area under the distribution is largest and corresponds to nanoporosity and microporosity while the less dominate mode corresponds to mesoporosity and macroporosity. However, results can vary when comparing whole-rock and crushed samples. In sample 4907 (Fig IV - 4A), the area under the T_2 curves below the T_2 cutoff is similar for the crushed and whole-rock samples, but the amplitude of the whole-rock sample is greater than that of the crushed sample. At values above the cutoff, the whole rock sample has a higher amplitude, and the crushed sample is shifted toward larger T_2 values, indicating larger pores. In sample 4909 (Fig IV - 4B), by contrast, the area and amplitude below the T_2 cutoff is greater for the crushed sample than for the whole-rock sample. Above the T_2 cutoff, the curve for the whole-rock sample indicates a positive shift of mesoporosity and macroporosity. Specifically, the crushed sample reaches peak amplitude near 100 ms, which is near the upper limit of the T_2 values recorded for the whole-rock sample.

3.3. T_2 distribution of crushed samples with different particle sizes

Fig IV - 5 shows a series of T_2 distributions for a range of particle sizes ranging from 0.60 to 2.00 mm; the blue lines on the plots are for whole-rock samples, whereas the orange lines are for crushed rock samples with particle sizes ranging from 0.60 to 2.00 mm. The T_2 distribution for the whole-rock sample shows the bimodal pattern described above, with a major mode representing nanoporosity below 3 ms and a subordinate mode representing mesoporosity and macroporosity above 3 ms. The T_2 distributions for the crushed samples differ from the whole-rock sample. These differences are minimal in the main mode between T_2 values of 0.01and 3 ms at most size fractions, although the amplitude of this mode is suppressed at a particle size of 1.20 mm. All plots show differences between whole and crushed rock at T_2 values higher than 1 ms. These differences are relatively minor at particle sizes greater than 1.4 mm. At increasingly smaller particle sizes, a major mode in the crushed samples is apparent above 1 ms, and the amplitude of this mode increases at progressively smaller particle sizes. And at particles sizes smaller than 0.85 mm, the amplitude approaches or even exceeds that of the major mode associated with nanoporosity, indicating that significantly more mesopores and macropores exist in the smaller crushed particle size fractions relative to the whole-rock sample. In the next section, the porosity of each particle size is quantified.

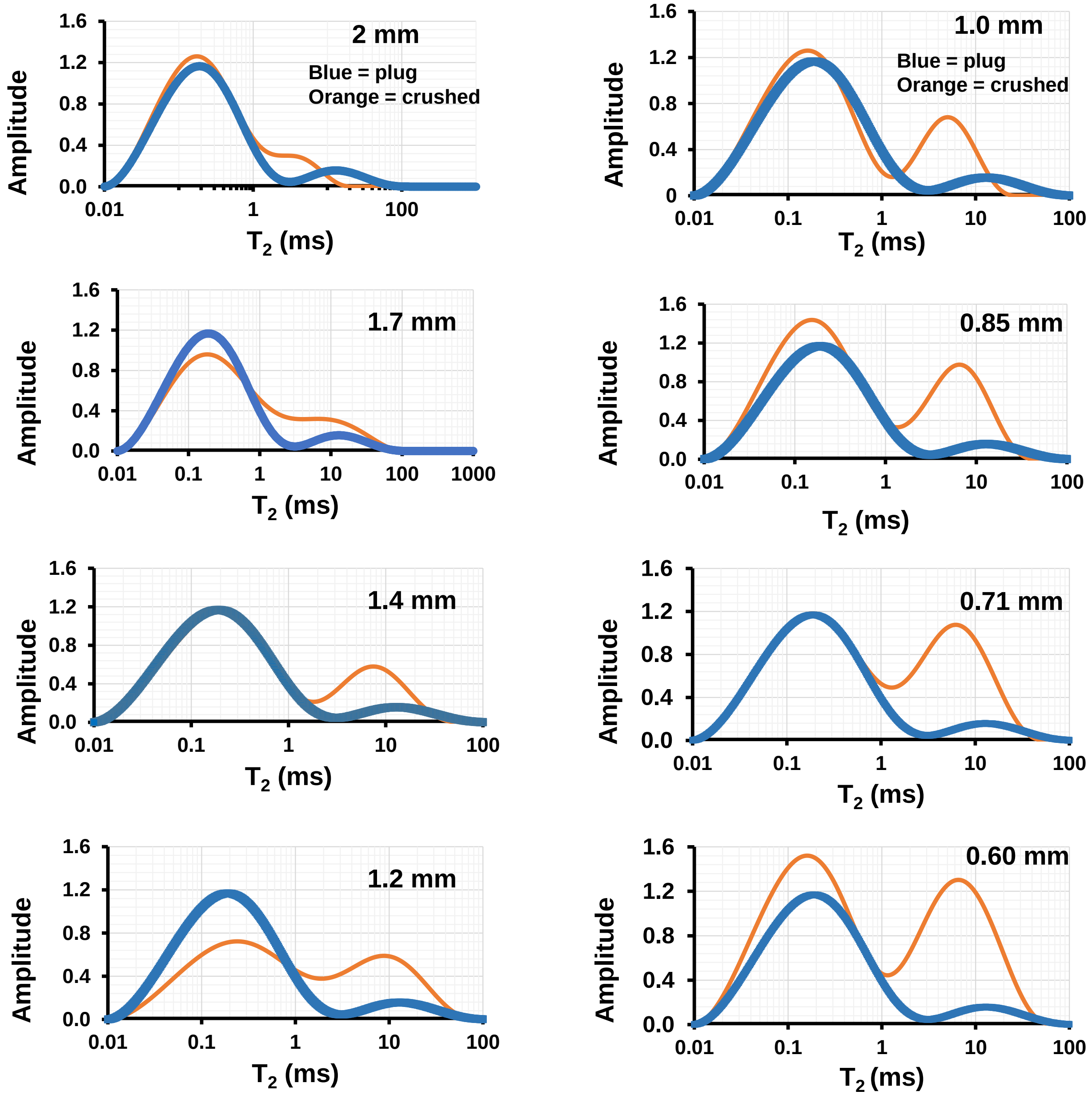

Fig IV - 5. Variation of T_2 distribution of whole-rock and crushed shale of various particle sizes (2.0 mm, 1.7 mm, 1.4 mm, 1.2 mm, 1.0 mm, 0.85 mm, 0.7 mm and 0.6 mm) from depths of 4909 ft (1496.26 m). Note that T_2 distributions for crushed rock resemble that for whole-rock at particle sizes greater than 1.2 mm and that a major mode at T_2 values >1 ms is increasingly pronounced at particle sizes smaller than 1.4 mm. The increase in the area under the T2 distribution corresponds to increasing porosity.

3.4. NMR and helium (He) porosity of crushed samples

The total porosity obtained from NMR spin-echo decay and helium porosity were plotted versus particle size (Fig IV - 6A). Porosity decreases with increasing particle size for both NMR and He porosity with He porosity about 2% greater than NMR porosity (Fig IV - 6A). The correlation coefficient for He porosity is -0.77 while that for NMR is -0.62, and so the correlation is weak, especially for NMR porosity. The range of He porosity with particle size is only 1%, and although there is a trend, the variable is nearly invariant. The plot of NMR porosity, by contrast, shows significant scatter, and values ranging from 0.2% to 3.4%. A plot comparing He porosity and NMR porosity (Fig IV - 6B), indicates a strong linear relationship between the variables, with a correlation coefficient of 0.93. The high He porosity compared to NMR porosity reflects the ability of He to access smaller pores than the water and liquid hydrocarbon in the sample.

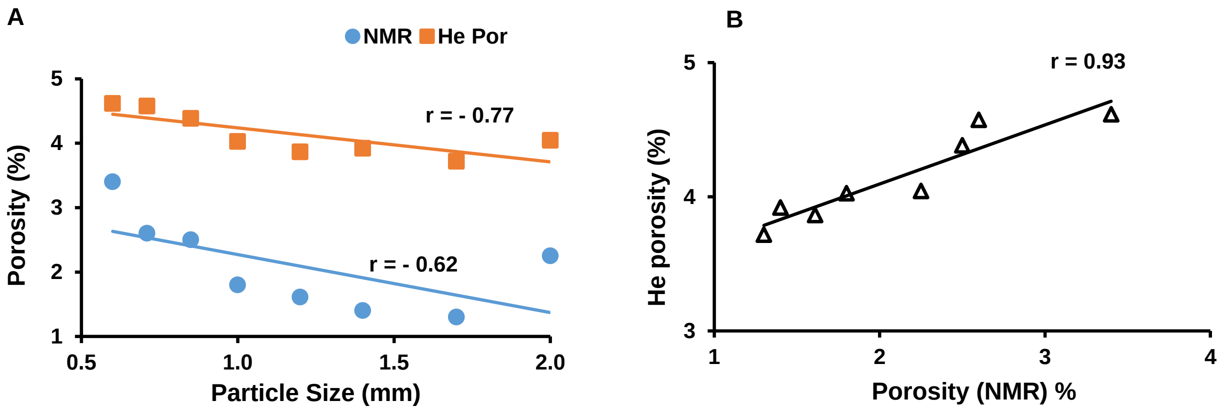

Fig IV - 6. Plots comparing porosity and particle size for sample 4909 ft (1496.26 m). (A) NMR and He porosity versus crushed particle size. Both He and NMR porosity decrease with an increase in particles size. (B) He vs. NMR porosity.

3.5. Nitrogen adsorption-desorption isotherms, pore size distribution and pore shape

As relative pressure (P/P_o) increases from 0.01 to 1.0, the adsorbed gas volume increases, thus defining the adsorption isotherm, and then as the relative pressure decreases, the gas volume decreases, thus defining the desorption isotherm (Fig IV - 7). There is no knee (a sharp bend in isotherm gradient) in all crushed shale particle sizes analyzed. The adsorption and desorption isotherms show significant hysteresis, with samples retaining more gas as the relative pressure decreases. The adsorption isotherms are of type III for all the samples, and the hysteresis pattern most closely resembles type B (Fig IV - 8) (Kuila and Prasad, 2013; Labani et al., 2013). Type B hysteresis corresponds with slit-shaped pores, but all the examples shown in Figure 8 incorporate a type III adsorption isotherm.

Pore size distribution was obtained from BJH inversion of nitrogen isotherms (Fig IV - 9). The dashed lines in Fig IV - 9 mark a pore size of 2 nm. The Quantachrome 2200e could not detect pore sizes below 3 nm, and so micropores were not captured. The detected pores are mesopores and macropores between 3 and 100 nm, and the shape of the curves indicate that mesopores dominate the samples. The curves define exponential decline from small to large pore sizes, and projection of the curves to 2 nm and below indicates that the samples may contain substantial microporosity.

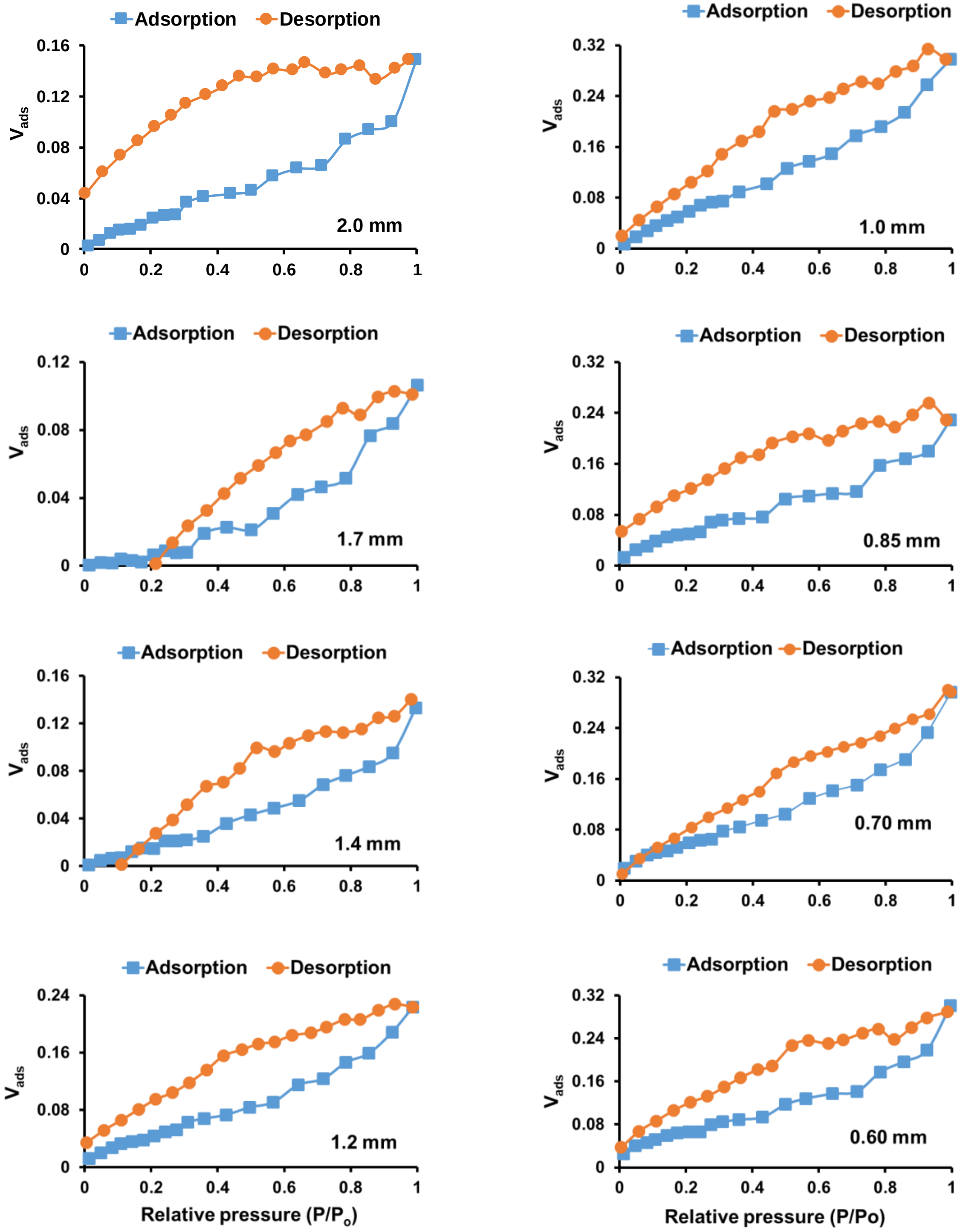

Fig IV - 7. Adsorption-desorption isotherms of crushed shale samples of different particle sizes. Isotherms derived at a temperature of 77°K. The space between the adsorption-desorption curve is use to describe the type of hysteresis (type b in this case) and as a proxy for pore shapes.

The BET specific surface area for the different crushed shale samples suggest surface area ranges from a minimum of 0.8 m^2/g to a maximum of 3.13 m^2/g and generally increase with decreasing particle size. The BET constant (C) values range from 0.99 to 21.81 and also tend to increase with decreasing particle size (Table8). The total pore volume shows a similar trend and ranges from 0.10 to 0.30 m^3.

Table8: Low pressure nitrogen result for different particle sizes

Particle size (mm)	BET surface area (m2/g)	BET constant (C)values	Total pore volume x10^{-2}
2	1.4	4.19	14.93
1.7	0.8	0.99	10.36
1.4	1.44	2.35	14.05
1.2	2.23	9.08	22.77
1	3.13	7.1	29.77
0.85	2.58	11.04	25.58
0.71	2.62	13.55	30.04
0.6	2.72	21.81	30.13

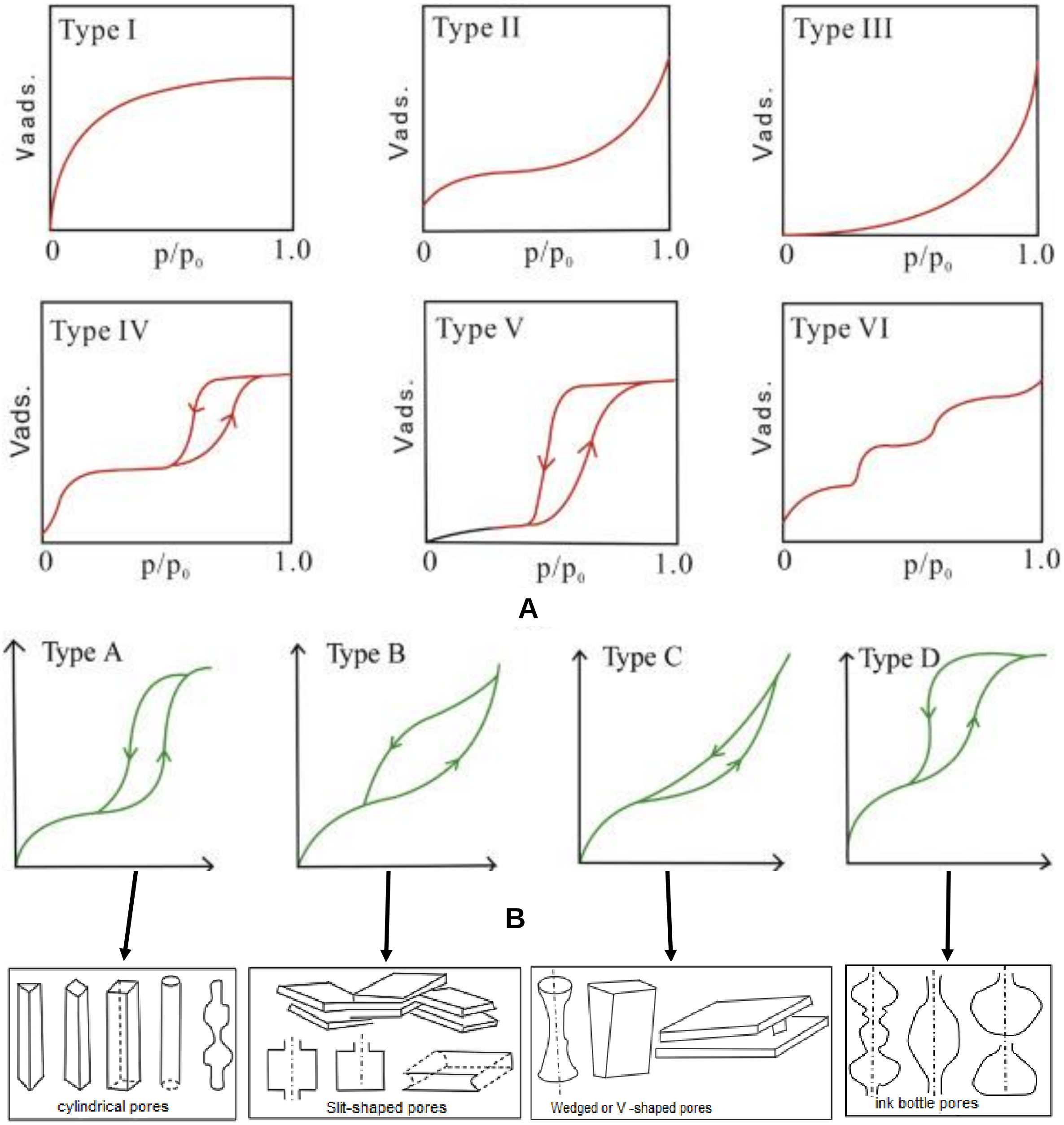

Fig IV - 8. Interpretation of pore size base on adsorption and desorption isotherms. (A) Adsorption isotherm types (B) hysteresis loops and their related pore shapes. V_{ads} is the adsorbed volume and P/P_0 is the relative pressure. Modified from (Chen et al., 2012; Thommes et al., 2015; Zhang et al., 2016). The Isothern for the Danker#1-28 samples is type II, hysteresis identified is type B corresponding to dominantly slit-shape pores. Type D is also plausible leading to less dominant ink bottle pores.

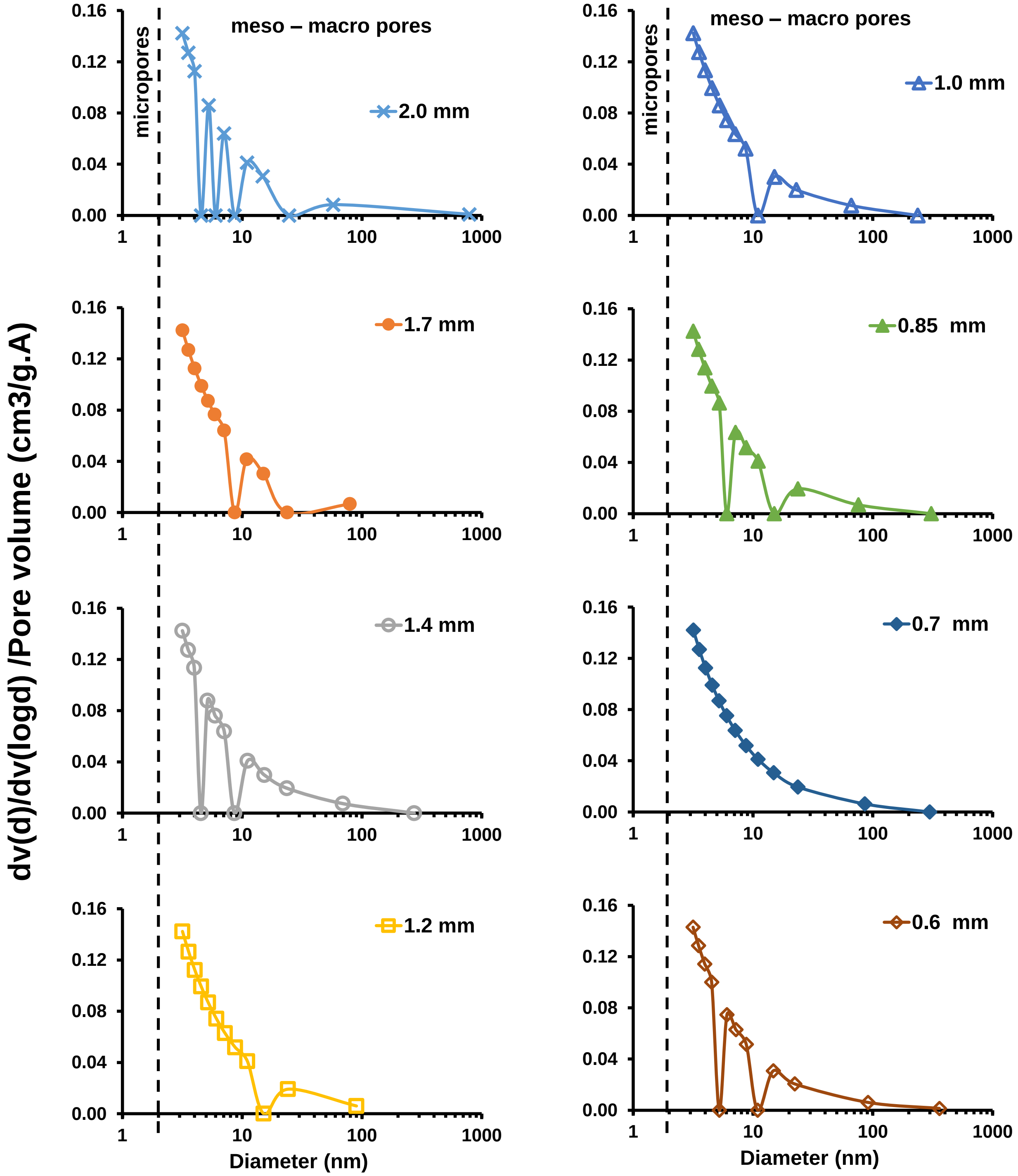

Fig IV - 9. Pore volume vs. pore diameter based on the BJH method. The dashed lines correspond to 2 nm and all the pore sizes are > 3 nm. Pores types >3 nm correspond to mesopores and macropores.

4.0. Discussion

4.1. T_2 distribution of crushed and whole-rock shale

In NMR results, T_2 relaxation values are directly proportional to pore size, and the area under the T_2 distribution is directly proportional to total porosity (Coates et al., 1999; Kenyon, 1997; Kleinberg et al., 1993; Lonnes et al., 2003). The increase in area under the T_2 distribution and broader pore size distribution of crushed shale compared to whole-rocks suggest crushing increases the porosity in the crushed samples, and that a large fraction of total porosity is added to samples with small particle sizes (Fig IV - 5). A possible reason for this observation is that crushing can add a substantial fraction of mesoporosity and macroporosity, thereby exposing more protons to the static magnetic field (Fig IV - 5). Since the pore size distribution for crushed samples and whole-rock track one another at T_2 values < 2.5 ms in most samples (Fig IV - 5), this segment could be used to predict the micropore sizes and porosity, while the segment beyond 2.5 ms is altered by crushing and therefore, does not represent the original condition of the rock. Our results agree with previous studies where NMR was used to track porosity changes as a result of variable fracture intensity in shale and coal (Veselinovic et al., 2016; Yao et al., 2010). The interpretations above could assist in understanding naturally fractured and hydrofractured shale reservoirs by providing insights on ways fracturing affects reservoir architecture (Veselinovic et al., 2016)..

The discontinuous bimodal distributions in Fig IV - 4 suggest there is a discontinuity in the pore size distribution, apparently between micropores and mesopores. Whole-rock samples 4907 and 4909 have TOC values of 7.5 and 11.2%, respectively.

The T_2 cutoff between bound and free water that is generally accepted in the industry and used in this study for shale is 3 ms (Coates et al., 1999; Testamanti and Rezaee, 2017). Comparing this value to T_2 distributions for crushed shale of different particle sizes (Fig IV - 5), we suggest a progressive increase in larger pores and porosity beyond 3 ms with a decrease in particle size related to rock damage during crushing. This means that crushing is creating artificial porosity, and this artificial porosity constitutes an increasing proportion of rock volume as particle size decreases. These results provide insight on how to assess the degree of damage caused to shale samples by the crushing process and can thus assist in choosing an appropriate particle size for pressure-decay permeability analysis.

NMR and He porosity have a correlation coefficient of 0.93. However, porosity values obtained by He porosimetry are much greater than those obtained from NMR and previous studies suggest ±1 to ±1.5 pu difference similar to observations reported in this study (Fig IV - 6) (Coates et al., 1999; Lonnes et al., 2003).

4.2. Pore size distribution (BJH) and surface area (BET) of shale

Pore size distribution determined using the BJH method further confirms the presence of mesopores and macropores in the shale samples (Fig IV - 9). However, pores smaller than 3 nm cannot be observed with low-pressure nitrogen sorption methods because of instrument limitation. Pore sizes equal to 50 nm have relative pressures of 0.96 and relative pressures between 0.96-1.0 correspond to pores greater than 200 nm and this region is not well understood and difficult for sorption characterization. Therefore, the pore-filling mechanism takes place in the multilayer adsorption where mesopores and macropores are filled because the hysteresis curves have no knees (Kuila and Prasad, 2013; Thommes et al., 2015). NMR pore size distribution embodies micropores through macropores, since T_2 values range from 0.5 to 100 ms. Thus, a combination of NMR and BET adsorption methods more fully describe pore size distribution in shale.

From visual inspection and comparison with adsorption and desorption isotherms, we interpreted that the crushed samples have type III isotherms (Kuila and Prasad, 2013; Labani et al., 2013; Thommes et al., 2015; Zhang et al., 2016). (Fig IV - 7 & 8). The BET C constants are all < 50, and studies of BET theory suggest that, for C < ~50, the isotherm has no knee and thus no transition from a monolayer to multilayer adsorption (Kuila and Prasad, 2013; Thommes et al., 2015). Also, the presence of hysteresis is an indication of the presence of mesopores and signifies that uptake of nitrogen is faster during adsorption than expulsion during desorption.

Based on the hysteresis curves, the Woodford Shale samples analyzed in this study are interpreted to contain predominantly slit-shape pores (Fig IV - 7, 8), and SEM images further justify the presence of slit-shape pores between clay flakes and circular pores in organic matter in our samples (Fig IV - 10). The pore shapes are suggested to result from the manner in which clay layering is established and amorphous kerogen evolves following deposition, burial, diagenesis, and catagenesis (Foscolos, 1984).

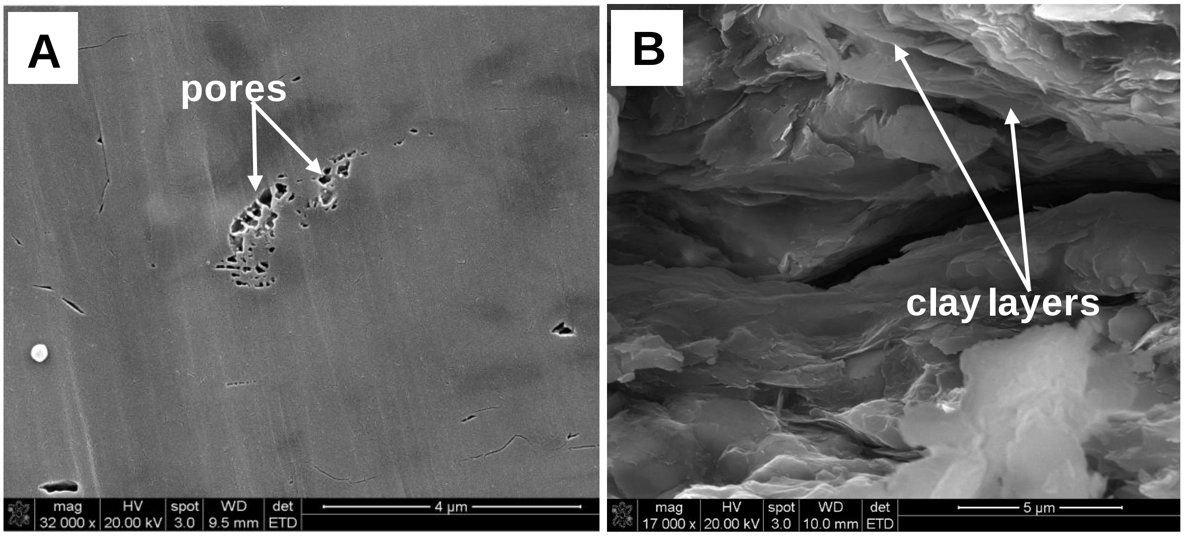

Fig IV - 10. SEM image sample from 4909-4911 ft (1496.29 – 1496.87 m). (A) circular pores in amorphous kerogen. (B) slit-shaped pores between clay particles.

5.0. Conclusions

The increase in area under the T_2 distribution and broader pore size distribution of crushed shale compared to whole-rocks is indicative of increasing porosity in the crushed samples and the increase is most significant for samples with smaller particle sizes. Bimodal pore size distributions are observed for both whole-rock and crushed samples. The progressive increase in larger pores and porosity beyond 3 ms (industry standard $T_{2cutoff}$) with a decrease in particle size is suggested to relate to rock damage during crushing. Thus, the degree of damage caused to crushed shale compared to whole-rock can assist in choosing an appropriate particle size for pressure-decay permeability analysis.

Pore size distribution from the BJH method indicates the presence of mesopores and smaller pores less than 3 nm cannot be observed with low-pressure nitrogen sorption methods because the Quantachrome 2200e isotherm inversion of PSD had no pores with sizes < 3 nm (instrument limitation). Pores greater than 200 nm cannot be analyzed as well because they exist in the relative pressure range of 0.96-1 which is not well understood and difficult for sorption characterization. The pore-filling mechanism is mainly multilayer adsorption where mesopores and macropores are filled and the desorption isotherm has no knees or sharp change in a gradient that can be identified. However, NMR pore size distribution embodies micropores through macropores, since T_2 values range from 0.5 to 100 ms.

Based on NMR and He-porosity measurements, porosity increases with decreasing particle size. Pore sizes obtained from nitrogen sorption are mostly in the mesopore range, and hysteresis results indicate that slit-shape pores predominate in the Woodford Shale in the Danker #1-28 core. Finally, a combination of methods and technologies is desirable to fully characterize the distribution of pore sizes in shale.

Acknowledgments

This paper is based on Doctoral research at Oklahoma State University (Achang). We thank Jim Puckette for providing access to the Danker #1-28 core, Michael Grammer and Ibukunoluwa Bode-Omoleye for Ion milling our samples, the American Association of Petroleum Geologists for support through the Grants-in-Aid Fund and Frank Blum and Ugo Arua of the Oklahoma State University Chemistry department for acquiring the sorption data.

References Cited

Barrett, E.P., Joyner, L.G., Halenda, P.P., 1951. The determination of pore volume and area distributions in porous substances. I. Computations from nitrogen isotherms. Journal of the American Chemical Society 73, 373-380.

Brownstein, K.R., Tarr, C., 1979. Importance of classical diffusion in NMR studies of water in biological cells. Physical Review A 19, 2446.

Brunauer, S., Emmett, P.H., Teller, E., 1938. Adsorption of gases in multimolecular layers. Journal of the American Chemical Society 60, 309-319.

Bustin, R., Bustin, A., Cui, X., Ross, D., Murthy Pathi, V., 2008. Impact of Shale Properties on Pore Structure and Storage Characteristics. Paper SPE 119892 presented at the SPE Shale Gas Production Conference, Fort Worth, Texas, USA, 16–18 November. dx. doi. org/10.2118/119892-MS.

Bode-Omoleye, I., Grammer, G.M., Zhang, C., 2017. Implications of Facies and Pore Architecture on NMR-Response in Carbonate Mudrock Reservoirs: Mississippian-Lime Play Case Study, AAPG Annual Convention and Exhibition

Cardott, B.J., 2012. Thermal maturity of Woodford Shale gas and oil plays, Oklahoma, USA. International Journal of Coal Geology 103, 109-119.

Cardott, B.J., 2013. Woodford Shale: from hydrocarbon source rock to reservoir, AAPG Woodford Shale Forum. American Association of Petroleum Geologists (AAPG) Tulsa, OK.

Chen, S.-B., Zhu, Y.-M., Wang, G.-Y., Liu, H.-L., Wei, W., Fang, J.-H., 2012. Structure characteristics and accumulation significance of nanopores in Longmaxi shale gas reservoir in the southern Sichuan Basin. Journal of China Coal Society 37, 438-444.

Chenevert, M., Amanullah, M., 1997. Shale preservation and testing techniques for borehole-stability studies. SPE Drilling & Completion 16, 146-149.

Clarkson, C.R., Jensen, J.L., Blasingame, T., 2011. Reservoir engineering for unconventional reservoirs: what do we have to consider? SPE 145080., North American Unconventional Gas Conference and Exhibition. Society of Petroleum Engineers.

Clarkson, C.R., Solano, N., Bustin, R., Bustin, A., Chalmers, G., He, L., Melnichenko, Y.B., Radliński, A., Blach, T.P., 2013. Pore structure characterization of North American shale gas reservoirs using USANS/SANS, gas adsorption, and mercury intrusion. Fuel 103, 606-616.

Coates, G.R., Xiao, L., Prammer, M.G., 1999. NMR logging: principles and applications. Haliburton Energy Services Houston.

Cui, X., Bustin, A., Bustin, R.M., 2009. Measurements of gas permeability and diffusivity of tight reservoir rocks: different approaches and their applications. Geofluids 9, 208-223.

Foscolos, A., 1984. Diagenesis 7. Catagenesis of argillaceous sedimentary rocks. Geoscience Canada 11.

Gensterblum, Y., Ghanizadeh, A., Cuss, R.J., Amann-Hildenbrand, A., Krooss, B.M., Clarkson, C.R., Harrington, J.F., Zoback, M.D., 2015. Gas transport and storage capacity in shale gas reservoirs–A review. Part A: Transport processes. Journal of Unconventional Oil and Gas Resources 12, 87-122.

Giesche, H., 2006. Mercury porosimetry: a general (practical) overview. Particle & particle systems characterization 23, 9-19.

Godefroy, S., Fleury, M., Deflandre, F., Korb, J.-P., 2001. Temperature effect on NMR surface relaxation, SPE Annual Technical Conference and Exhibition. Society of Petroleum Engineers.

Godefroy, S., Fleury, M., Deflandre, F., Korb, J.-P., 2002. Temperature effect on NMR surface relaxation in rocks for well logging applications. The Journal of Physical Chemistry B 106, 11183-11190.

Handwerger, D.A., Keller, J., Vaughn, K., 2011. Improved petrophysical core measurements on tight shale reservoirs using retort and crushed samples, SPE Annual Technical Conference and Exhibition. Society of Petroleum Engineers.

Handwerger, D.A., Willberg, D.M., Pagels, M., Rowland, B., Keller, J., 2012. Reconciling retort versus dean stark measurements on tight shales, SPE Annual Technical Conference and Exhibition. Society of Petroleum Engineers.

Javadpour, F., 2009. Nanopores and apparent permeability of gas flow in mudrocks (shales and siltstone). Journal of Canadian Petroleum Technology 48, 16-21.

Javadpour, F., Fisher, D., Unsworth, M., 2007. Nanoscale gas flow in shale gas sediments. Journal of Canadian Petroleum Technology 46.

Kaneko, K., 1994. Determination of pore size and pore size distribution: 1. Adsorbents and catalysts. Journal of membrane science 96, 59-89.

Kenyon, W., 1997. Petrophysical principles of applications of NMR logging. The Log Analyst 38.

Kleinberg, R., Straley, C., Kenyon, W., Akkurt, R., Farooqui, S., 1993. Nuclear magnetic resonance of rocks: T1 vs. T2, SPE annual technical conference and exhibition. Society of Petroleum Engineers.

Kuila, U., Prasad, M., 2013. Specific surface area and pore-size distribution in clays and shales. Geophysical Prospecting 61, 341-362.

Labani, M.M., Rezaee, R., Saeedi, A., Al Hinai, A., 2013. Evaluation of pore size spectrum of gas shale reservoirs using low pressure nitrogen adsorption, gas expansion and mercury porosimetry: A case study from the Perth and Canning Basins, Western Australia. Journal of Petroleum Science and Engineering 112, 7-16.

Lasswell, P., 2014. Steady-state permeability analysis in unconventional plays. AAPG Datapages/Search and Discovery 80404.

Li, A., Ding, W., Wang, R., He, J., Wang, X., Sun, Y., Gu, Y., Jiao, N., 2017. Petrophysical characterization of shale reservoir based on nuclear magnetic resonance (NMR) experiment: A case study of Lower Cambrian Qiongzhusi Formation in eastern Yunnan Province, South China. Journal of Natural Gas Science and Engineering 37, 29-38.

Liu, K., Ostadhassan, M., Zhou, J., Gentzis, T., Rezaee, R., 2017. Nanoscale pore structure characterization of the Bakken shale in the USA. Fuel 209, 567-578.

Lonnes, S., Guzman-Garcia, A., Holland, R., 2003. NMR petrophysical predictions on cores, SPWLA 44th Annual Logging Symposium. Society of Petrophysicists and Well-Log Analysts.

Loucks, R.G., Reed, R.M., Ruppel, S.C., Hammes, U., 2012. Spectrum of pore types and networks in mudrocks and a descriptive classification for matrix-related mudrock pores. AAPG bulletin 96, 1071-1098.

Loucks, R.G., Ruppel, S.C., 2007. Mississippian Barnett Shale: Lithofacies and depositional setting of a deep-water shale-gas succession in the Fort Worth Basin, Texas. AAPG bulletin 91, 579-601.

Luffel, D., Hopkins, C., Schettler Jr, P., 1993. Matrix permeability measurement of gas productive shales, SPE Annual Technical Conference and Exhibition. Society of Petroleum Engineers.

Mastalerz, M., Hampton, L., Drobniak, A., Loope, H., 2017. Significance of analytical particle size in low-pressure N 2 and CO 2 adsorption of coal and shale. International Journal of Coal Geology 178, 122-131.

Passey, Q.R., Bohacs, K., Esch, W.L., Klimentidis, R., Sinha, S., 2010. From oil-prone source rock to gas-producing shale reservoir-geologic and petrophysical characterization of unconventional shale gas reservoirs, International oil and gas conference and exhibition in China. Society of Petroleum Engineers.

Rezaee, R., 2015. Fundamentals of gas shale reservoirs. John Wiley & Sons.

Rouquerol, J., Avnir, D., Fairbridge, C., Everett, D., Haynes, J., Pernicone, N., Ramsay, J., Sing, K., Unger, K., 1994. Recommendations for the characterization of porous solids (Technical Report). Pure and Applied Chemistry 66, 1739-1758.

RP40, A., 1998. Recommended practices for core analysis. Feb.

Saidian, M., Prasad, M., 2015. Effect of mineralogy on nuclear magnetic resonance surface relaxivity: A case study of Middle Bakken and Three Forks formations. Fuel 161, 197-206.

Sander, R., Pan, Z., Connell, L.D., 2017. Laboratory measurement of low permeability unconventional gas reservoir rocks: A review of experimental methods. Journal of Natural Gas Science and Engineering 37, 248-279.

Schmoker, J., Oscarson, S.A., 1995. Descriptions of continuous-type (unconventional) plays of the US Geological Survey 1995 National assessment of United States oil and gas resources. US Geological Survey.

Shafer, J., 2013. Recent advances in core analysis. Petrophysics 54, 554-579.

Sondergeld, C., Newsham, K., Comisky, J., Rice, M., Rai, C., 2010a. Petrophysical Considerations in Evaluating and Producing Shale Gas Resources. Paper SPE 131768 presented at the SPE Unconventional Gas Conference, Pittsburgh, Pennsylvania, USA, 23–25 February.

Sondergeld, C.H., Newsham, K.E., Comisky, J.T., Rice, M.C., Rai, C.S., 2010b. Petrophysical considerations in evaluating and producing shale gas resources, SPE Unconventional Gas Conference. Society of Petroleum Engineers.

Spears, R.W., Dudus, D., Foulds, A., Passey, Q., Esch, W.L., Sinha, S., 2011. Shale gas core analysis: Strategies for normalizing between laboratories and a clear need for standard materials, SPWLA 52nd Annual Logging Symposium. Society of Petrophysicists and Well-Log Analysts.

Standards, A.I., International, A., 2007. Standard test method for equilibrium moisture of Coal at 96 and 97 percent relative humidity and 30 degress celcius, D1412 − 07.

Suarez-Rivera, R., Chertov, M., Willberg, D.M., Green, S.J., Keller, J., 2012. Understanding permeability measurements in tight shales promotes enhanced determination of reservoir quality, SPE Canadian Unconventional Resources Conference. Society of Petroleum Engineers.

Sulucarnain, I.D., Sondergeld, C.H., Rai, C.S., 2012. An NMR study of shale wettability and effective surface relaxivity, SPE Canadian Unconventional Resources Conference. Society of Petroleum Engineers.

Testamanti, M.N., Rezaee, R., 2017. Determination of NMR T 2 cut-off for clay bound water in shales: A case study of Carynginia Formation, Perth Basin, Western Australia. Journal of Petroleum Science and Engineering 149, 497-503.

Thommes, M., Kaneko, K., Neimark, A.V., Olivier, J.P., Rodriguez-Reinoso, F., Rouquerol, J., Sing, K.S., 2015. Physisorption of gases, with special reference to the evaluation of surface area and pore size distribution (IUPAC Technical Report). Pure and Applied Chemistry 87, 1051-1069.

Tinni, A., Fathi, E., Agarwal, R., Sondergeld, C.H., Akkutlu, I.Y., Rai, C.S., 2012. Shale permeability measurements on plugs and crushed samples, SPE Canadian Unconventional Resources Conference. Society of Petroleum Engineers.

Veselinovic, D., Green, D., Dick, M., 2016. Determination of Natural Fracture Porosity Using NMR, Unconventional Resources Technology Conference, San Antonio, Texas, 1-3 August 2016. Society of Exploration Geophysicists, American Association of Petroleum Geologists, Society of Petroleum Engineers, pp. 1062-1069.

Wang, G., Ju, Y., 2015. Organic shale micropore and mesopore structure characterization by ultra-low pressure N 2 physisorption: Experimental procedure and interpretation model. Journal of Natural Gas Science and Engineering 27, 452-465.

Wei, M., Xiong, Y., Zhang, L., Li, J., Peng, P.a., 2016. The effect of sample particle size on the determination of pore structure parameters in shales. International Journal of Coal Geology 163, 177-185.

Yao, Y., Liu, D., Cai, Y., Li, J., 2010. Advanced characterization of pores and fractures in coals by nuclear magnetic resonance and X-ray computed tomography. Science China Earth Sciences 53, 854-862.

Zhang, Q., Liu, R., Pang, Z., Lin, W., Bai, W., Wang, H., 2016. Characterization of microscopic pore structures in Lower Silurian black shale (S 1 l), southeastern Chongqing, China. Marine and Petroleum Geology 71, 250-259.

CHAPTER V

GENERAL CONCLUSION AND RECOMMENDATIONS FOR FUTURE WORK

General Conclusion

The objectives of this dissertation were to: (1) determine the relationship between crushed shale particle size and matrix permeability by analyzing pressure-decay curves using late time analysis (2) perform controlled experiments to evaluate the relationship between moisture content and permeability and (3) compare pore size distributions of whole-rock and crushed samples using NMR and gas porosimetry. Upon investigating these objectives, the following conclusions were reached:

When comparing permeability from different analytical datasets, care should be taken as different techniques for data interpretation yield different permeability values. Permeability from the hyperbolic pressure decay segment is highest, while that from the exponential segment is intermediate, and values determined from the whole curve yield the lowest values. Permeability determined from the hyperbolic segment is influenced by microfractures, larger pores and crushing-related particle damage and is thus not fully representative of the matrix permeability. To obtain permeability that is most representative of matrix permeability the exponential segment should be used for analysis. Measurement duration (≥ 500 s), the mass of sample in the sample holder, pressure variability from different laboratories, particle size, and the presence of microfractures all influence permeability. All particle sizes of the crushed shale investigated had microfractures with average aperture ranging from 60 to 1020 nm but showed no correlation between particle size and fracture width. The mass of the sample in the sample holder and Kc significantly influence the slope of LnFR vs time and thus affect the permeability determination. From moisture content and moisture equilibration relation with permeability, we conclude that moisture content is inversely proportional to permeability in shale, and moisture equilibrated shale samples result in more accurate and repeatable permeability numbers. Permeability increases with particle size for as-received and moisture equilibrated samples. However, moisture equilibrated samples have better correlation coefficients compared to as-received samples suggesting that moisture equilibration improves pressure decay permeability measurements in crushed shale samples. Though moisture equilibration does not restore the shale sample to its original moisture content, particularly in samples where hydrocarbons have devolatized, it does help normalize analysis by compensating for moisture loss during core retrieval, transport, and storage.

Research on comparing the pore size distribution of whole-rock and crushed shale samples using Nuclear Magnetic Resonance (NMR), gas porosimetry and low-pressure nitrogen sorption led to the following inferences: the area under the T_2 distribution increases with a decrease in particle size for crushed shale and stays same for the whole-rock. Porosity increase is most significant for samples with smaller particle sizes. The progressive increase in larger pores and porosity beyond 3 ms (industry standard $T_{2cutoff}$) with a decrease in particle size is suggested to relate to rock damage during crushing. The degree of damage caused to crushed shale compared to whole-rock can assist in choosing an appropriate particle size for pressure-decay permeability analysis. Bimodal pore size distributions exist for both whole-rock and crushed samples.

Pore size distribution from the BJH method indicates the presence of mesopore (3 nm to 50 nm) and smaller pores less than 3 nm cannot be observed because of instrument limitation. Pores greater than 200 nm cannot be analyzed as well because they exist in the relative pressure range of 0.96-1 which is not well understood and difficult for sorption characterization. The pore-filling mechanism is mainly multilayer adsorption where mesopores and macropores are filled and the desorption isotherm has no knees or sharp change in a gradient that can be identified. Based on nitrogen sorption we obtained Type II isotherms, with type B hysteresis which corresponds to slit-shaped pores in the Woodford Shale from the Danker #1-28 core. SEM imaging supports the presence of slit-shaped pores. NMR pore size distribution embodies micropores through macropores since T_2 values range from 0.5 to 100 ms (full spectrum of pores). From NMR and He-porosity measurements, porosity increases with decreasing particle size. Finally, a combination of methods and technologies is desirable to fully characterize the distribution of pore sizes in shale.

Future Research

- Perform tests on progressively larger particle sizes to identify optimal size; probably varies from sample to sample.
- Develop analytical standards for the determination of permeability by the pressure decay methods.
- Model the permeability of crushed shale using numerical methods, incorporate microfractures in the models and compare permeability results to those obtained from pressure decay curve analysis.
- Apply moisture equilibration methods to organic-poor, sealing shale units, those containing swellable clay and different li.
- Develop methods to assess shale permeability for CO2 sequestration

VITA

Mercy Achang

Candidate for the Degree of

Doctor of Philosophy

Dissertation: THE INFLUENCE OF PARTICLE SIZE, MICROFRACTURES, MOISTURE CONTENT ON THE PERMEABILITY OF CRUSHED SHALE SAMPLES

Major Field: **Geology**
Biographical

Education:
Completed the requirements for the Doctor of Philosophy in Geology at Oklahoma State University, Stillwater, Oklahoma in July, 2018.

Completed the requirements for the Master of Science in Geophysics at The University of Yaoundé I/Yaoundé, Cameroon in 2008.

Completed the requirements for the Master of Science in Secondary and High School Physics Teaching Grade II from Higher Teachers Training College Yaoundé, Yaoundé, Cameroon in 2006

Completed the requirements for the Bachelor of Science in Physics at The University of Dschang, Dschang, Cameroon in 2002

Completed the requirements for the Bachelor of Science in Secondary School Physics Teaching Grade I
The Advanced Teachers Training College, Annex Bambili, Cameroon in 1998

Experience:
Teaching and research Assistant at Oklahoma State University. August 2011 2018
Physics Teacher and head of department at Government Bilingual Practicing High School Yaoundé, Cameroon, 2006 - 2012
Physics Teacher at Government Bilingual High School Mbatu, Bamenda, Cameroon 2000-2003

Professional Memberships:
American Association of Petroleum Geologists (AAPG)
Society of Petrophysicists and Well Log Analysts (SPWLA)
National Association of Black Geoscientists (NABG)
Geological Society of America (GSA)
Society of Exploration Geophysicists (SEG)